THE EFFECTS OF MORPHOLOGICAL CHANGES AND CARBON NANOSPHERES ON THE PSEUDOCAPACITIVE PROPERTIES OF MOLYBDENUM DISULPHIDE

Tobile Khawula

A dissertation submitted to the Faculty of Engineering and the Built Environment, University of the Witwatersrand, in fulfilment of the requirements for the degree of Master of Science in Engineering.

Supervisors: Prof I. Sigalas and Prof K.I. Ozoemena

Co-Supervisor: Dr. P. Franklyn

Johannesburg,

21 July 2016

DECLARATION

I declare that the dissertation is my own unaided work. It is being submitted to the Degree of Master of Science to the University of the Witwatersrand, Johannesburg. It has not been submitted before for any examination to any other University.

……………………………………………………………………………………

(Signature of candidate)

……………………..day of………………….year…………………

ABSTRACT

The use of supercapacitors for energy storage is an attractive approach considering their ability to deliver high levels of electrical power, unlimited charge/discharge cycles, green environmental protection and long operating lifetimes. Despite the satisfactory power density, supercapacitors are yet to match the energy densities of batteries and fuel cells, reducing the competitiveness as a revolutionary energy storage device. Therefore, the biggest challenge for supercapacitors is the trade-off between energy density and power density. This presents an opportunity to enhance the electrochemical capacitance and mechanical stability of an electrode. Previous attempts to get around the problem include developing porous nanostructured electrodes with extremely large effective areas.

One of the emerging high-power supercapacitor electrode materials is molybdenum disulfide (MoS_2), a member of the transition-metal dichalcogenides (TMDs). Its higher intrinsic fast ionic conductivity and higher theoretical capacity have attracted a lot of attention, particularly in supercapacitors. In addition to double-layer capacitance, diffusion of the ions into the MoS_2 at slow scan rates gives rise to Faradaic capacitance. Analogous to Ru in RuO_2, the Mo center atom displays a range of oxidation states from +2 to +6. This plays an important role in enhancing charge storage capabilities. However, the electronic conductivity of MoS_2 is still lower compared to graphite, and the specific capacitance of MoS_2 is still very limited when used alone for energy storage applications. As evident in several literature reports, there is a need to improve the capacitance of MoS_2 with

conductive materials such as carbon nanotubes (CNT), polyaniline (PANI), polypyrrole (PPy), and reduced graphene (r-GO). Carbon nanospheres (CNS) have, in the past, improved the conductivity of cathode material in Li-ion batteries, owing to their appealing electrical properties, chemical stability and high surface area.

The main objective of this dissertation research is to develop nanocomposite materials based on molybdenum sulphide with carbon nanospheres for pseudocapacitors with simultaneously high power density and energy density at low production cost. The research was carried out in two phases, namely, (i) Symmetric pseudocapacitors based on molybdenum disulfide (MoS_2)-modified carbon nanospheres: Correlating physico-chemistry and synergistic interaction on energy storage and (ii) The effects of morphology re-arrangements on the pseudocapacitive properties of mesoporous molybdenum disulfide (MoS_2) nanoflakes. The physico-chemical properties of the MoS_2 layered materials have been interrogated using the surface area analysis (BET), scanning electron microscopy (SEM), transmission electron microscopy (TEM), x-ray diffraction (XRD), Raman, fourier-transform infrared (FTIR) spectroscopy, and advanced electrochemistry including cyclic voltammetry (CV), galvanostatic cycling with potential limitation (GCPL), repetitive electrochemical cycling tests, and electrochemical impedance spectroscopy (EIS).

In the first phase, Molybdenum disulfide-modified carbon nanospheres (MoS_2/CNS) with two different morphologies (spherical and flower-like) have

been synthesized using hydrothermal techniques and investigated as symmetric pseudocapacitors in aqueous electrolyte. The two different MoS_2/CNS layered materials exhibit unique differences in morphology, surface areas, and structural parameters, which have been correlated with their electrochemical capacitive properties. The flower-like morphology (f-MoS_2/CNS) shows lattice expansion (XRD), large surface area (BET analysis), and small-sized nanostructures (corroborated by the larger FWHM of the Raman and XRD data). As a contrast to the f-MoS_2/CNS, the spherical morphology (s-MoS_2/CNS) shows lattice contraction, small surface area with relatively large-sized nanostructures. The presence of CNS on the MoS_2 structure leads to slight softening of the characteristic Raman bands (E^1_{2g} and A_{1g} modes) with larger FWHM. The MoS_2 and its CNS-based composites have been tested in symmetric electrochemical capacitors in aqueous 1 M Na_2SO_4 solution. CNS improves the conductivity of the MoS_2 and synergistically enhanced the electrochemical capacitive properties of the materials, especially the f-MoS_2/CNS-based symmetric cells (most notably, in terms of capacitance retention). The maximum specific capacitance for f-MoS_2/CNS-based pseudocapacitor show a maximum capacitance of 231 F g^{-1} with high energy density 26 Wh kg^{-1} and power density 6443 W kg^{-1}. For the s-MoS_2/CNS-based pseudocapcitor, the equivalent values are 108 F g^{-1}, 7.4 Wh kg^{-1} and 3700 W kg^{-1}. The high-performance of the f-MoS_2/CNS is consistent with its physico-chemical properties as determined by the spectroscopic and microscopic data.

In the second phase, Mesoporous molybdenum disulfide (MoS_2) with different morphologies has been prepared via a hydrothermal method using

different solvents, water or water/acetone mixtures. The MoS_2 obtained with water alone gave graphene-like nanoflakes (g-MoS_2) while the other with water/acetone (1:1 ratio) gave a hollow-like morphology (h-MoS_2). Both materials are modified with carbon nanospheres as conductive materials and investigated as symmetric pseudocapacitors in aqueous electrolyte (1 M Na_2SO_4 solution). Interestingly, a simple change of synthesis solvents confers on the MoS_2 materials different morphologies, surface areas, and structural parameters, correlated by electrochemical capacitive properties. The g-MoS_2 exhibits higher surface area, higher capacitance parameters (specific capacitance of 183 F g^{-1}, maximum energy density of 9.2 Wh kg^{-1} and power density of 2.9 kW kg^{-1}) but less stable electrochemical cycling compared to the h-MoS_2. These findings have opened doors for further exploration of the synergistic effects between MoS_2 graphene-like sheets and CNS for energy storage.

DEDICATION

To God, thank you for your love and guidance. If it wasn't for you my God, I wouldn't be where I am today.

AKNOWLEDGEMENTS

TABLE OF CONTENT

LIST OF FIGURES

LIST OF TABLES

LIST OF ABBREVIATIONS

MoS_2	Molybdenum disulphide
s-MoS_2	Spherical-Molybdenum disulphide
f-MoS_2	Flower-like-Molybdenum disulphide
g-MoS_2	Graphene-like-Molybdenum disulphide
h-MoS_2	Hollow-Molybdenum disulphide
CNS	Carbon nanospheres
s-MoS_2/CNS	Spherical-Molybdenum disulphide/carbon nanospheres
f-MoS_2/CNS	Flower-like-Molybdenum disulphide/carbon nanospheres
g-MoS_2/CNS	Graphene-like-Molybdenum disulphide/carbon nanospheres
h-MoS_2/CNS	Hollow-Molybdenum disulphide/carbon nanospheres
CNT	Carbon nanotubes
MWCNT	Multi-wall carbon nanotubes
r-GO	Reduced graphene
PANI	Polyaniline
Ppy	Polypyrrole
PEG	Polyethelyene glycol
PVDF	Polyvinylidene fluoride
SEM	Scanning electron microscopy
EDS	Energy dispersive X-ray spectroscopy
TEM	Transmission electron microscopy

BET	Brannauer-Emmett-Teller
XRD	X-ray diffraction
FTIR	Fourier transform infrared spectroscopy
CV	Cyclic voltammetry
GCD	Galvanostic charge-discharge
EIS	Electrical impedance spectroscopy
ESR	Equivalent series resistance
EEC	Electrical equivalent circuit
FWHM	Full-width at half maximum
CPE or Q	Constant-phase elements
P	Power density
E	Energy density
Csp	Specific capacitance
a.u	Arbitrary unit
c.f	compare

LIST OF SYMBOLS

Symbol	Acronym
F	Farad
A	Ampere
V	Volts
W	watts
s	second
h	hour
Hz	Hertz
Rct	Charge-transfer resistance
Rs	Solution resistance
f_o	Knee frequency

CHAPTER ONE

1 INTRODUCTION

1.1 Background

Parallel to increasing demand for energy and power in applications, studies conducted in this field have also increased. According to annual reports from The World Energy Investment Outlook 2014, it is clear that the gap between energy demands and consumption keeps decreasing every year. The growing global concerns namely, growing carbon dioxide (CO_2) emission, the forever increasing mining cost and depletion of fossil fuels are driving forces for the development of alternative energy storage technology that is able to meet both current and future energy demands. The issues surrounding global energy require clean and sustainable energy.

Innovative approaches to address the issue and respond rapidly and reliably to the global energy needs have led to the discovery of electric devices. The primary goal for the development of electric devices was to provide source of power and energy especially in transportation. The discovery led to the development of hybrid electric vehicles and fuel cell vehicles, which have played a key role in reducing our dependence on soon to be depleted natural energy resources.
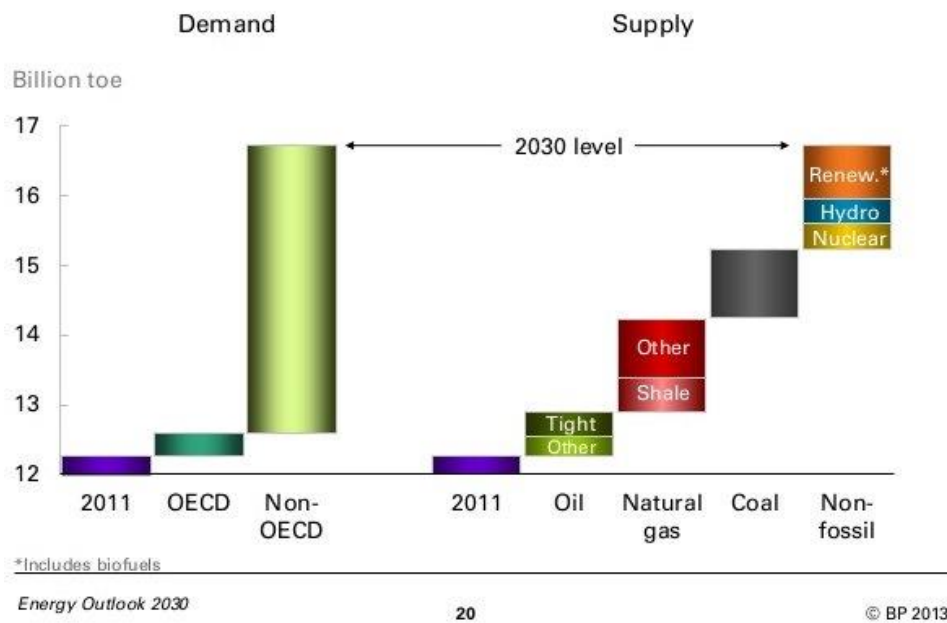
Figure 1.1 Schematic for energy demand vs supply from BP.

As it stands, batteries, fuel cells, conventional capacitors and supercapacitors are now dealing with energy conversion, storage and usage. Being the latest addition, supercapacitors have received a lot of attention mainly because they are able deliver high levels of electrical power, offer unlimited charge/discharge cycles, green environmental protection and have long operating lifetimes.[1] Inferior power capabilities coupled with high maintenance fee of other competing energy storage devices such as batteries and fuel cells has restricted their use.[2]

The concept of storing electrical energy in the electric double layer that is formed at the interface between an electrolyte and a solid can be traced back to the late 1800s.[3] The discovery of the first electrical device using double layer charge storage was first reported and patented by H.I. Becker of General Electric in 1957. Unfortunately, it was impractical, given that, both electrodes needed to be placed

in an electrolyte in a way resembling that of a battery. Subsequently, in 1966 researchers from Standard Oil of Ohio (SOHIO) accidently re-discovered this effect while working on experimental fuel cell designs. SOHIO also failed to commercialize the device and licensed it to the Nippon Electric Company (NEC). Furthermore, it took until 1978 for supercapacitors to be commercially available. Since then, supercapacitors have continually evolved through several generations of design.[3, 4, 5]

Supercapacitors have a good combination of properties which makes them very attractive for many applications. When used in electric vehicles, they supply power for acceleration that is in turn recuperated during breaking.[6] Supercapacitors are also used in parallel with batteries. This unique type of energy storage system uses supercapacitors to handle peak power in devices like laptops and a battery for handling the sustained load. [7, 8]

In spite of their superior properties, the widespread use of supercapacitors is still very limited. Unfortunately, supercapacitors suffer from high self-discharge and their energy densities are yet to match that of mid to high-end batteries (typically, 24 to 27 $Whkg^{-1}$).[9] Energy density refers to the amount of energy stored per unit mass or volume. Power density is the time it takes to deliver the energy per unit mass or volume. Both are crucial to handle the wide range of applications. Therefore, the biggest challenge in supercapacitors is the trade-off between energy density and power density. The limited charge accumulation in the electrical double layer restricts the specific capacitances of electric double layer capacitors (EDLCs) in a relatively small range. Nevertheless, pseudocapacitors are lost from

the poor electrical conductivity of electrode materials and the irreversibility of Faradaic reactions on the electrode surface, which cause gradual loss of capacitance.[9] This presents an opportunity to enhance electrochemical capacitance and stability of an electrode. The first approach is to develop nanostructured electrodes with extremely large effective area. Nanotubes, nanowires, nanosheets, and mesoporous nanostructures have been studied, and it was shown that nanostructures exhibit higher specific capacitances than their bulk counterparts[7]. The second approach is to increase the electrical conductivity of electrodes by mixing them with highly conductive materials. For instance, as excellent electrical conductors, carbon materials have been widely used to form composites with metal oxide electrodes[6]. Therefore, increased specific energy density is the major driving force for the improvement of supercapacitors.

In this current competitive environment supecapacitors need breakthrough materials which offer significant improvements. That is, materials that can facilitate multi-electron transfer per atom which increases the energy density significantly. Till recently, carbonaceous, transition metal oxides and conducting polymers were used as electrode materials for supercapacitors, with each providing unique features and benefits. One of the emerging high-power supercapacitor electrode materials is the molybdenum disulfide (MoS_2), a member of the transition-metal dichalcogenides (TMDs). MoS_2 has found applications in electrochemical devices, hydrogen storage, catalysis, capacitors, solid lubricants, and intercalation hosts.[10, 11] The MoS_2 is a layered-structured material with a close relationship to graphene, characterized by a sheet-like morphology. In molybdenum disulfides the atoms are arranged in a hexagonal close packed array

in which the metal atom is covalently bonded to six sulphur atoms at the vertices of a trigonal prism.The Mo layer is sandwiched between two S layers, and the triple layers are stacked and held together by weak van der Waals interactions.[12, 13] Due to it higher intrinsic fast ionic conductivity (than oxides) and higher theoretical capacity (than graphite), MoS_2 continues to attract a lot of attention, particularly in supercapacitors.[10, 12, 14] Subsequently, Soon and Loh[15] pointed out the use of MoS_2 as an electrode material for supercapacitors. The results suggest that the supercapacitor performance of MoS_2 is comparable to that of carbon nanotubes (CNT) array electrodes. In addition to double-layer capacitance, diffusion of the ions into the MoS_2 at slow scan rates gives rise to Faradaic capacitance. Analogous to Ru in RuO_2, Mo center atom displays a range of oxidation states from +2 to +6. This plays an important role in enhancing charge storage capabilities.[16] However, the electronic conductivity of MoS_2 is still lower compared to graphite, and the specific capacitance of MoS_2 is still very limited when used alone for energy storage applications.[14, 15, 17] As evident in several literature reports, there is a need to improve the capacitance of MoS_2 with conductive materials such as CNT,[14] polyaniline (PANI),[12] polypyrrole (PPy),[13] and reduced graphene (RGO).[18] In a review by Nieto-Marquez et al.,[19] carbon nanosphere (CNS) has been described as a good candidate for catalytic and adsorption applications, and whose unclosed graphitic flakes provide the necessary 'dangling bonds' that could enhance surface reactions. CNS has also been used to enhance the conductivity of battery cathode material, $LiFePO_4$.[20]

1.2 Objectives

This generation of electrical energy storage device lacks the capabilities to store large amounts of energy that are possible with batteries, has high rate of self-discharge, low operating potential and high equivalent series resistance. Carbon nanostructures are an interesting choice for supercapacitors, considering their low cost, accessibility, versatility, and high surface areas. However, in contrast to batteries, their energy densities are far less. On the other hand, pseudocapacitors have much higher capacities but due to poor cycling stability of CPs and metal oxides are rendered not suitable for commercialization. Although not financially practical, Ruthenium oxide is a good choice seeing that it has the unique combination of properties.

The main aim of this work is to explore nanostructured MoS_2 and CNS modified MoS_2 based composites as potential electrode material for supercapacitor applications. It is expected that incorporation of CNS with transition metal nanoparticles could tailor the properties of the electrode material and widen their utility in energy storage applications. Most importantly, this unique composite might potentially provide the much needed effective surface area and electrical conductivity for energy storage.

The following materials were hydrothermally synthesized, characterized and used as supercapacitor electrode materials.

- MoS_2 (spherical), MoS_2 (flower-like), MoS_2 (graphene-like), MoS_2 (hollow) and CNS

- s-MoS$_2$/CNS, f-MoS$_2$/CNS, g-MoS$_2$/CNS and h-MoS$_2$/CNS composites

The objectives of this work are;

- To increase the effective surface area by using nano-MoS$_2$ as opposed to bulk counterparts.

- To employ a simple cost-effective hydrothermal approach for synthesis of MoS$_2$ –based products.

- To modify MoS$_2$ with carbon nano-spheres from sucrose derived carbon-rich polysaccharides (SCP) by a simple in-situ hydrothermal method.

- To integrate the exfoliated g-MoS$_2$ and h-MoS$_2$ in solvent with CNS.

- To extensively investigate the s/f-MoS$_2$/CNS composite's chemical and physical properties as a novel electrode material by using the following techniques: Scanning Electron Microscope (SEM), Energy Dispersive X-Ray Spectroscopy (EDX), Transmission Electron Microscope (TEM), X-ray diffraction (XRD), Fourier Transform Infrared Spectroscopy (FTIR), Raman Spectroscopy, and Brunauer–Emmett–Teller (BET) surface area measurements.

- Investigation and optimization of performance parameters, such as specific capacitance, energy density, power density, operating voltage, equivalent series resistance (ESR) and stability of the fabricated supercapacitors using the synthesized materials.

- The measurements were carried out in 1 M Na$_2$SO$_4$ aqueous electrolyte. Cyclic Voltammograms (CV), galvanostatic charge/discharge and electrochemical impedance spectroscopy (EIS) were examined using a

7

Bio-Logic VMP 300 potentiostat/galvanostat. Additional electrochemical measurements were done using a three-electrode configuration which constitutes of active materials (MoS_2 or MoS_2/CNS) as the working electrode, platinum foam and Ag/AgCl electrodes as the counter and reference electrodes, respectively.

1.3 Limitations and Scope of Investigation

This work is limited to the synthesis of aforementioned materials using a hydrothermal technique with various chemical reagents and on the application of the composites as an electrode material. The main focus is to achieve large capacitance values which are not available in current literature while maintaining the high power characteristic of this device.

1.4 Plan of Development

The report begins with an introduction chapter that describes the background and motivation of study with objectives limitations and scope. Chapter 2 is a brief literature review, followed by chapter 3 which describes the experimental approach used to make and test the electrode materials. It then focuses on the results obtained in chapter 4 and 5, in which attention was then devoted to the behavior of these composites. Conclusions in chapter 6 were then drawn on the basis of the results and finally, recommendations made, based on the conclusions.

1.5 References

1. Gupta, R.; Sharma, N. K.; Tiwari, P.; Gupta, A.; Nigam, N.; Gupta, A. (2011) Application of Energy Storage Devices in Power Systems. *Science And Technology*, *3*, 289–297.

2. Whittingham, M. S. (2008) Materials Challenges Facing Electrical Energy Storage. *Harnessing Materials for Energy*, *33*, 411–419.

3. Miller, J. R.; Simon, P. (2008) Fundamentals of Electrochemical Capacitor Design and Operation. *The Electrochemical Society Interface*, *c*, 31–32.

4. Miller, J.R. (2007). HISTORY OF TECHNOLOGY A Brief History of Supercapacitors. *Battey+energy technologies*, *ISSN521452*, 61–78.

5. Jayalakshmi, M.; Balasubramanian, K. (2008) Simple Capacitors to Supercapacitors - An Overview. *International Journal of Electrochemical Science*, *3*, 1196–1217.

6. Stevic, Z.; Radovanovic, I. (2012) Energy Efficiency of Electric Vehicles. *New generation of electric vehicle*, http://dx.doi.org/10.5772/55237, 94-133.

7. Harrop, P.; Zervos, H. Batteries (2009) Alternative Storage for Portable Devices. INTERNET.www.idtechex.com cited 2 November 2015.

8. Shin, D.; Kim, Y.; Seo, J.; Chang, N.; Wang, Y.; Pedram, M. (2011) Battery-Supercapacitor Hybrid System for High-Rate Pulsed Load Applications. *Design, Automation & Test in Europe*, 1–4.

9. Lu, X.; Wang, G.; Zhai, T.; Yu, M.; Gan, J.; Tong, Y.; Li, Y. (2012) Hydrogenated TiO_2 Nanotube Arrays for Supercapacitors. *Nanoletters*, *12*, 1690–1696.

9

10. Huang, K. J.; Wang, L.; Liu, Y. J.; Liu, Y. M.; Wang, H. B.; Gan, T.; Wang, L. L. (2013) Layered MoS_2-Graphene Composites for Supercapacitor Applications with Enhanced Capacitive Performance. *International Journal of Hydrogen Energy*, *38*, 14027–14034.

11. Wang, S.; An, C.; Yuan, J. (2010) Synthetic Fabrication of Nanoscale MoS_2-Based Transition Metal Sulfides. *Materials*, *3*, 401–433.

12. Huang, K. J.; Wang, L.; Liu, Y. J.; Wang, H. B.; Liu, Y. M.; Wang, L. L. (2013) Synthesis of polyaniline/2-Dimensional Graphene Analog MoS_2 composites for High-Performance Supercapacitor. *Electrochimica Acta*, *109*, 587–594.

13. Ma, G.; Peng, H.; Mu, J.; Huang, H.; Zhou, X.; Lei, Z. (2013) In Situ Intercalative Polymerization of Pyrrole in Graphene Analogue of MoS_2 as Advanced Electrode Material in Supercapacitor. *Journal of Power Sources*, *229*, 72–78.

14. Huang, K. J.; Wang, L.; Zhang, J. Z.; Wang, L. L.; Mo, Y. P. (2014) One-Step Preparation of Layered Molybdenum Disulfide/multi-Walled Carbon Nanotube Composites for Enhanced Performance Supercapacitor. *Energy*, *67*, 234–240.

15. Soon, J. M.; Loh, K. P. (2007) Electrochemical Double-Layer Capacitance of MoS_2 Nanowall Films. *Electrochemical and Solid-State Letters*, *10*, A250.

16. Hu, B.; Qin, X.; Asiri, A. M.; Alamry, K. a.; Al-Youbi, A. O.; Sun, X. (2013) Synthesis of Porous Tubular C/MoS_2 Nanocomposites and Their Application as a Novel Electrode Material for Supercapacitors with Excellent Cycling Stability. *Electrochimica Acta*, *100*, 24–28.

17. Krishnamoorthy, K.; Veerasubramani, G. K.; Radhakrishnan, S.; Kim, S. J. (2014) Supercapacitive Properties of Hydrothermally Synthesized Sphere like MoS_2 Nanostructures. *Materials Research Bulletin*, *50*, 499–502.

18. Mandal, M.; Ghosh, D.; Kalra, S. S.; Das, C. K.; Centre, M. S.; Bengal, W. (2014) High performance supercapacitor electrode material based on flower like MoS$_2$/reduced graphene oxide. *International Journal of Latest Research in Science and Technology*, *3*, 65–69.

19. Nieto-m, A. (2011) Carbon Nanospheres : Synthesis , Physicochemical Properties and Applications. *Journal of Materials Chemistry*, *21,* 1664–1672.

20. Jiang, T.; Pan, W.; Wang, J.; Bie, X.; Du, F.; Wei, Y.; Wang, C.; Chen, G. (2010) Electrochimica Acta Carbon Coated Li$_3$V$_2$ (PO$_4$)$_3$ Cathode Material Prepared by a PVA Assisted Sol – Gel Method. *Electrochimica Acta*, *55*, 3864–3869.

CHAPTER TWO

2 LITERATURE REVIEW

2.1 Principles of energy storage

A conventional capacitor is formed from two conducting electrodes with a current collector on each electrode, a porous separator between the symmetrical electrodes and a solid/liquid electrolyte.[1] In principle, a voltage is applied to a capacitor and opposite charges accumulates on the surfaces of each electrode. Since the charges are kept separate by a dielectric, an electric field that allows the capacitor to store energy is produced. This first generation of capacitors is depicted in Fig.2.1.[2]

The capacitance of a capacitor is determined by the following equation:

$$C = \frac{Q}{V} \tag{1}$$

Where C is the capacitance [F] and Q [C] the charge to the applied voltage, V. For a conventional capacitor, each electrode has a surface area A [m^2] that is accessible to ions, separated from the other by a distance D [m] and the medium between the plates with a relative dielectric constant ε. Therefore, the capacitance can be further estimated by the following equation.[2]

$$C = \frac{\varepsilon^*}{D} A \tag{2}$$

ε^* is a product of the dielectric constant of free space ($\varepsilon_0 \approx 8.854 \times 10^{-12}$ [F/ m]) and the dielectric constant of the insulating material between the electrodes ($\varepsilon_r =$

1) . According to this equation, a significant increase in the capacitance value can be achieved by a high surface area electrode, a small distance between the electrodes and a large dielectric constant of the insulating material.[2]

Two most important attributes which are regarded as the basis of a capacitor are power density and energy density. Both densities are generally calculated as a quantity per unit mass or per unit volume. The energy E [W h/kg] stored in a capacitor is directly proportional to its capacitance as shown in equation (3).[3]

$$E = \frac{CV^2}{2} \tag{3}$$

Power P [W/kg] represents energy expended per unit time. It is known that capacitors are generally represented as a circuit in series with an external "load" resistance R. In addition, the internal components of the capacitor namely current collectors, electrodes, and dielectric material also contribute to the internal resistance and thus, are accounted for, by a quantity known as the equivalent series resistance (ESR) [Ohms]. The voltage that exists during discharge depends on these resistances. Therefore, the maximum power P_{max} for a capacitor measured at matched impedance (R=ESR) is given by equation (4)[4]

$$P_{max} = \frac{V^2}{4 \times ESR} \tag{4}$$

This so-called ESR also frequently referred to as the internal resistance is calculated as follows

$$R = \frac{\Delta V_{ir}}{2i} \tag{5}$$

13

ΔV_{iR} [V] is the voltage drop (iR drop) between the first two points of the discharge curve (Fig. 2.1), i [A] is the applied current.[2]
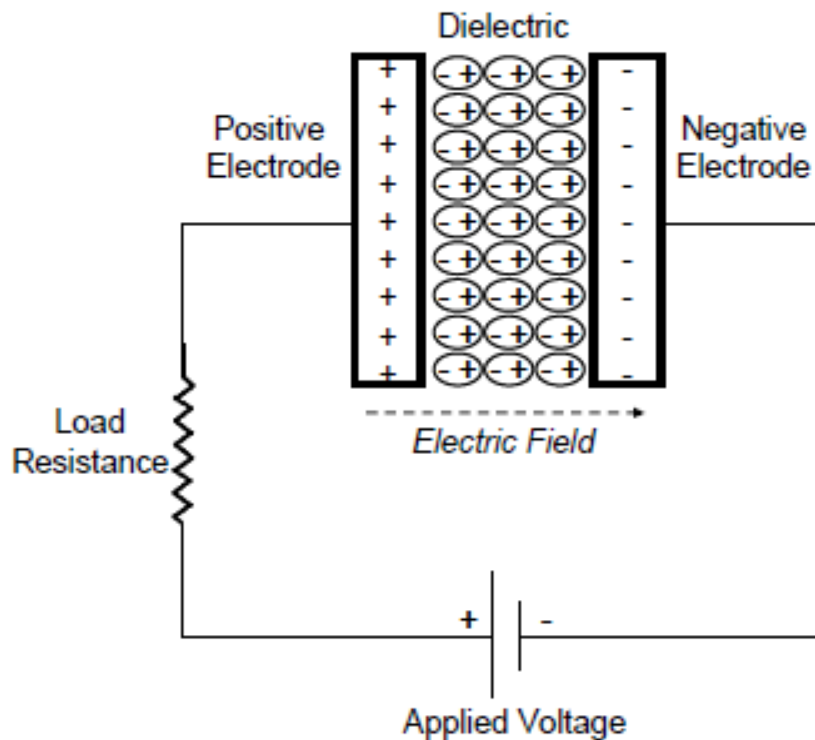
Figure 2.1. Schematic diagram of a conventional capacitor.[2]

Conventional capacitors are characterized by their high power density. Hence, they are of interest in various applications. Although they have much higher power densities compared to both batteries and fuel cells, they store much less energy per unit mass or volume. Based on recent development, supercapacitors, which are the second generation of capacitors, are most viable and therefore, hold more promise.[3]

A typical supercapacitor is also formed from the same basic structure as a conventional capacitor.[5] Only on this device, the ions in the electrolyte, governed by the law of attraction, diffuse across the separator into the pores of the electrode

of opposite charges, such that charge accumulates at the electrolyte/electrode interface of both electrodes as shown in Fig. 2.2.[3] The fundamental difference lies in the electrode material and charge accumulation mechanism. This invention aims to bridge the gap between conventional capacitors and other energy storage devices. These so-called supercapacitors rely on the high surface area (A) electrode materials in combination with much thinner dielectrics that decrease the distance (D) between the electrodes. Thus, according to equation (2) and (3) the capacitance and energy values are improved by several orders of magnitude. Moreover, the low ESR characteristic from conventional capacitors is maintained in supercapacitors, thus, enabling comparable power densities.[2]
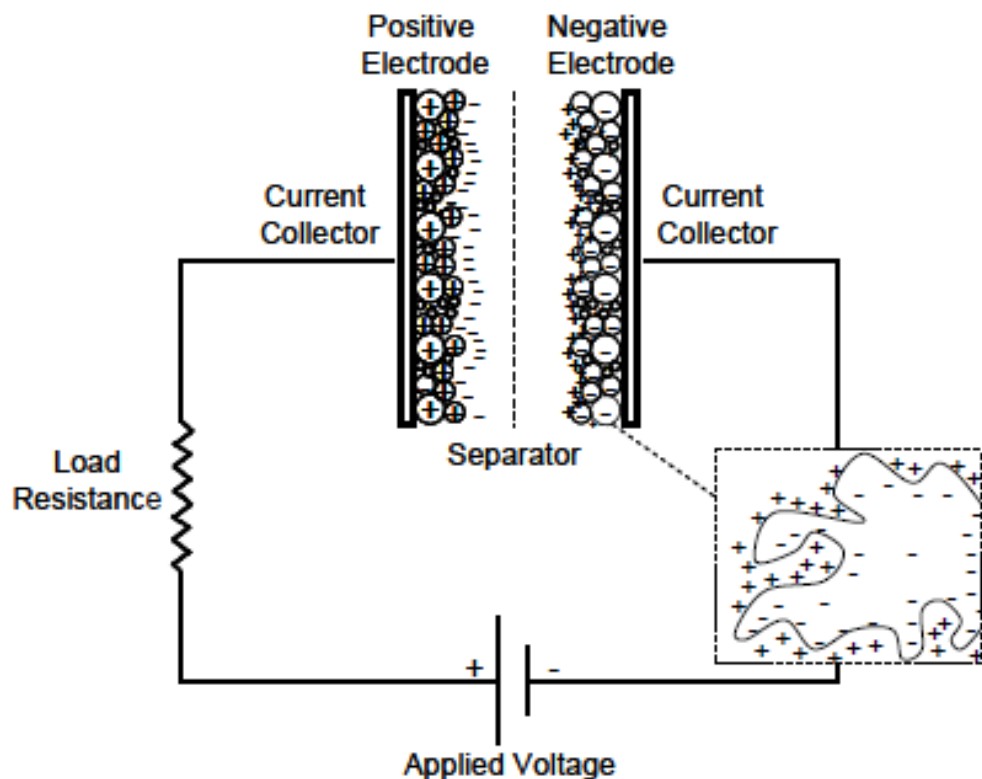
Figure 2.2. Schematic diagram of a supercapacitor.[22]

Early studies of the double layer model indicate that two layers of opposite charges are highly ordered at the electrode/electrolyte boundary, such that a double layer is formed. This Helmholtz model (shown in Fig. 2.3a) relies on the assumption that the double layer capacitance is independent of the diffusion of ions in the solution as well as the concentration of the electrolyte. Later, Gouy and Chapmen proposed a model that accounts for the influence of diffusion in which the applied potential decreases exponentially from the interface to the bulk electrolyte solution, see Fig 2.3b. However, this model neglects the highly charged double-layers.[6] An alternative model combines the two characteristics from Helmholtz and Gouy-Chapman models, namely; (i) the hydrodynamic motion of the ionic species in the diffuse layer and (ii) the accumulation of ions close to the electrode surface. This elegant and traceable model with aforementioned characteristics (Fig. 2.3c) was developed by Stern in 1924. Therefore, the total capacitance of the electrode C_{DL} is equivalent to the sum of two capacitors in series, where C_H represents the phenomena in the Helmholtz layer and C_D is the diffusion region capacitance.[7] This is to say,

$$\frac{1}{C_{DL}} = \frac{1}{C_H} + \frac{1}{C_D} \tag{6}$$
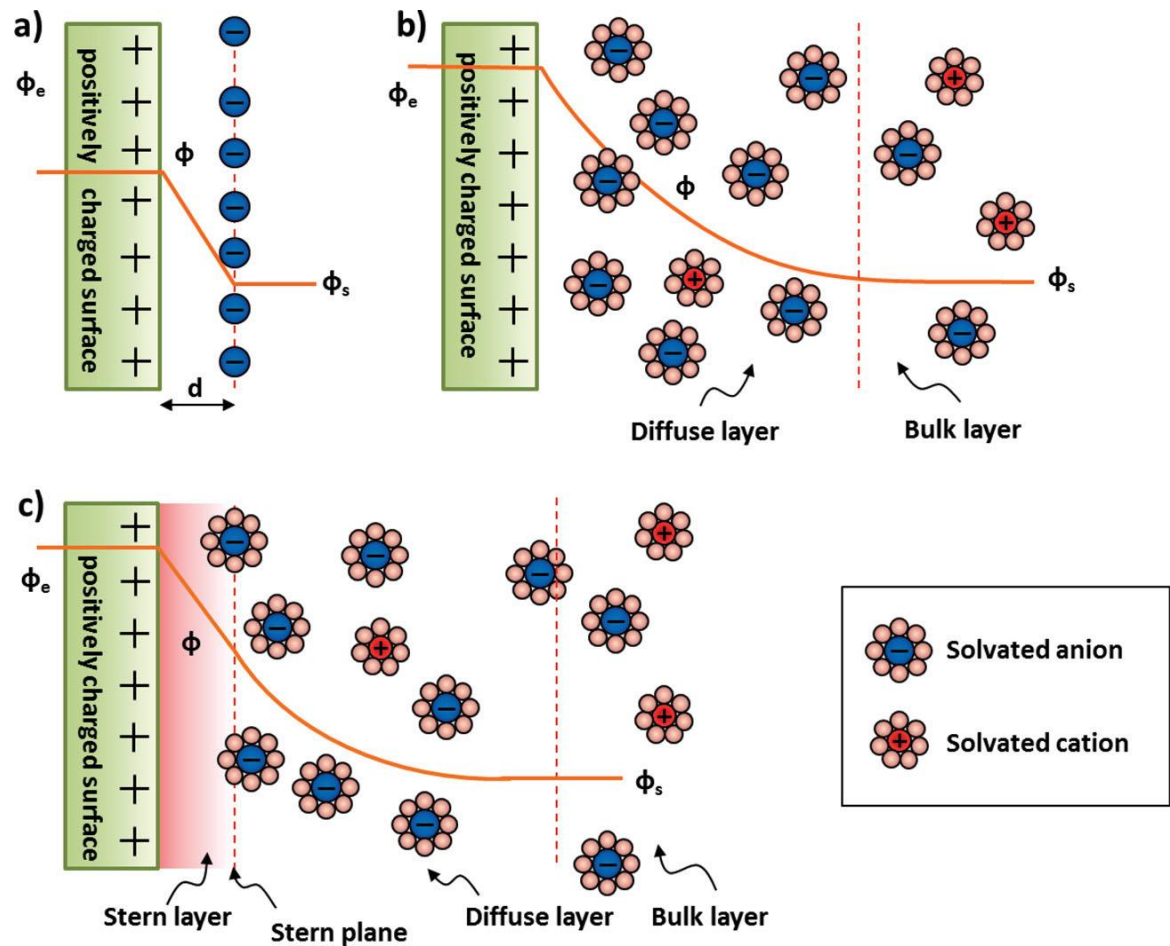
Figure 2.3. Schematic diagram of double layer models (a) Helmholtz model (b) Gouy-Chapman model (c) Stern model.[7]

2.2 Supercapacitors in general

Supercapacitor also referred to by many researchers as ultracapacitor, or electrochemical capacitor is a relatively new energy storage device that makes use

of high surface area electrode. They have received a lot of attention mainly because they are able to deliver high levels of electrical power and offer long operating lifetimes.[8] This makes them ideal for use in components where high specific power, faster charge-discharge rates and cycling stability are critical factors.[9] The performance of supercapacitors in relation to batteries and other energy storage and conversion devices is best described by the Ragone plot shown in Fig. 2.4 Illustrated in this graph is a plot of energy densities (along the horizontal axis) measured against power densities (along vertical axis) of various energy storage devices. According to this diagram, supercapacitors constitute a large region between batteries and conventional capacitors. Both batteries and fuel cells possess attributes of high theoretical specific energy, but their power density falls below the desired levels compared to supercapacitors.[3, 10] In simpler terms, they are able to store large amounts of total energy, but fail to deliver it very fast, like capacitors. For this reason, batteries and fuel cells are usually complimented with high power electric devices to overcome these deficiencies.[8] Despite the satisfactory power density, supercapacitors are yet to match the energy densities of batteries and fuel cells, reducing the competitiveness as a revolutionary energy storage device.[1] Conventional capacitors have the highest power density but store very little energy. The electrochemical properties of batteries and supercapacitors are listed and compared in Table 2.1.[5] According to the table, batteries have high energy density and suitable power density. Cycle life of a battery is narrow in comparison to supercapacitors due to faradaic processes that lead to constant phase or volume changes. On the other hand, supercapacitors with no chemical or compositional changes last longer since the charge-discharge motions are highly

reversible. During the last years, the power requirements of batteries increased for some applications. This led to the design and development of high power pulse batteries. Alternatively, these are used instead of supercapacitors.[11]
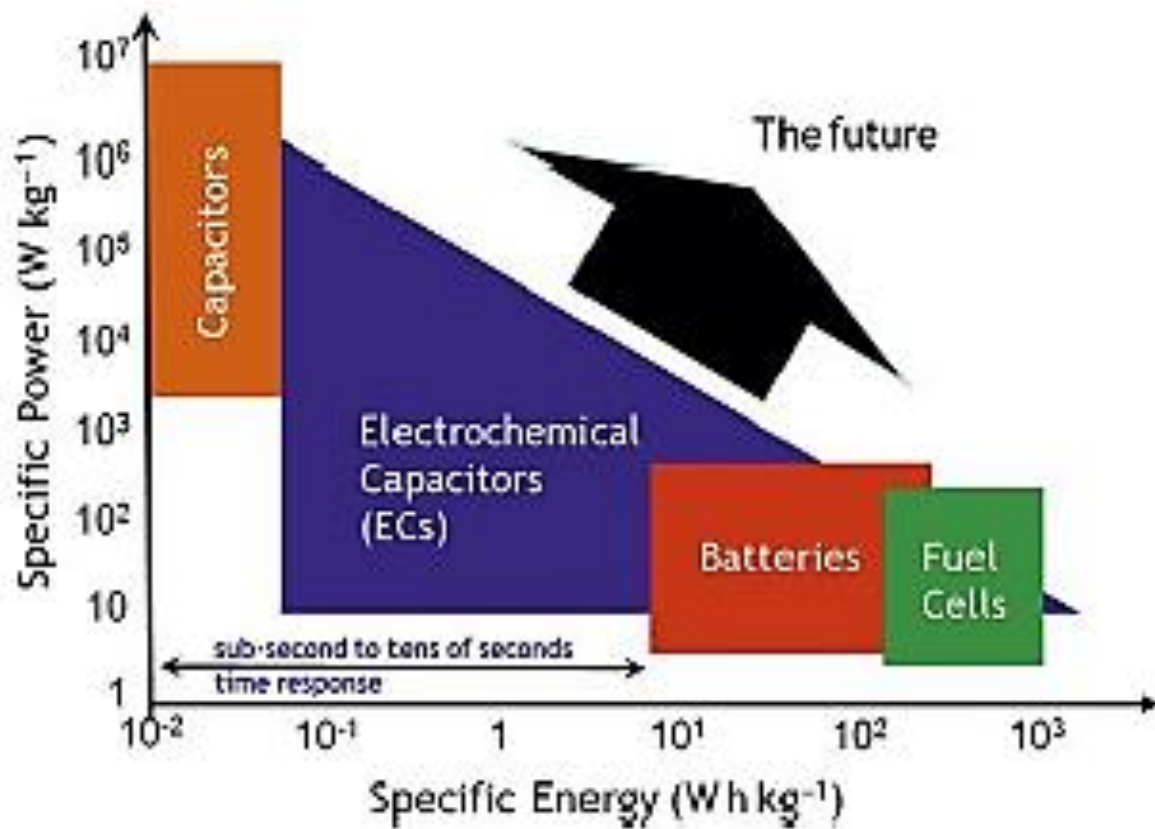
Figure 2.4. The Ragone plot illustrating energy density vs power density.[8]

Table 2.1 Batteries vs. supercapacitors characteristics.[5]

Attribute	Ultracapacitor	Batteries
Power Density	> 1000 W/kg	< 500 W/kg
Energy Density	< 5 Wh/kg	10-100 W/kg
Cold Temperature	< -40 ° C	-20 ° C
Hot Temperature	+65 ° C	+40 ° C
Efficiency	98%	95%
Charging time	Fraction of a several minutes	Several hours
Charging-discharging efficiency	88-98 %	70-85 %
self-discharging	Hours to days	Weeks to several months
Cycle life	10^6 - 10^8	200-1000
Lifetime	8-14 years	1-5 years
Toxicity	Non-toxic	Lead, strong Acid
Monitoring	Not required, simple voltage, current measurements	Sophisticated
Handling	Human handling	Requires equipment

2.3 Electrochemistry

Supercapacitors are classified according to their charge storage mechanism. Fig. 2.5 is showing different types with corresponding materials.

2.3.1 EDLCs

When voltage is applied, current is produced and charge accumulates on the surface of the electrodes. Governed by the law of attraction, opposite ions diffuse across a separator, into the pores of the electrode of opposite charge, thus, forming a double layer of charge on each electrode. The combination of double layer, high surface area and close separation of charges contribute to high energy densities in supercapacitors. Supercapacitors that primarily store energy at the electrolyte/carbon interface through reversible ion adsorption onto the carbon surface are called electric double-layer capacitors (EDLC).[12] Since there are no phase or volume changes associated with EDLC charge storage, the mechanism is completely reversible and highly efficient. In particular, EDLCs based on carbon materials can achieve long cycle life with unlimited charge-discharge cycles but exhibit relatively low specific capacitances. This is unlike batteries, whose performance deteriorates as cells continuously lose capacitance and gain series resistance.[8]

2.3.2 Pseudocapacitors

In contrast, those in which additional charge is produced by the fast reversible faradic transitions of active materials or conducting polymers are referred to as pseudocapacitors[12]. This phenomenon is accomplished through electrosorption,

reduction-oxidation and intercalation processes. In a pseudocapacitor, the charge transfer that occurs in the reaction is voltage-dependent. The voltage dependent charge-transfer can be dichotomized into two reactions; (a) redox reaction, and (b) adsorption of ions. In a redox reaction, an oxidant, ox, and reductant, red, of the form,

ox + ze⁻ =red, the potential, E, is given by the Nerst equation as

$$E = E_0 + RT/ZF \; \text{In} \; [\check{R}/1 - \check{R}] \tag{7}$$

In which, $\check{R}$ = [ox]/([ox] + [red]) (square brackets indicate concentration of species)

E_0 is the standard potential, R is the gas constant, T is the absolute temperature and F is the Faraday constant. The amount of charge, q, is denoted by the product zF, and is a function of potential, E. Mathematical differentiation of the above equation produces a pseudocapacitive relation. Although pseudocapacitors possess much higher capacitance, the continuous change in volume due to solid state mass transport limits the life of a pseudocapacitor.[3]

2.3.3 Hybrid capacitors

The third and final type is based on a combination of EDLCs and pseudocapacitors. The combination highlights only the favorable high power of the former and large energy density of the latter. For this reason, hybrid capacitors have achieved energy and power densities that are not possible with the individual

types. The electrode materials responsible for the excellent behavior of hybrid capacitors are: composite, asymmetric and battery type.[3]
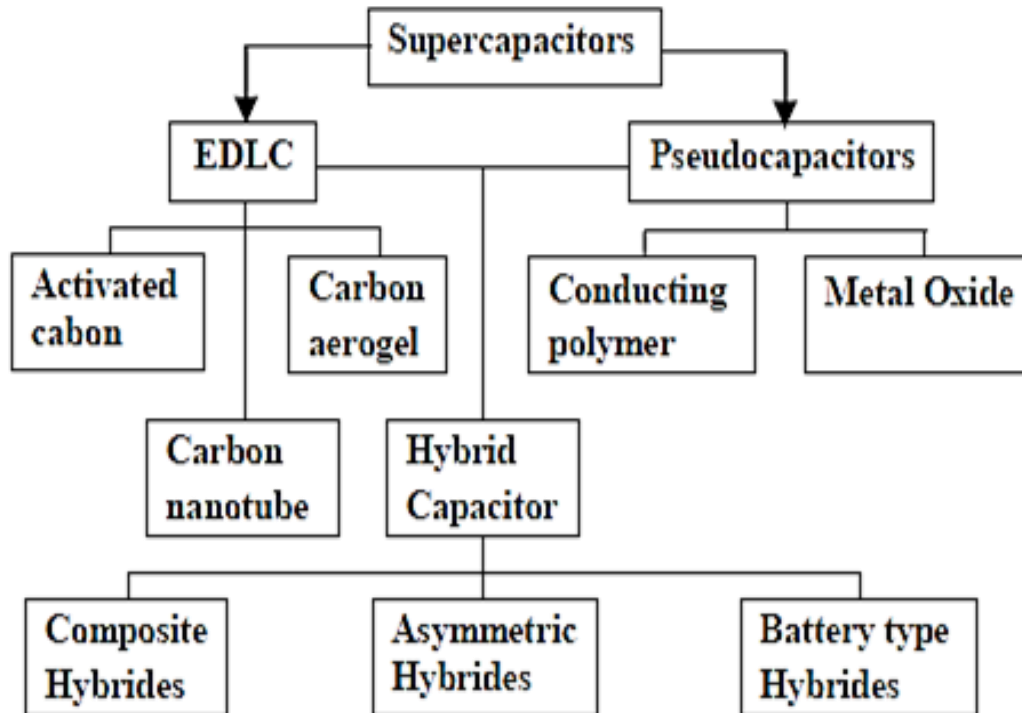
Figure 2.5. Classification of supercapacitors and related types.[3]

2.4 Electrode materials

There are several ways in which supercapacitors may be distinguished. Essentially, the performance of a supercapacitor depends on the type of electrode material used. This is best illustrated in Fig. 2.6. In general, they are grouped into three main classes: carbon-based, transition metal oxides and conducting polymers, with each electrode material providing unique features and benefits.[11]

At present, carbon currently dominates the market as an electrode material, while progress in the development of conducting polymers and metal oxides is continuing at a steady rate.[8]
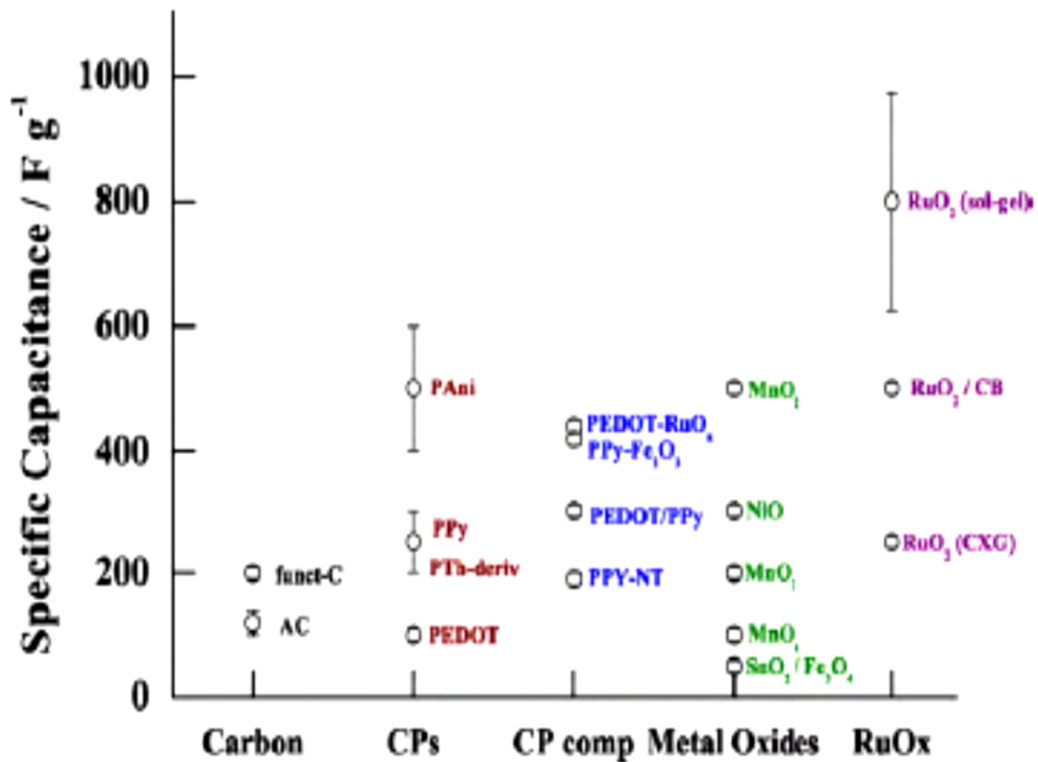
Figure 2.6. Typical electrode materials showing their specific capacitance.[11]

2.4.1   Carbon-based

Carbon is a unique element, seeing that it can exist in various structural forms, such as diamond, graphite, fullerene/nanotubes.[13] Among these, diamond and graphite are found naturally in earth's crust as minerals, whereas the other forms are synthetic. Advantage was taken to develop supercapacitors based purely on

carbon, as they exhibit outstanding long-term electrochemical stability as a result of high electrical conductivity and extraordinary chemical stability.

On the basis of recent advancements, it was shown that charge storage on carbon electrodes is predominantly capacitive in the electrochemical double layer. In that sense, carbon based materials are an interesting choice considering their low cost, accessibility, versatility, and lastly the high surface areas.[13] The large effective area makes it possible to store energy up to 2500 g/m.[2, 8] Other factors that contribute greatly to the specific capacitance and therefore the supercapacitors performance, include carbon structure, pore size and particle size. Additionally, the presence of some electrically conducting functional groups on activated carbons also gives rise to pseudocapacitance. Typically, carbon-based electrodes have specific capacitance between 50 and 170 Fg^{-1}. At present activated carbon, carbon aerogels and carbon nanotubes (CNTs) are often used in EDLCs. Different carbon structures have been explored in capacitor research and result in different properties, as is illustrated in Fig. 2.7.[14]
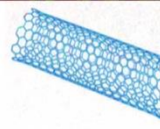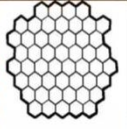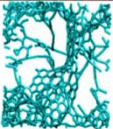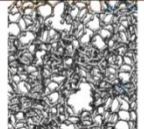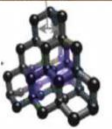
Material	Carbon onions	Carbon nanotubes	Graphene	Activated carbon	Carbide derived carbon	Templated carbon
Dimensionality	0-D	1-D	2-D	3-D	3-D	3-D
Conductivity	High	High	High	Low	Moderate	Low
Volumetric Capacitance	Low	Low	Moderate	High	High	Low
Cost	High	High	Moderate	Low	Moderate	High
Structure						

Figure 2.7. Various carbon structures used in EDLCs including Onion-like Carbon (OLC), Carbon Nanotubes, Graphene, Activated Carbons, and Carbide-Derived Carbon. [14]

2.4.2 *Metal oxide*

Metal oxides have also been explored as potential electrode materials. The results showed that they store much more energy than carbon-based electrodes. This effect is explained by the fast and reversible faradaic processes at the electrode surfaces, coupled with the non-faradaic formation of the electric double layer. Metal oxides such as RuO_2, Co_3O_4, Fe_3O_4, MnO_2, amongst others, have received tremendous attention due to their capacitive characteristics and green environmental protection[14].

The capacitance of ruthenium oxide is achieved, through the insertion and removal, or intercalation, of protons into its amorphous structure, as presented below in equation (8).[8] In it hydrous form, RuO_2 is able to exceed the specific capacitance of carbon materials using double layer charge storage. Furthermore, the ESR of RuO_2 is lower than that of carbon-based and conducting polymer materials. As a result, RuO_2 provides higher charge density and better

electrochemical stability[1]. However, the cost of RuO_2 is high compared to its competing materials, primarily conventional carbon and polymer materials. The high intrinsic cost restricts these supercapacitors from reaching their potential. Consequently, much effort has been devoted to the development of fabrication methods and composite materials that will reduce the cost of RuO_2 without sacrificing its properties.[8, 13, 15]

$$RuO_2 + xH+ + xe- \leftrightarrow RuO_2-x(OH)x \qquad (8)$$

2.4.3   Polymers

Alternative to transition metal oxides, pseudocapacitors make use of electronically conducting polymer (ECPs) materials. Typically, these consist of polyaniline, polypyrrole and polythiophene, etc. The primary advantages of ECPs include the large specific capacitance, high conductivity, low cost and a wide range of possible configurations.[16] These configurations are: (I) a symmetric supercapacitor based on a p-doped ECP, (II) an asymmetric supercapacitor based on two p-doped ECPs that are dopable over different potential ranges, and (III) a symmetric supercapacitor with a p- and n-doped ECP. Configuration III is the most promising in terms of energy and power density. One significant drawback of these materials is the difficulty to obtain efficient, n-doped ECPs.[15] Moreover, it has been reported that, similar to batteries, the charge-discharge process of polymer electrodes involves (doping/de-doping) insertion-deinsertion of ions. In this process, a polymer is reversibly oxidised and reversibly reduced as shown by

the equations (9) and (10). The continuous change in physical structure leads to degradation of the electrode during cycling redox reactions. These factors have hindered the wide use of ECPs pseudocapacitors. Recent ECP research with regards to supercapacitor applications is directed towards hybrid vehicles.[17]

$$Cp \rightarrow Cpn+(A-)n+ne-(\text{p-doping}) \tag{9}$$

$$Cp+ne- \rightarrow (C+)nCpn-(\text{n-doping}) \tag{10}$$

2.4.4 Composite

In this type of material carbon related materials are mixed with CP or metal oxides to form a composite that is later cast on a single electrode.[2]

2.4.5 Asymmetric

These capacitors employ one electrode comprised of carbon based material, non-faradaic, and the other with either a conducting polymer of metal oxide, faradaic.[2]

2.4.6 Battery type

Here, one electrode is a typical supercapacitor electrode and the other is battery like. This invention aims to bridge the gap between energy and power density between batteries and supercapacitors. Evidently, this invention adopts the cycle

life and charge-discharge times of a supercapacitor. Main examples of electrode materials include nickel hydroxide, lead dioxide and LTO.[2]

2.5 Electrolytes

The nature of an electrolyte displays an amazing diversification from solid, organic to aqueous type. Electrolytes that decompose at high voltages restrict the cell voltage of a supercapacitor to about 1 V. This is often the case with aqueous electrolytes due to thermodynamic electrochemical properties of water (1.23 V). Aqueous electrolytes solutions are usually derived from KOH, Na_2SO_4 and H_2SO_4. Advantages include high conductivity, low cost and accessibility. The organic electrolyte is derived from a quaternary salt dissolved in organic solvent such as acetonitrile (ACN) or propylene carbonate (PC). Operating cell voltages are above 2.5 V. Moving from aqueous to organic electrolytes increases the energy density approximately by a factor of four. This in turn, has greatly influenced current research studies to shift from aqueous to organic electrolytes. However, these may still suffer from low conductivity, in which case the ESR increases. In applications where power density is a requirement, this may not be ideal. In essence, the electrolyte should therefore provide high conductivity, adequate electrochemical stability to allow the capacitor being operated to reach the highest possible voltages. Recently ionic liquid (solvent-free) electrolytes were established due to their stability in wide voltage windows. However, they still suffer from various limitations. The appropriate electrolyte is chosen according to the intended application of the supercapacitor.[8]

2.6 Separators

Separators also contribute to the performance of a supercapacitor. It is also interesting to note that organic electrolytes utilize polymers or paper as separators. On the other hand, aqueous electrolytes employ glass fiber or ceramic separators. The main role of a separator is to allow movement of charged ions in the electrolyte solution between the electrodes whilst avoiding electronic contact between the electrodes.

The key to a successful supercapacitor device lies in the following performances: high ionic electrolyte conductance, high electronic separator conductance, high electronic separator resistance, high electrode electronic conductance, large electrode surface, low separator and electrode thickness.[18]

2.7 Applications

The application of supercapacitors accelerated when its potential as a high power density, environmentally friendly energy storage device was widely recognized. Supercapacitors can be used as powerful tools for short-term energy storage applications. They are mainly used in high power devices for energy storage systems, voltage stabilizers, portable electronics, power failure protection, pulsed lasers, satellite antennas, space communication systems, starters in motor vehicles , medical devices, electronic fuses in the mining industry and smart weapons, with the hybrid electric vehicle being the largest consumer of supercapacitors. In

addition, the minimum ESR, associated with supercapacitors allows for this device to be charged with a very high current. This novel feature makes supercapacitors ideal in regenerative braking applications where high charging current profile is needed to absorb energy from braking. Such a phenomenon is not possible for batteries with high ESR where current must be limited to avoid overheating. Initially, supercapacitors were designed to boost batteries or the fuel cell. Now they can be independently adapted to serve in roles which electrochemical batteries are not as well suited, for example memory back-up in computers, displays, video recorders, solar watches and toys.[19]

2.8 Molybdenum sulphides

Considerable recent capacitor research has also focused on the transition-metal dichalcogenides (TMDs), such as tungsten disulfide (WS_2) and molybdenum disulfide (MoS_2), as potential electrode materials. The emerging interest stems from the increasing demand to develop novel materials for supercapacitor applications.[20] Practically, electrochemical devices, hydrogen storage, catalysis, capacitors, solid lubricant, and intercalation hosts, have benefited from the discovery of MoS_2.[21] For some known reason, transition metals with unfilled d-shells show advantageous physical and chemical properties which allows their application in numerous industries.

Naturally occurring molybdenum sulphide is extracted from its core molybdenite. This is present in most high temperature hydrothermal ore deposits.[22] Analogous

to graphite, they are characterized by a sheet-like morphology. In this layered-structure, the atoms are arranged in a hexagonal close packed array in which the metal atom is covalently bonded to six sulphur atoms at the vertices of a trigonal prism. Subsequently, the Mo layer is sandwiched between two S layers, and the triple layers are stacked and held together by weak van der Waals interactions (Fig.2.8).[23] Depending on the method of preparation, MoS_2 is able to exist in different allotropes as nanorods, nanostripes, nano-tubes and fullerene like particles.[24]
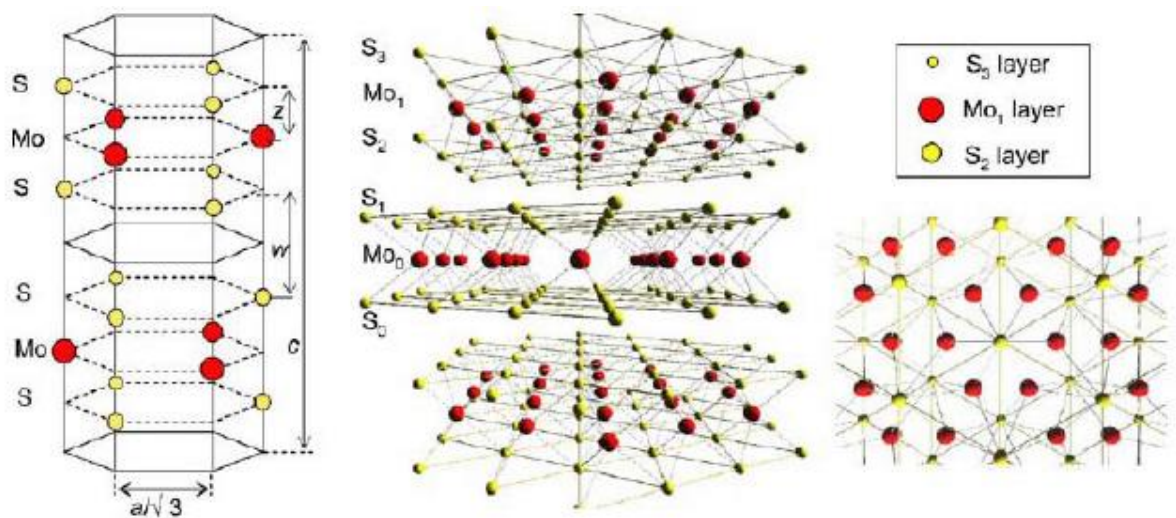
Figure 2.8. Layered atomic structure of MoS_2.**[24]**

There are several ways in which MoS_2 can be synthesized. From complex high temperature reactions involving a combination of elements or gas solid reactions between oxides and a reducing H_2S or S atmosphere, to a simple hydrothermal route that does not require extreme temperatures or pressure. In the past decade

alone, there has been a lot of reports on the synthesis of MoS_2 using both organic and inorganic compounds. Of these, the hydrothermal approach is regarded the most viable.[24]

MoS_2 is the most studied TMD due to its high intrinsic fast ionic conductivity (higher than oxides) and high theoretical capacity (higher than graphite). MoS_2 has attracted a lot of attention as an electrode material, particularly in Lithium ion batteries and supercapacitors. In fact, Soon and Lohz[25] reported the use of MoS_2 as an electrode material for capacitors. The results suggest that the supercapacitor performance of MoS_2 is comparable to that of CNT array electrodes. Double layer capacitance forms between and within the layers of MoS_2 sheets. In addition to double-layer capacitance, diffusion of the ions into the MoS_2 at slow scan rates gives rise to faradaic capacitance. Similar to Ru in RuO_2, the Mo centre atom displays a range of oxidation states (+2 to +6) which plays an important role in enhancing charge storage capabilities.[25] However, the electronic conductivity of MoS_2 is still lower compared to graphite/Gr, and the specific capacitance of MoS_2 is still very limited in alone usage for energy storage applications. The combination of MoS_2 with other conducting materials such as polymers, CNTs, graphite, etc. may overcome such deficiencies (schematic in Fig. 2.9).[20, 26] The specific capacitance and other performance studies for MoS_2 composites are summarized in table 2.2.
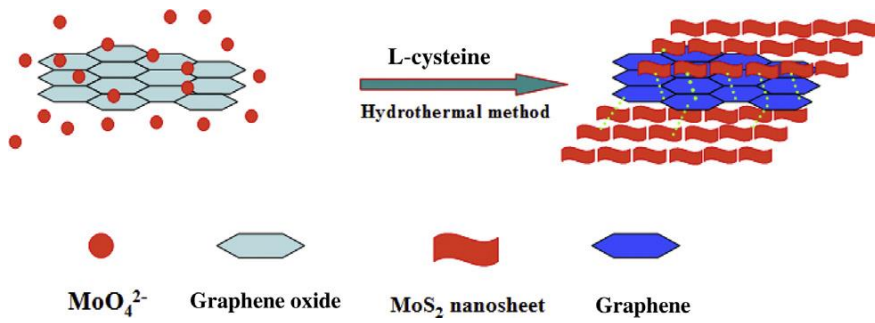
Figure 2.9. Schematic for the preparation of MoS$_2$/Graphene composite.[20]

Table 2.2 Comparison values of MoS$_2$ and its composites in 3 electrode configurations for supercapacitors.

Electrode Material	Electrolyte	Current density	Csp	Energy density	Power density	Reference
MoS$_2$	1 M Na$_2$SO$_4$	1 A/g	92.85 F/g	7.25 Wh/kg	186.5 W/kg	27
PANI/MoS$_2$	1 M H$_2$SO$_4$	1 A/g	575 F/g	265 Wh/kg	18 kW/kg	26
PPy/MoS$_2$	1 M KCl	1 A/g	553.7 F/g	49 Wh/kg	400 W/kg	28
MoS$_2$-graphene composite	1 M Na$_2$SO$_4$	1 A/g	243 F/g	85 Wh/kg	7600 W/kg	20
MoS$_2$/MWCNT	1 M Na$_2$SO$_4$	1 A/g	452.7 F/g	-	-	29
Porous tubular C/MoS$_2$	3 M KOH	1 A/g	210 F/g	-	-	30

In 1942, Wildervank and Jellinek conducted a thermal decomposition study on as-synthesized MoS_2 black precipitate using X-ray diffraction, diffractograms are shown in fig2.10. In doing so, they found that the obtained product is in excess of Sulphur which is easily removed from the matrix when heating above 250 °C. However, the product is still amorphous up to 350 °C. They go on to suggest that crystallization begins at 400 °C according to their DTA measurements. At this point, the moist MoS_3 begins to release various gases (S, H_2S, NH_3, etc.) and the composition is either $MoS_{2.4}$ or $Mo_{0.83}S_2$. At 500 °C broad diffraction peaks with positions corresponding to (002) (103) and (105) lines of hexagonal MoS_2 were present. This was due to stacking of layers in a random orientation. Further annealing between 800 and 1000 °C favors hexagonal MoS_2 with stacking faults. At 1100 °C the crystallinity was found to be comparable to the level of natural molybdenite.[22]
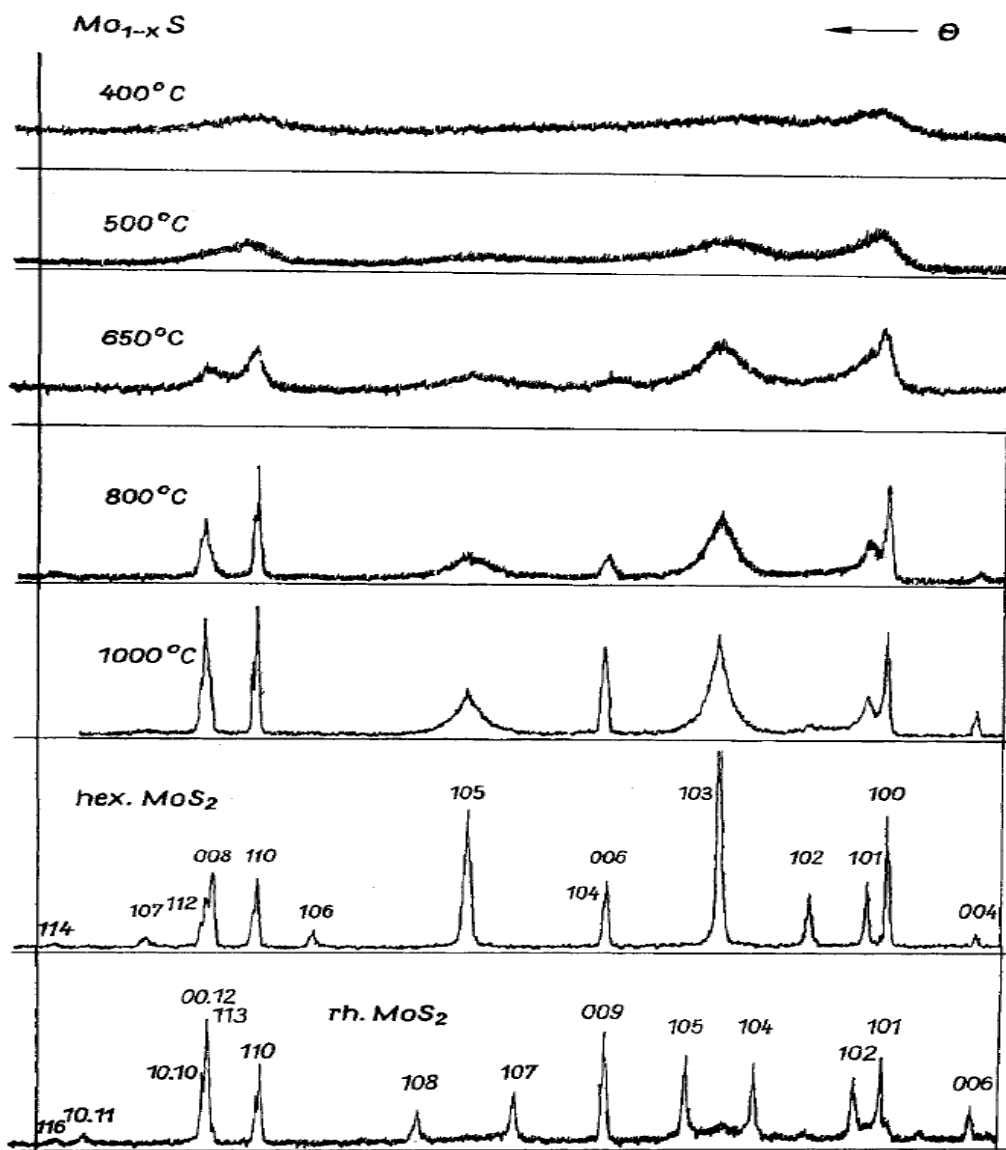
Figure 2.10. Diffractogram of products obtained from thermal decomposition of

MoS_3 at various temperatures.[22]

2.9 References

1. Jayalakshmi, M.; Balasubramanian, K. (2008) Simple Capacitors to Supercapacitors - An Overview. *International Journal of Electrochemical Science*, *3*, 1196–1217.

2. Ellenbogen, J. C.; Halper, M.S. (2006) Supercapacitors : A Brief Overview. MITRE Report No. MP 05W0000272.

3. Mohapatra, S.; Acharya, a; Roy, G. S. (2012) The Role of Nanomaterial for the Design of Supercapacitor. *Latin-American Journal of Physics Education*, *6*, 380–384.

4. Yadav, V.K.; Bhardwarj, N. (2013) Introduction to Supercapacitors and Supercapacitor Assisted Engine Starting System. *International Journal of Scientific & Engineering Research*, 4, 583-588.

5. Mallika, S.; Saravana Kumar, R. (2011) Review on Ultracapacitor- Battery Interface for Energy Management System. *International Journal of Engineering and Technology*, *3*, 37–43.

6. Endo, M.; Takeda, T.; Kim, Y. J.; Koshiba, K.; Ishii, K. (2001) High Power Electric Double Layer Capacitor (EDLC's); from Operating Principle to Pore Size Control in Advanced Activated Carbons. *Carbon Science*, *1*, 117–128.

7. Béguin, F.; Presser, V.; Balducci, A.; Frackowiak, E. (2014) Carbons and

Electrolytes for Advanced Supercapacitors. *Advanced Materials*, *26*, 2219–2251.

8.   Ko, R.; Carlen, M. (2000) Principles and Applications of Electrochemical Capacitors. *Electrochimica Acta*, *45*, 2483–2498.

9.   Burke, A. (2000) Ultracapacitors: Why, How, and Where Is the Technology. *Journal of Power Sources*, *91*, 37–50.

10.   Scherson, D. A.; Palencsár, A. (2006) Batteries and Electrochemical Capacitors. T*he Electrochemical Society Interface,* 1827, 17-22.

11.   Chen, K.; Xue, D. (2014) Ionic Supercapacitor Electrode Materials: A System-Level Design of Electrode and Electrolyte for Transforming Ions into Colloids. *Colloids and Interface Science Communications*, *1*, 39–42.

12.   Pandolfo, A. G.; Hollenkamp, A. F. (2006) Carbon Properties and Their Role in Supercapacitors. *Journal of Power Sources*, *157*, 11–27.

13.   Frackowiak, E.; Béguin, F. (2001) Carbon Materials for the Electrochemical Storage of Energy in Capacitors. *Carbon*, *39*, 937–950.

14.   Simon, P.; Gogotsi, Y. (2013) Carbon À Electrolyte Systems. Capacitive Energy Storage in Nanostructured Carbon–Electrolyte Systems. *American Chemical Society*, *46*, 1094.

15.   Simon, P.; Gogotsi, Y. (2008) Materials for Electrochemical Capacitors.

Nature Materials, *7*, 845–854.

16. Snook, G. a.; Kao, P.; Best, A. S. (2011) Conducting-Polymer-Based Supercapacitor Devices and Electrodes. *Journal of Power Sources*, *196*, 1–12.

17. Mastragostino, M.; Arbizzani, C.; Soavi, F. (2001)Polymer-Based Supercapacitors. *Journal of Power Sources*, *97-98*, 812–815.

18 Schneuwly, A.; Gallay, R. (2000) Properties and Applications of Supercapacitors From the State-of-the-Art to Future Trends., Proceeding PCIM, 1–10.

19. Trasatti, S.; Kurzweil, P. (1994) Electrochemical Supercapacitors as Versatile Energy Stores. *Platinum Metals Review*, *38*, 46–56.

20. Huang, K. J.; Wang, L.; Liu, Y. J.; Liu, Y. M.; Wang, H. B.; Gan, T.; Wang, L. L. (2013) Layered MoS_2-Graphene Composites for Supercapacitor Applications with Enhanced Capacitive Performance. *International Journal of Hydrogen Energy*, *38*, 14027–14034.

21. Feng, C.; Ma, J.; Li, H.; Zeng, R.; Guo, Z.; Liu, H. (2009) Synthesis of Molybdenum Disulfide (MoS_2) for Lithium Ion Battery Applications. *Materials Research Bulletin*, *44*, 1811–1815.

22. Jellinek, F.; W. J. C. (1964) Preparation and Crystallinity of Molybdenum and Tungsten Sulfides. *American Chemical Society*, *328*, 309–318.

23.   Afanasiev, P.; Xia, G.-F.; Berhault, G.; Jouguet, B.; Lacroix, M. (1999) Surfactant-Assisted Synthesis of Highly Dispersed Molybdenum Sulfide. *Chemistry of Materials*, *11*, 3216–3219.

24.   Wang, S.; An, C.; Yuan, J. (2010) Synthetic Fabrication of Nanoscale MoS_2-Based Transition Metal Sulfides. *Materials*, *3*, 401–433.

25.   Soon, J. M.; Loh, K. P. (2007) Electrochemical Double-Layer Capacitance of MoS_2 Nanowall Films. *Electrochemical and Solid-State Letters*, *10*, A250.

26.   Huang, K. J.; Wang, L.; Liu, Y. J.; Wang, H. B.; Liu, Y. M.; Wang, L. L. (2013) Synthesis of polyaniline/2-Dimensional Graphene Analog MoS_2 composites for High-Performance Supercapacitor. *Electrochimica Acta*, *109*, 587–594.

27.   Krishnamoorthy, K.; Veerasubramani, G. K.; Radhakrishnan, S.; Kim, S. J. (2014) Supercapacitive Properties of Hydrothermally Synthesized Sphere like MoS_2 Nanostructures. *Materials Research Bulletin*, *50*, 499–502.

28.   Ma, G.; Peng, H.; Mu, J.; Huang, H.; Zhou, X.; Lei, Z. (2013) In Situ Intercalative Polymerization of Pyrrole in Graphene Analogue of MoS_2 as Advanced Electrode Material in Supercapacitor. *Journal of Power Sources*, *229*, 72–78.

29.   Huang, K. J.; Wang, L.; Zhang, J. Z.; Wang, L. L.; Mo, Y. P. (2014) One-

Step Preparation of Layered Molybdenum Disulfide/multi-Walled Carbon Nanotube Composites for Enhanced Performance Supercapacitor. *Energy*, *67*, 234–240.

30.   Hu, B.; Qin, X.; Asiri, A. M.; Alamry, K. a.; Al-Youbi, A. O.; Sun, X. (2013) Synthesis of Porous Tubular C/MoS$_2$ Nanocomposites and Their Application as a Novel Electrode Material for Supercapacitors with Excellent Cycling Stability. *Electrochimica Acta*, *100*, 24–28.

CHAPTER THREE

This chapter gives detailed information of the experiment equipment and work procedures. The hydrothermal synthesis method is regarded as most viable and cost-effective for producing large scale MoS_2/CNS composites. As a preliminary study, MoS_2 were synthesized using different precursors available in the literature.

3 EXPERIMENTAL: MATERIALS AND METHOD

3.1 Materials

Sodium molybdate dihydrate ($Na_2MoO_4 \cdot 2H_2O$, Analytical Reagent BDH chemicals Ltd, Poole England), thiourea (CH_4N_2S, Sigma-Aldrich Inc, USA), polyethylene glycol 1000, (*PEG-1000*, Fluka Analytical, Germany), L-cysteine ($C_3H_7NO_2S$, Sigma-Aldrich Inc, USA), Molybdenum Trioxide (*MoO_3*, Analytical Reagent, Hopkin & Williams Ltd, London), Potassium Thiocyanate (*KSCN*, SAARCHEM PTY (Ltd) RSA), and Sucrose ($C_{12}H_{22}O_{11}$, Sigma-Aldrich Inc, USA). Solvents; hydrochloric acid (*HCl*) 32%, Acetone (C_3H_6O) and absolute ethanol (C_2H_6O) were purchased from Associated Chemical Enterprises, in Johannesburg. All chemicals had purity higher than 98.99%. Distilled de-ionised water (18 MΩ.cm) used in this study were generated from the School of Chemistry at the University of the Witwatersrand.

3.2 Synthesis of MoS$_2$ nanostructures

MoS$_2$ nanosheets were prepared using hydrothermal synthesis. In this work, four variants with different starting materials were mixed appropriately to reach the target composition.

3.2.1   Spherical MoS$_2$

Spherical MoS$_2$ was synthesized using a well-established method by Huang et al.[1] as follows: 0.31 g Na$_2$MoO$_4$·2H$_2$O were dissolved in 30 ml deionized water. After adjusting the pH value to 6.5 with 12 M HCl, 0.82 g L-cysteine was added and the mixture was diluted with water to 35 ml, and then the solution rapidly stirred for about an hour. Subsequently, the mixture was transferred into a 40 ml Teflon-lined stainless steel autoclave and heated at 180 °C for 48 hours. The black MoS$_2$ precipitate was cooled naturally to room temperature, collected by centrifugation, washed with distilled water and absolute ethanol in three cycles, and then dried in vacuum at 60 °C for 24 hours. For simplicity, the obtained layered material (as evident from SEM images) is abbreviated as **s-MoS$_2$**.

3.2.2   Flower-like MoS$_2$

This was synthesized as suggested by Wang et al.[2] 1.21 g Na$_2$MoO$_4$•2H$_2$O, 1.56 g thiourea powders were mixed together sufficiently in 30ml deionised water, and 0.14 g PEG-1000 added. The resulting mixture was transferred in a Teflon cup of capacity 40ml and heated in a stainless steel autoclave at 180 °C for 24 h. After cooling naturally to room temperature, the black MoS$_2$ precipitates were collected by centrifugation, washed with distilled water and absolute ethanol in three

cycles, and then dried in vacuum at 60 °C for 24 h. The flower-like material (as evident from SEM analysis) obtained is abbreviated herein as **f-MoS$_2$**.

3.2.3 Graphene-like and hollow MoS$_2$

Synthesis of graphene-like MoS$_2$ (g-MoS$_2$) and hollow MoS$_2$ (h-MoS$_2$)

The g-MoS$_2$ sample was synthesized using a method by Matte *et al*. with few modifications.[3] Briefly, 1 mmol (0.61 g) of MoO$_3$ and 2.5 mmol (1.94 g) of KSCN were mixed in 30 ml of deionized water, rapidly stirred for 1 h and transferred into a 40 ml Teflon cup. The mixture is then heated with continuous stirring in a stainless steel autoclave for 24 h while maintaining a temperature of 180 °C. A black precipitate is first retrieved from the solution, and washed with distilled water three times, then dried in vacuum at 60°C for 6 h. The hollow MoS$_2$ rods were synthesized in a similar way, except the solvent used was a mixture of 15 ml de-ionised water and 15 ml acetone.

3.3 Annealing

Following XRD analysis of the as-synthesized materials, the precipitates were amorphous in nature and thus, subject to homogenization treatment. These were annealed using a horizontal furnace with a controlled heating rate in a quartz tube. The optimum temperature was found to be 900°C for the duration of 4 hours under a flow of nitrogen at a rate of 100 ml/minute. The heating rate was 6 °C per minute. Fig. 3.1 shows a temperature profile for annealing the products. This was done to homogenize the as-synthesized MoS$_2$ and promote further crystallization.
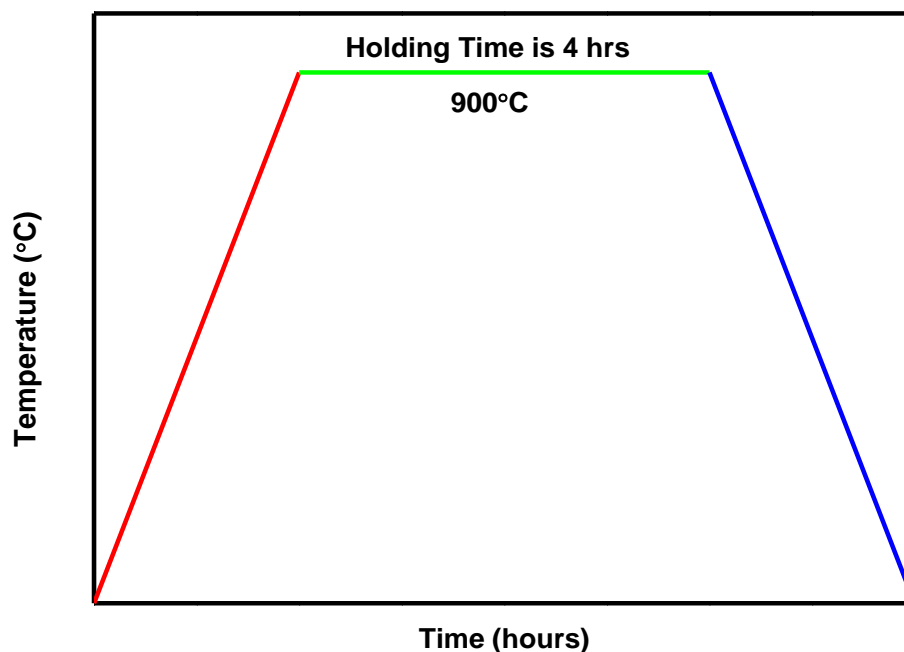
Figure 3.1. Temperature profile for annealing MoS_2, CNS and MoS_2/CNS nanocomposites

3.4 Characterization techniques

3.4.1 X-ray powder diffraction

MoS_2 based nanopowders were characterized structurally by means of powder X-ray diffraction (PXRD) using a Bruker Lynxeye PSD diffractometer. Powders were lightly ground (using mortar and pestle) and carefully transferred to a Si sample holder. Every sample was compressed with a glass slide and placed inside the instrument. The X-Ray diffraction patterns were obtained at room temperature

over the 2θ range of 10-90° using Co radiation (λ=1.78897 Å). Qualitative phase analysis was recorded using the OriginPro 8.5 software.

3.4.2   Brannauer Emmett and Teller

The specific surface area of the nanopowders was measured using 5 point analysis Brannauer Emmett and Teller (BET) method. This method relies on the adsorption of nitrogen gas onto the surface of nanopowders at a given pressure. Prior to analysis, samples were degassed in order to remove unwanted vapours and gases adsorbed on the surface for 4 hours at 150 ºC in a heating mantle.

The surface area was determined by the fundamental BET equation;

$$1/W*((P/P_0)-1) = 1/W_mC + C-1/ W_mC *(P/P_0) \tag{11}$$

Where W, is the weight of gas adsorbed at a relative pressure, P/P_0, and W_m is the weight of adsorbate constituting a monolayer of surface coverage. The term C, is the BET constant and is related to the energy of adsorption in the first adsorbed layer and consequently its value is an indication of the magnitude of the adsorbent/adsorbate interactions.

3.4.3   Scanning Electron Microscopy and Energy Dispersive X-ray Spectroscopy

FEI Nova Nano lab Scanning Electron Microscopy (SEM) played a crucial role in recoding the morphology of the particles. In general, SEM uses a beam of electrons to form an image. Electrons in the beam interact with atoms in the sample to produce various signals which are then used to gather information such

46

as surface topography, crystalline structure and chemical composition. Prior to analysis, the powder samples were sprinkled on a carbon tape and supported on a metallic disc stub. In addition, nano-powders were coated with 5μm thick layer of gold and palladium to reduce charging interference during imaging.

Elemental composition was obtained using the Oxford INCA EDS software on the SEM. Briefly, elemental analysis is achieved when the electron beam interacts with the sample and display x-rays with similar properties of the elements present in the sample. MoS_2 composition data was collected using area and point scan.

3.4.4 Transmission Electron Microscopy

In transmission electron microscopy (TEM), a beam of electrons transmitted through a sample interacts with the sample and forms an image. TEM engineered capabilities allow directed images of nano materials to be captured at a much higher resolution than light microscopy. Additional information includes particle size, distribution and morphology. All samples were sonicated using an ultrasonic bath for five minutes in acetone. Small amounts of the solution were sprayed on the copper grid and left to dry. Using tweezers, the sample is placed on a sample holder and inserted in the instrument.

3.4.5 Raman spectroscopy and Fourier Transform Infrared spectroscopy

Both Raman and Fourier Transform Infrared (FT-IR) spectroscopies have proven to be powerful non-destructive characterization tools for a detailed study of amorphous and crystalline compounds. Infrared spectra were collected using

47

Bruker Tensor 27 equipped with ZnSe crystal that absorbs strongly below 500 cm$^-$^{1}, so data was collected in the range 550-4000 cm^{-1}. Generally for a single beam measurement, a background spectrum is acquired prior to running an actual sample. Raman measurements were obtained using T64000 Horiba Jobin Yvon Raman spectroscopy. The technique is based on inelastic scattering of monochromatic light from a laser. The light in turn interacts with molecular vibrations of a given system that leads to the energy of the laser photons to be shifted either up or down. It is this particular shift in energy that produces information about vibrational modes of a system. FT-IR gave detailed information on bonding and coordination of the as-synthesized materials using the same basic principles as Raman analysis. On the other hand, Raman provided information on the vibration of S-Mo-S atoms and approximate layer thickness that is largely dependent on the E_{2g} and A_{1g} peak frequencies, intensities and widths.

3.5 Synthesis of Carbon nanospheres (CNS)

These were obtained using the established method by Dlamini et al.[4]: In brief, sucrose solution (0.3 M) was transferred into a 100ml Teflon-lined stainless steel autoclave and heated at 150 °C for 5 hours. The reaction was then left to cool at room temperature. At this stage, a black precipitate that had formed was purified by Soxhlet extraction, washed with ethanol and water then dried at 80 °C in an oven.

3.6 Synthesis of MoS$_2$/CNS composites

3.6.1 *Composite s-MoS$_2$/CNS*

The CNS-modified spherical **s-MoS$_2$** (abbreviated herein as **s-MoS$_2$/CNS**) composite was prepared as follows. Firstly, 0.028 g CNSs were ultrasonically dispersed in 20 mL deionized water. Then 0.30 g Na$_2$MoO$_4$•2H$_2$O was added and ultrasonic dispersed for 30 min. After adjusting the pH value to 6.5 with 12 M HCl, 0.80 g L-cysteine was added. The resultant mixture was diluted with water to 30 mL and rapidly stirred for about 1 h. The mixture was then transferred into a 40 mL Teflon cup and heated in a stainless steel autoclave at 180^{0}C for 36 h. Upon completion the product was cooled naturally to room temperature, the s-MoS$_2$/CNS composite was collected by filtration, washed with distilled water and acetone for several times, and finally dried in oven at 80 °C for 24 h.

3.6.2 *Composite f-MoS$_2$/CNS*

CNS-modified flower-like **f-MoS$_2$** composite (abbreviated herein as **f-MoS$_2$/CNS**) was prepared as follows. 1.21 g Na$_2$MoO$_4$•2H$_2$O was added to the sonicated CNS in 20 mL deionised water and further sonicated for 30 min. Then 1.56 g thiourea and 0.28 g PEG-1000' were added to the solution and the mixture diluted to 30 ml before heating at 180 °C using a Teflon-lined stainless steel autoclave for 36 h. Upon completion the product was cooled naturally to room temperature, the f-MoS$_2$/CNS composites was collected by filtration, washed with distilled water and acetone for several times, and finally dried in oven at 80°C for 24 h. To homogenise the as-synthesized materials and further promote

crystallization, the as-synthesized materials, were annealed in a horizontal furnace with a quartz tube at 900°C under a flow of nitrogen at a rate of 100ml/min for 4 h.

3.6.3 *Mechanical exfoliation of MoS$_2$ and CNS*

1.1 g of **g/h-MoS$_2$** from previous methods were mixed in a flask with 0.08 g CNS in de-ionised water and placed in an ultrasonic bath for an hour. The product was collected by centrifugation and dried in an oven overnight.

3.7 Characterization

The XRD patterns of the as-prepared MoS$_2$ and MoS$_2$/CNS nanopowders were obtained from DMax/2500PC diffractometer using Co Kα radiation (K=1.5418 Å) at 40kV, 100mA and a 2θ range of 10-90°. The FTIR spectra were recorded using a Bruker Tensor 27 FTIR spectrometer equipped with ZnSe crystal that absorbs strongly below 500 cm^{-1}. FTIR spectra were collected in the range 550-4000 cm^{-1} and a single beam measurement as a background spectrum was acquired prior to running the actual sample. Raman measurements were carried out in air using a Horiba Jobin Yvon spectrometer equipped with an Olympus BX40 microscope attachment to focus the laser beam on a small selected area of the sample, a 30 mW green argon laser (λ = 514 nm) an excitation source, and a 1800 lines per mm grating monochromator with liquid nitrogen-cooled CCD. The BET (Brunauer Emmett and Teller) measurements were performed to determine the specific surface area and pore size of the nano-sheets using Micromeritics TriStar II instrument. The SEM images were obtained using JEOL- JSM 7500F scanning

electron microscope operated at 2.0 kV and FEI Nova Nanolab 600 SEM. TEM images were obtained from FEI Tecnai T12 microscope operated at an acceleration voltage of 120 kV. Elemental composition was obtained using the Oxford INCA EDS software on the SEM.

3.8 Electrochemical measurements

3.8.1 Fabrication

3.8.1.1 Current collector surface treatment

As common practise, as-received nickel foams are pre-treated prior to use. For thermal activation, the nickel foam was heated between 200 and 300 °C in the presence of argon. In chemical activation, it was soaked in a 1M HCl solution and sonicated for 20 minutes before leaving it to dry in a vacuum oven. The aim is to remove residual impurities while creating surface roughness. Ultimately the surface area improves.

3.8.1.2 Electrode preparation

Nickel foam (Celmet: thickness = 1.6 mm, surface area 7500 m^2, cell size = 0.5 mm, 48-52 cells per inch) was used as substrate and current collector in the fabrication of the symmetric pseudocapacitors. Before use, the nickel foam was thoroughly cleaned by sonicating in 1 M HCl solution for 30 min, washing with copious amount of distilled water, and finally drying under vacuum. A 1 M Na$_2$SO$_4$ solution was used as the electrolyte while a porous filter paper (Whatman®) served as the separator. The electrode materials were prepared by first thoroughly mixing the active materials (either MoS$_2$/CNS or MoS$_2$), carbon

51

black as the conducting agent, and polyvinylidene fluoride (PVDF) as the binder (80:15:5 weight ratio) using pestle and mortar with few drops of anhydrous N-methyl-2-pyrrolidone (NMP) to produce a homogeneous paste. The resulting slurry was coated onto the nickel foam substrate with a spatula. The electrode was then dried at 60 °C overnight in a vacuum oven. The mass of the active material on nickel foam was between 5 and 20 mg. For complete impregnation, the assembled cells were left for 12 hours prior to testing.

3.8.1.3 Cell assembly

Symmetric pseudocapacitive properties of the materials were investigated using the Swagelok cells (MTI, Inc., USA) illustrated in Fig. 3.2. The prepared electrode with active material was placed inside the lower split of a stainless steel split test cell and few drops of an electrolyte solution (1M Na_2SO_4) added. Then a separator (filter paper) was placed on top of the first electrode followed by an O-ring. Few more drops of the electrolyte solution were added and the second electrode positioned above. Two spacers were added to keep the stack horizontal and finally, tightly sealed the upper slit with the bottom, using bolts and the cap above. For complete impregnation, the assembled cells were left for 12 hours prior to testing.
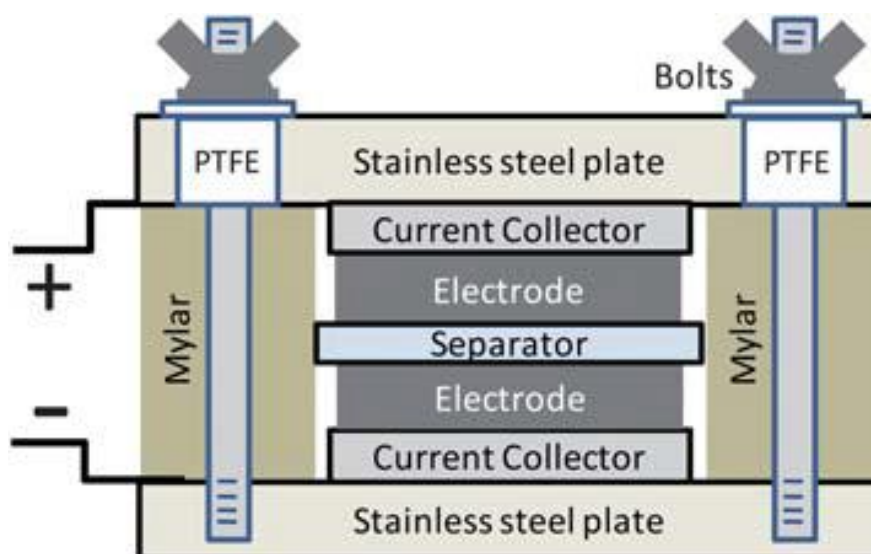
Figure 3.2. Schematic of a test cell assembly.[5]

3.8.2 Testing

All electrochemical measurements: cyclic voltammetry (CV), galvanostatic cycling with potential limitation (GCPL), and electrochemical impedance spectroscopy (EIS) were performed at room temperature using computer-controlled Multi-channel Potentiostat/Galvanostat Bio-Logic VMP3 work station driven by EC-Lab® v10.40 software with Z-fit tool for EIS data analysis. EIS measurements were carried out in the frequency range from 10 kHz to 10 mHz at the open circuit voltage with AC voltage amplitude of 1.5 mV.

The specific capacitance (C_{sp}), maximum specific power density (P_{max}) and specific energy density (E_{sp}) was evaluated using the conventional equations (12-16).[6, 7]

$$C(F) = \frac{i\Delta t}{\Delta V}$$ (12)

$$C_{sp}(F\ g^{-1}) = \frac{4C}{m}$$ (13)

$$P_{max}(10^3 W\ kg^{-1}) = \frac{V^2}{4\ m\ R_{ir}}$$ (14)

where, $R_{ir}(\Omega) = \frac{\Delta V_{ir}}{2I}$ (15)

$$E(\frac{1}{3.6} Wh\ kg^{-2}) = \frac{CV^2}{2m}$$ (16)

where i (A) is the applied current, ΔV (V)/Δt (s) the slope of the discharge curve and m (g) the total mass of the two electrodes, C (F) the calculated capacitance, V (V) is the maximum voltage obtained during charge, and R_{ir} is the internal resistance which is determined from the voltage drop at the beginning of each discharge, while the ΔV_{ir} represents the voltage drop.

3.8.2.1 Cyclic Voltammograms

In this work, cyclic voltammetry (CV) measurements were done to investigate the electrochemical processes and determine the capacitance capabilities of MoS_2–based supercapacitors. In principle, when a voltage is applied linearly (from upper limit to lower limit and vice versa) as a function of time, a current is produced.[8] The voltage is given by the Nernst equation, and the rate of change of potential is referred to as scan rate (Vs^{-1}).[9] To investigate the effect of scan rate on the capacitance of the electrode, CV curves were measured at various scan rates namely, 10, 20, 30, 50 and 100mVs^{-1}. Usually the specific capacitance decreases

with increasing scan rate. This is explained by the fact that at low scan rates ions of the electrolyte have more time to diffuse and penetrate into the electrode pores for double layer charge storage formation. This contributes significantly to the total capacitance.[10]

The results obtained from this technique are usually presented as series of plots of I vs V and capacitance calculated using equation (12). Alternatively, the graph is integrated to find the area under the curve and capacitance calculated using equation (17) below. Where Q, is the area, m is the mass of the active material and V, voltage.

$$C_{sp} = \frac{Q}{2mV} \tag{17}$$

As the scan rate increase, the energy density decreases and power density increases.

In theory, CV curves for supercapacitors are rectangular in shape. However, practically they take a shape of a parallelogram with bulging peaks as depicted in Fig. 3.3. Frackowiak and Beguin[11] suggested that, these peaks are associated with faradic reactions of pseudocapacitors and the porous nature of the electrode surface. Another important piece of information CV can provide is the reversibility of the reaction on the surface of an electrode. In the case where it is reversible, the voltammogram displays a mirror-image. On the other hand, irreversible reactions will have different charge-discharge profiles.[11]
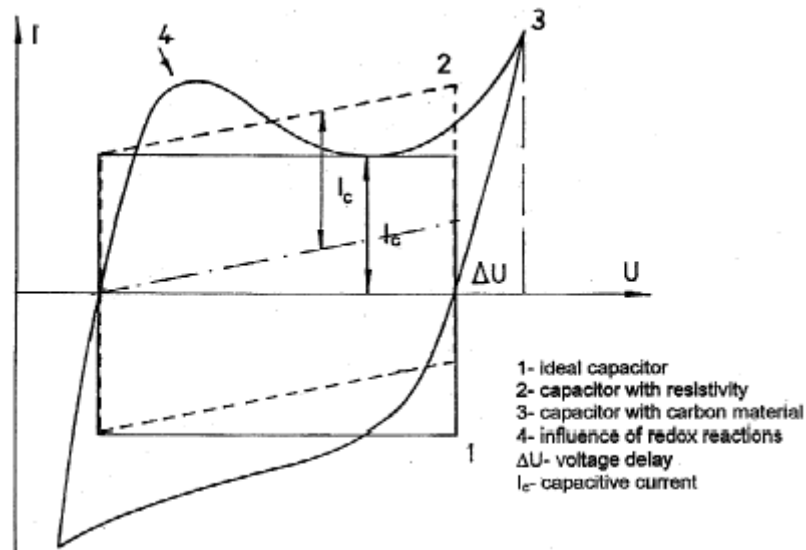
Figure 3.3. Cyclic voltammograms for supercapacitors.[11]

3.8.2.2 Galvanostatic charge/discharge

The real power of this technique lies in the ability to estimate the relationship between power and energy densities in a device. Charge and discharge experiments were carried out at various current densities over a potential window defined by CV curves. The specific capacitance of the electrodes was calculated at different current densities according to equation (12).

The IR drop located at the beginning of the discharge profile indicates the energy loss as a result of internal resistance. This resistance, often called equivalent series resistance, is associated with hindrance of ion diffusion in the electrodes. Electrochemists look at this information to gain insight on internal chemistry. It is determined using equation (15).

This effect is accounted for in power density as shown by equation (14). The results of charge-discharge cycles are usually presented in a graph of V vs T and as Ragone plots. A typical example of V vs T graph is shown in Fig. 3.4.
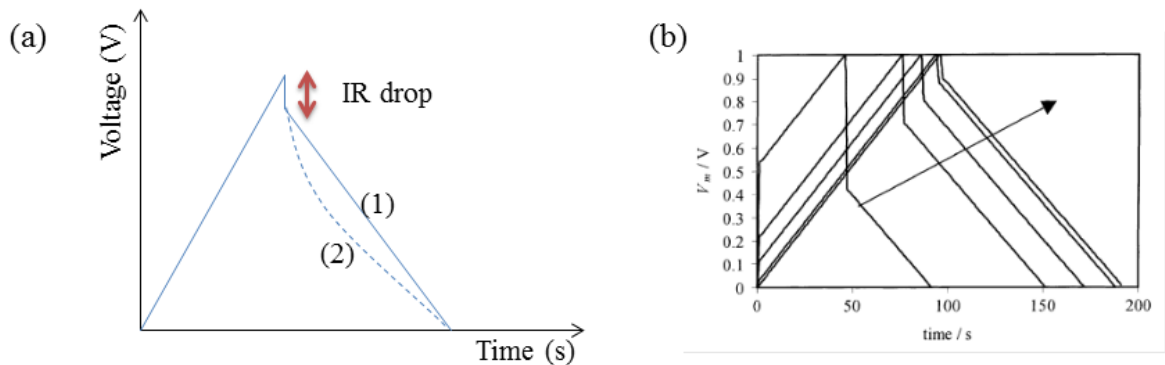
Figure 3.4. Galvanostatic charge-discharge curves of (a) 1. EDLC and 2. pseudocapacitor (b) charge-discharge tests at various current densities showing different internal resistance behaviour.

3.8.2.3 Electrochemical impedance spectroscopy

Electrical impedance spectroscopy (EIS) was used to investigate the behavior of the electrode in the frequency realm. Impendence was measured at OCV over the frequency range 5 MHz and 100 kHz before and after cycling. Experimental results are graphed on a Nyquist diagram, where the vertical axis is the imaginary impedance and horizontal axis the real axis. The Nyquist diagram is divided into 3 segments namely, the high, medium and low frequency parts. Each frequency is dominated by diffusion phenomena that translate to the impedance behavior. At

high frequency, the real axis indicates equivalent series resistance (ESR), which includes resistance of terminals, electrolyte, separator and current collectors. In Fig. 3.5 it is referred to as bulk resistance. The second part is medium frequency impedance that shows a semi-circle, reflecting charge-transfer resistance on the electrode-electrolyte interface. The slope of the 45 ° portion of the curve at higher frequency is called the Warburg resistance. As the frequency increases, ion diffusion transport in the electrolyte are reduced, thus the resistance and capacitance decrease.[12] Eventually, the Nyquist plot alone can be quite vague in explaining the concept of frequency dependence. In this regard, a Bode diagram, showing AC frequency of selected data point is also presented.
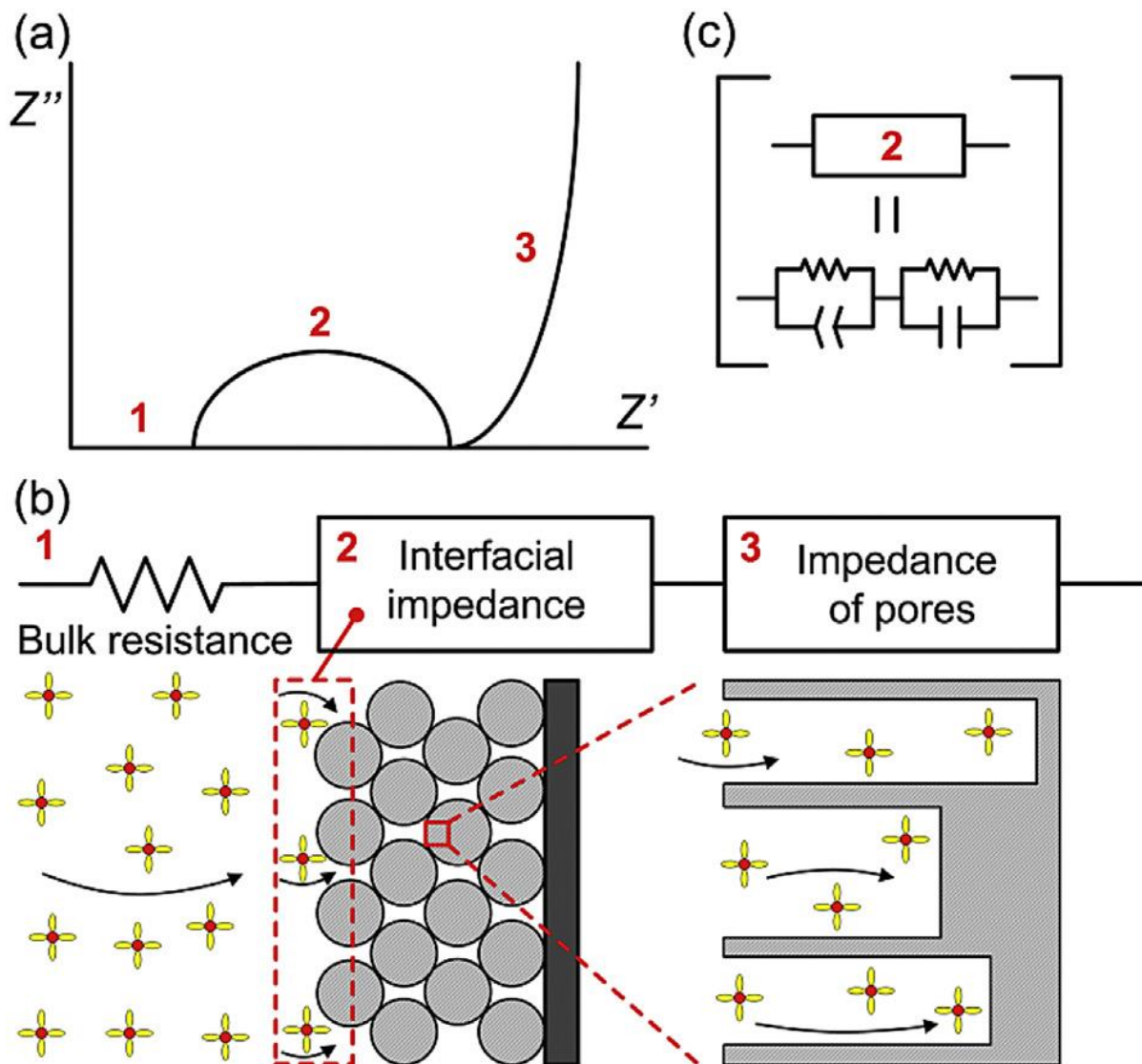
Figure 3.5. Schematic representation of the Nyquist impedance plot of an ideal capacitor (vertical thin line) and an electrochemical capacitor with porous electrodes (thick line).[13]

3.8.2.4 Voltage holding

Apart from the capacitance, life expectancy coupled with recyclability is a very important feature in supercapacitors. During voltage holding measurements

charge-discharge is done at fixed current densities over a potential window similar to that achieved in cyclic voltammetry. A current density that results in discharge slope of about 5 seconds was purposely chosen since it is more likely to give a high power density. Charging and discharging sequence was done after every 10 hour cycle up until the last cycle at 50 hours, where it was set to stop. From each cycle, capacitance, as well as energy and power densities were evaluated over time and plotted.

Columbic efficiency (η) was also determined using the discharge profile during cycling of the electrodes.

$$\eta = \frac{t_d}{t_c} \times 100 \tag{18}$$

Where t_d is the discharging time and t_c is the charging time.[14]

3.9 References

1. Huang, K. J.; Wang, L.; Zhang, J. Z.; Wang, L. L.; Mo, Y. P. (2014) One-Step Preparation of Layered Molybdenum Disulfide/multi-Walled Carbon Nanotube Composites for Enhanced Performance Supercapacitor. *Energy*, *67*, 234–240.

2. Wang, S.; Li, G.; Du, G.; Jiang, X.; Feng, C.; Guo, Z.; Kim, S. J. (2010) Hydrothermal Synthesis of Molybdenum Disulfide for Lithium Ion Battery Applications. *Chinese Journal of Chemical Engineering*, *18*, 910–913.

3. Ramakrishna Matte, H. S. S.; Gomathi, a.; Manna, A. K.; Late, D. J.; Datta, R.; Pati, S. K.; Rao, C. N. R. (2010) MoS_2 and WS_2 Analogues of Graphene. *Angewandte Chemie - International Edition*, *49*, 4059–4062.

4. Billing, D. G.; Dlamini, M. W.; Kumi, D. O.; Phaahlamohlaka, T. N. (2015) Carbon Spheres Prepared by Hydrothermal Synthesis — A Support for Bimetallic Iron Cobalt Fischer – Tropsch Catalysts Carbon Spheres Prepared by Hydrothermal Synthesis — A Support for Bimetallic Iron Cobalt Fischer – Tropsch Catalysts. *ChemCatChem, 7,* 3000 – 3011 .

5. Stoller, M. D.; Ruoff, R. S. (2010) Review of Best Practice Methods for Determining an Electrode Material's Performance for Ultracapacitors. *Energy Environ. Sci.,3,* 1294–1301.

6. Béguin, F.; Presser, V.; Balducci, A.; Frackowiak, E. (2014) Carbons and Electrolytes for Advanced Supercapacitors. *Advanced Materials*, *26*, 2219–2251.

7. Presser, V.; Ozoemena, K. I. (2015) PAPER A High-Rate Aqueous Symmetric Pseudocapacitor Birnessite-Type Manganese Oxide Nanohybrids. *Journal of Materials Chemistry A: Materials for energy and sustainability*, *3*, 3480–3490.

8. Suroveic, A.H. (2013) Introduction to Electrochemistry. *Journal of Laboratory Chemical Education, (3),* 45–48.

9. Kumar, R. V.; Sarakonsri, T. (2010) Introduction to Electrochemical Cells. *High Energy Density Lithium Batteries: Materials, Engineering, Applications*, 1–25.

10. Shu, D.; Lv, C.; Cheng, F.; He, C.; Yang, K.; Nan, J.; Long, L. (2013) Enhanced Capacitance and Rate Capability of Nanocrystalline VN as Electrode Materials for Supercapacitors. *International Journal of Electrochemical Science*, *8*, 1209–1225.

11. Frackowiak, E.; Béguin, F. (2001) Carbon Materials for the Electrochemical Storage of Energy in Capacitors. *Carbon*, *39*, 937–950.

12. Ko, R.; Carlen, M. (2000) Principles and Applications of Electrochemical Capacitors, *Electrochimica Acta, 45*, 2483–2498.

13. Yoo, H. D.; Jang, J. H.; Ryu, J. H.; Park, Y.; Oh, S. M. (2014) Impedance Analysis of Porous Carbon Electrodes to Predict Rate Capability of Electric Double-Layer Capacitors. *Journal of Power Sources*, *267*, 411–420.

14. Agarl, E.; Benjamin, A.; Dennison, C.; Kimburl, E.C.; (2013) On the determination of coulombic effeciency for Vanadium redox flow batteries:

Cutoof voltage vs. state of charge limits. *The Electrochemical Society*, Abstract#1663.

CHAPTER FOUR

4 SYMMETRIC PSEUDOCAPACITORS BASED ON MOLYBDENUM DISULFIDE (MOS₂)-MODIFIED CARBON NANOSPHERES: CORRELATING PHYSICO-CHEMISTRY AND SYNERGISTIC INTERACTION ON ENERGY STORAGE[*]

4.1 Introduction

Pseudocapacitors are redox-based electrochemical capacitors (ECs). Unlike their counterpart, the electrical double layer capacitors (EDLC) that only use carbon materials as electrode materials, pseudocapacitors employ redox-active materials such as conducting polymers, metal oxides and metal sulphides.[1-4] Unlike batteries with high energy densities, ECs are characterized by their high power characteristics which make them very attractive for several technologies and devices that require high-power applications (*i.e.*, ability to release energy pulses in a very short time, in a few seconds) such as in regenerative braking energy systems in vehicles and metro-rails, "stop-start" applications in modern cars, uninterrupted power supply (UPS), emergency doors in aircrafts, escalators in buildings, to name a few.[5,6]

One of the emerging high-power supercapacitor electrode materials is the molybdenum disulfide (MoS_2), a member of the transition-metal dichalcogenides (TMDs). MoS_2 has found applications in electrochemical devices, hydrogen storage, catalysis, capacitors, solid lubricants, and intercalation hosts.[7, 8] The MoS_2 is a layered-structured material with close relationship to graphene, characterized by a sheet-like morphology. The Mo layer is sandwiched between two S layers, and the triple layers are stacked and held together by weak van der Waals interactions.[2, 9-11] Due to it higher intrinsic fast ionic conductivity (than oxides) and higher theoretical capacity (than graphite), MoS_2 continues to attract a lot of attention, particularly in supercapacitors. [2, 7, 12] Subsequently, Soon and Loh[13] pointed out the use of MoS_2 as an electrode material for supercapacitors. The results suggest that the supercapacitor performance of MoS_2 is comparable to that of carbon nanotubes (CNT) array electrodes. In addition to double-layer capacitance, diffusion of the ions into the MoS_2 at slow scan rates gives rise to faradaic capacitance. Analogous to Ru in RuO_2, Mo central atom displays a range of oxidation states from +2 to +6. This plays an important role in enhancing charge storage capabilities.[14] However, the electronic conductivity of MoS_2 is still lower compared to graphite, and the specific capacitance of MoS_2 is still very limited when used alone for energy storage applications.[12, 13, 15] As evident in several literature, there is need to improve the capacitance of MoS_2 with conductive materials such as CNT,[12] polyaniline (PANI),[2] polypyrrole (PPy),[9] and reduced graphene (RGO).[11] In a review by Nieto-Marquez et al.,[16] carbon nanospheres (CNS) has been described as a good candidate for catalytic and adsorption applications, and whose unclosed graphitic flakes provide the

65

necessary 'dangling bonds' that could enhance surface reactions. CNS has also been used to enhance the conductivity of battery cathode material, LiFePO$_4$.[17]

To the best of our knowledge, the supercapacitive properties of MoS$_2$ have only been investigated in half-cells (*i.e.*, 3-electrode systems), which creates a huge knowledge gap on the true behavior of the electrode material when used in full-cells (2-electrode systems). Moreover, there is no literature on the effect of CNS on the supercapacitance of MoS$_2$. Pseudocapacitors usually suffer from poor electrical conductivity and irreversible redox-activity, thereby leading to gradual loss of capacitance. To tackle the abovementioned challenges, this study adopted two different synthesis protocols to prepare MoS$_2$ and MoS$_2$/CNS composites with different physico-chemistries (*i.e.*, spherical and flower-like morphologies, structure, porous textures and electrochemistry) and then used it to fabricate symmetric pseudocapacitors. We clearly show that the pseudocapacitive properties of the MoS$_2$/CNS (especially, in terms of cycling stability and electronic conductivity) are intrinsically linked with the presence of CNS.

4.2 Results and discussion

4.2.1   Material characterisation

A one-pot hydrothermal route was used for the synthesis of MoS$_2$, CNS and MoS$_2$/CNS. Fig. 4.1 shows the SEM and TEM images of the CNS (Fig. 4.1c and d), confirming the spherical nature of the CNS in agreement with literature. The micrographs show the interconnected uniform amorphous CNS in the particle size diameter range of 100-200 nm. Fig. 4.1 compares the SEM and TEM images of the s-MoS$_2$ and s-MoS$_2$/CNS. The SEM and TEM micrographs of the s-MoS$_2$

(Fig. 4.1a and b) show the formation of sphere-like morphology consisting of several and agglomerated clusters of s-MoS$_2$ sheets.
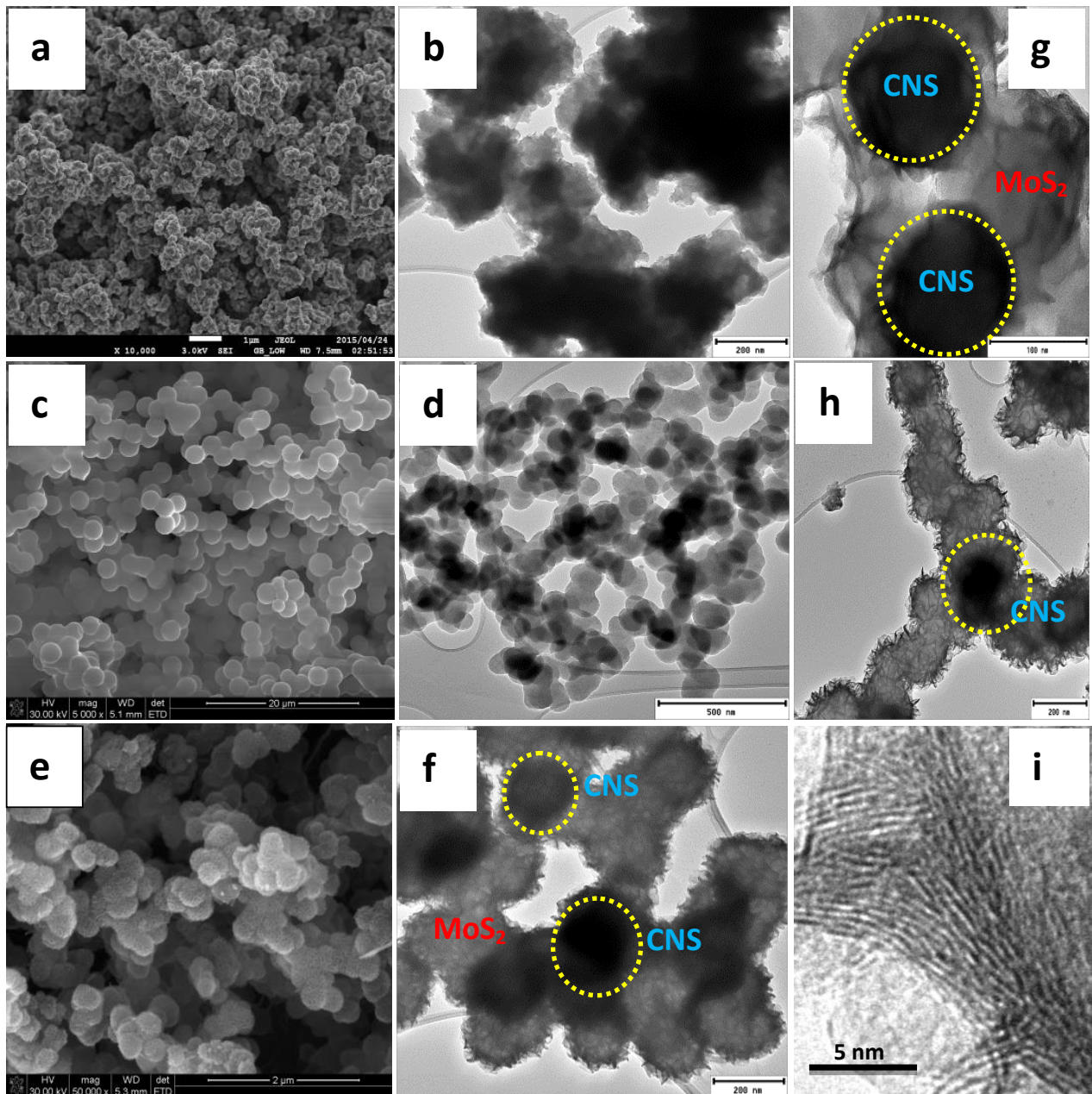
Figure 4.1. SEM (a,c and e) and TEM (b,d,f,h and i) micrographs of s-MoS$_2$ (a and b), CNS (c and d), s-MoS$_2$/CNS (e and f), magnified views of s-MoS$_2$/CNS (g and h), and d-spacing of s-MoS$_2$ (i).

Element	Weight%	Atomic%
Na K	1.5	3.35
S K	41.34	66.11
Mo L	57.16	30.55
Totals	100	
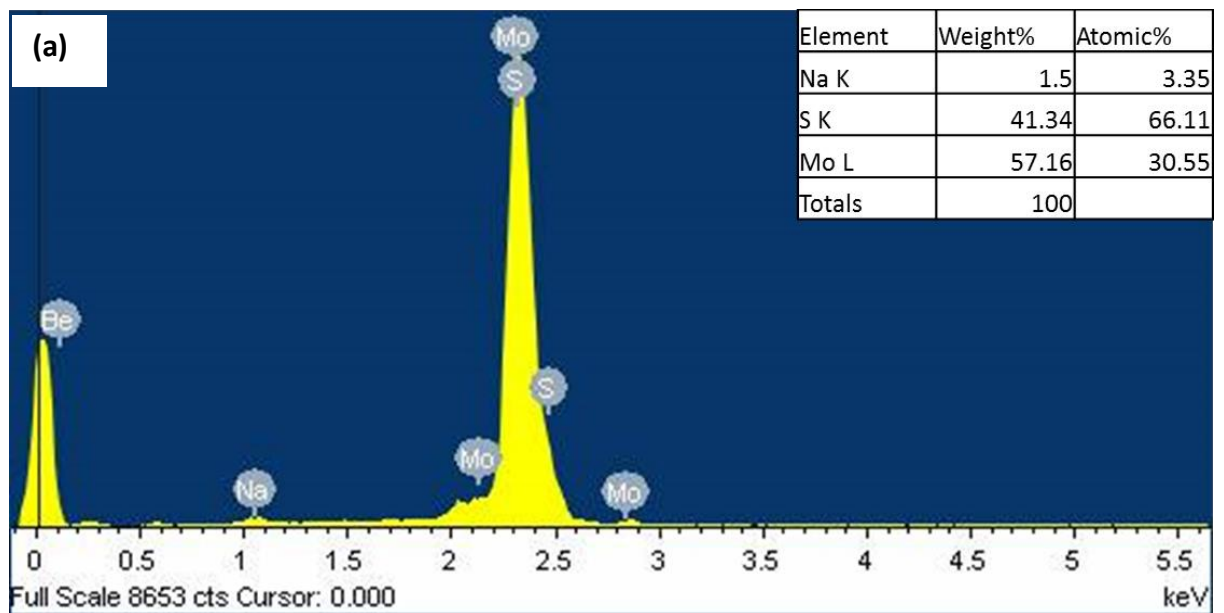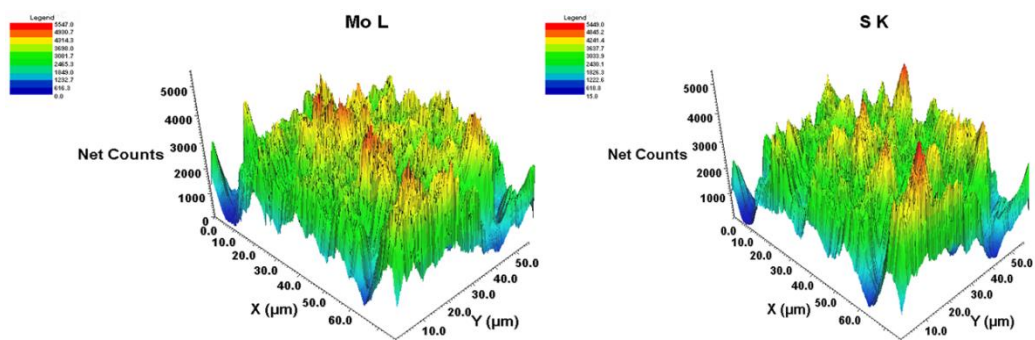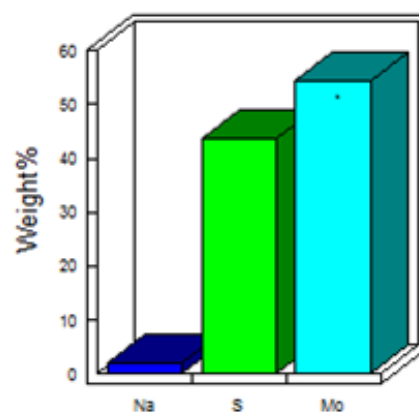
Figure 4.2. EDX results for s-MoS$_2$ showing spectra and elemental composition (a), 3-D topographical profile of Mo and S net counts and (c) bar chart of major elements.

A closer examination of the TEM images of the CNS (Fig. 4.1d) and s-MoS$_2$/CNS (Fig. 4.1f-h) clearly suggest an uniform dispersion and excellent integration of the MoS$_2$ with the CNS. The value of d-spacing of the s-MoS$_2$ shown in the TEM image (Fig. 4.1i) is 0.62 nm, which is in agreement with literature.[18] In this synthesis method, it seems that the CNS particles acted as substrates for nucleation, where MoO$_4^-$ ions reacted with sulphur ions from L-cysteine to form the MoS$_2$ sheets on the CNS. The presence of CNS prevented MoS$_2$ stacking, thus, the formation of a porous 3-D sphere-like architecture with highly dispersed wrinkled and fluffy MoS$_2$ sheets on CNS particles. This unique structure is also apparent in the TEM images (Fig. 4.1 f and h). In the s-MoS$_2$/CNS composite, the MoS$_2$ nano-sheets' edges are readily exposed and not entangled as in MoS$_2$. This loose structure is desirable for superior charge storage. However, the MoS$_2$ sheets in the composite are not visible as layered, instead, they grew in various orientations and intertwined around the spheres. Important consequence is small accessible surface area coupled with the small micropores. This could potentially cause an obstruction for ion transportation and thus limit the capacitance. The elemental composition of as-synthesized s-MoS$_2$, obtained from the EDS (Fig. 4.2) gave Na (3.35), S (66.11) and Mo (30.55) by weight percentage, clearly confirming the stoichiometry of the MoS$_2$. The impurity 'Na' is attributed to the starting precursor Na$_2$MoO$_4$•2H$_2$O.

Similarly, the flower-like nanostructures (f-MoS$_2$) were obtained using a one-pot hydrothermal method. This method relies on sodium molybdate and thiourea to provide MoO$_4^{2-}$ ions and sulphur atoms, respectively. Interestingly, the addition of small amounts of PEG in our synthesis protocol assisted in the

efficient dispersion of the MoS_2 to generate the flower-like morphology. The starting precursor materials in the MoS_2 formation play a vital role especially in the achieved morphology. A slight change even in the reducing agent can bring about enormous value. In this hydrothermal process, the reaction involves three steps: (a) The hydrolysis of sulfur precursor to form H_2S, followed by (b) the reduction of Mo and (c) finally the formation of MoS_2.[19]

$$CS\ (NH_2)_2 + 2H_2O \longrightarrow 2NH_3 + CO_2 + H_2S \qquad (19)$$

$$4Na_2MoO_4 + 15CS\ (NH_2)_2 + 6H_2O \longrightarrow 4MoS_2 + Na_2SO_4 + 6NaSCN + 24NH_2 + 9CO \qquad (20)$$

The SEM and TEM images of as-synthesized MoS_2 in Figure 2 clearly show flower-like hierarchical 3-D structures. The f-MoS_2 sheets self-assemble into a highly porous structure (Fig. 4.3a-c and e). The composite structure (Fig. 4.3d) also exhibit clear flower-like morphology. The occurrence of this morphology may be associated with the presence of a surfactant (PEG-1000'). Remarkably, after coating CNS with MoS_2 sheets, the surface appears rough and wrinkled by MoS_2 sheets (Fig. 4.3d, f, g). The value of d-spacing of the f-MoS_2 (Fig. 4.3h) is 0.61 nm, which is in agreement with literature.[20] The EDX data (see Fig4.4) depicted strong Mo and S overlapping signals, the MoS_2 contains Na 1.3 atomic %, S 62.09 atomic % and Mo 36.61 atomic %, confirming the stoichiometry of the MoS_2.
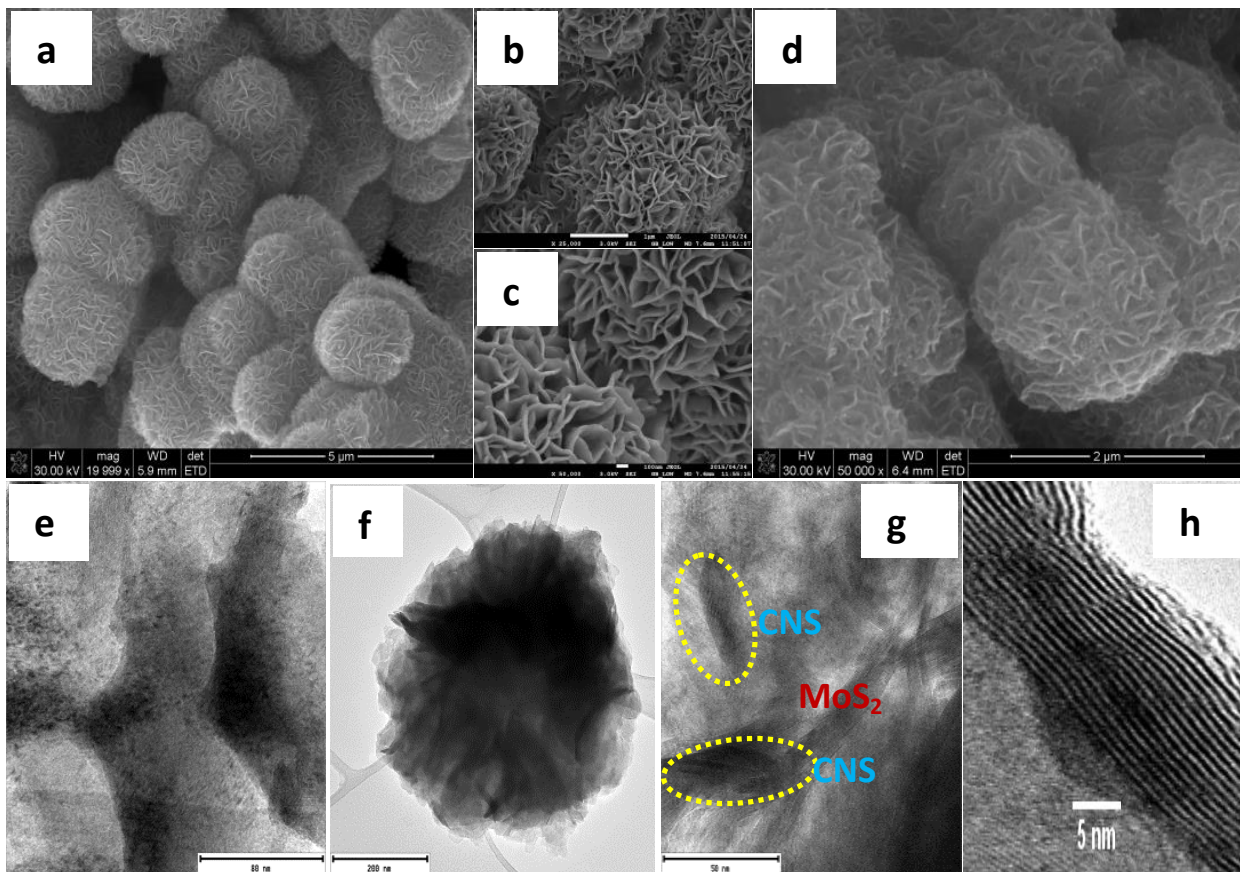
Figure 4.3. SEM (a-d) and TEM (e-h) micrographs of f-MoS$_2$ (a-c), f-MoS$_2$/CNS (d), f-MoS$_2$ (e), magnified views of f-MoS$_2$/CNS (f and g), and d-spacing of f-MoS$_2$ (h)

Element	Weight%	Atomic%
S K	37.59	64.31
Mo L	62.41	35.69
Totals	100	
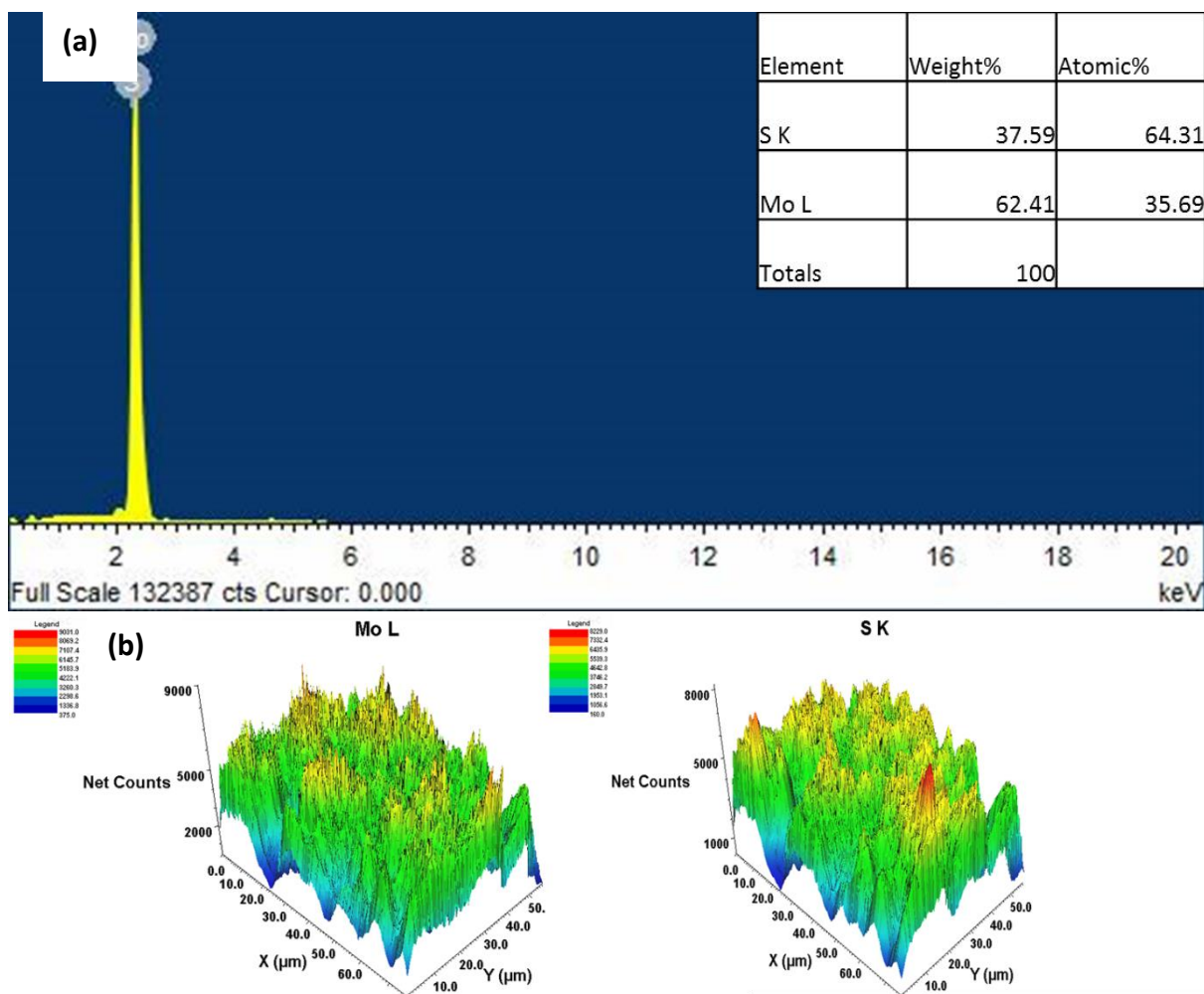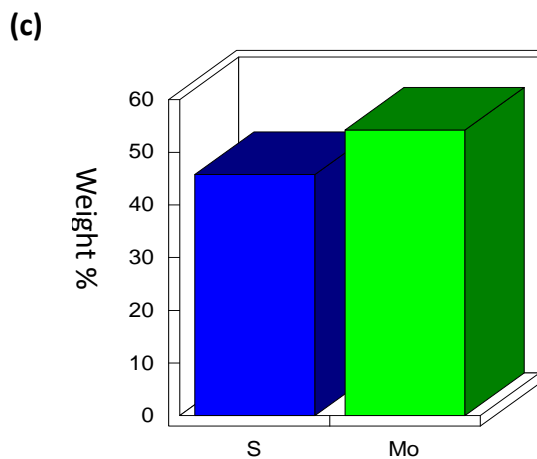
Figure 4.4. EDX results for f-MoS$_2$ showing spectra and elemental composition (a), 3-D topographical profile of Mo and S net counts and (c) bar chart of major elements.

MoS$_2$ is a hexagonal crystal system and layer-structured, D$^4_{6h}$ crystal system and P63 space group. Figure 4.5 compares the XRD patterns of the CNS and its MoS$_2$ spherical and flower-like composites. There is no significant difference between the MoS$_2$ and MoS$_2$/CNS patterns, confirming good integration of the CNS with the MoS$_2$ structure. The diffraction peaks at 2θ = 15.8°, 37.9° and 41.5° are indexed to the hexagonal phase of MoS$_2$ (002), (100) and (201), respectively. For the spherical morphology (s-MoS$_2$/CNS composite), the diffraction peaks are similar to the individual s-MoS$_2$, meaning that CNS fully interacts with the MoS$_2$ and its presence did not interfere with the structure of the MoS$_2$. For the spherical material, s-MoS$_2$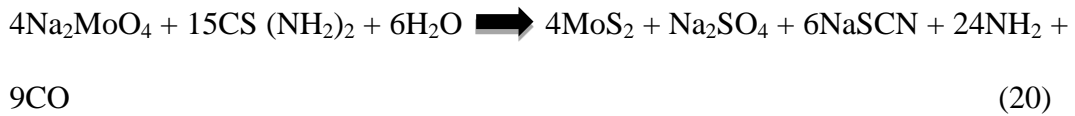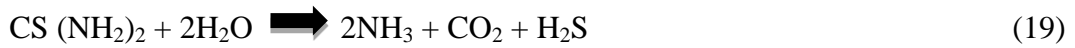/CNS, incorporation of CNS into the MoS$_2$ nanosheets decreases the intensity of the peaks, in particular the (002). The result indicates the formation of few layers of the MoS$_2$ in the composite, thus, CNS impedes the growth of the MoS$_2$ layer in a hexagonal array. Importantly, upon incorporation of the CNS, there is a slight shift in the diffraction lines of the MoS$_2$ to higher 2θ values (see Fig. 4.5a-c), which is an indication of a lattice contraction. However, for the flower-like morphology (f-MoS$_2$/CNS), the incorporation of the CNS resulted to a slight shift to lower 2θ values (see Fig. 4.5d-f), an indication of lattice expansion in the S-Mo-S interlayer spacing and formation of a few layers MoS$_2$. Ultimately, this improves the pathway and creates permeable channels for both ionic and electronic transportation. In addition, unlike the layered composite (Fig. 4.5a-f), the presence of the CNS did not negatively impact on the peak intensity of (002). In fact, the (002) peak becomes more intense and sharper, indicating a higher degree of crystallinity comparable to that of the bulk MoS$_2$. This finding may be due to strong

73

integration between the MoS_2 and CNS arising from the synthesis protocol adopted in this study, which allowed for the two materials to undergo chemical reaction rather than just physical mixing. Furthermore, the peak (103) is more apparent with a new broad peak (006) of hexagonal MoS_2 at 46 ° (Fig. 4.5d).
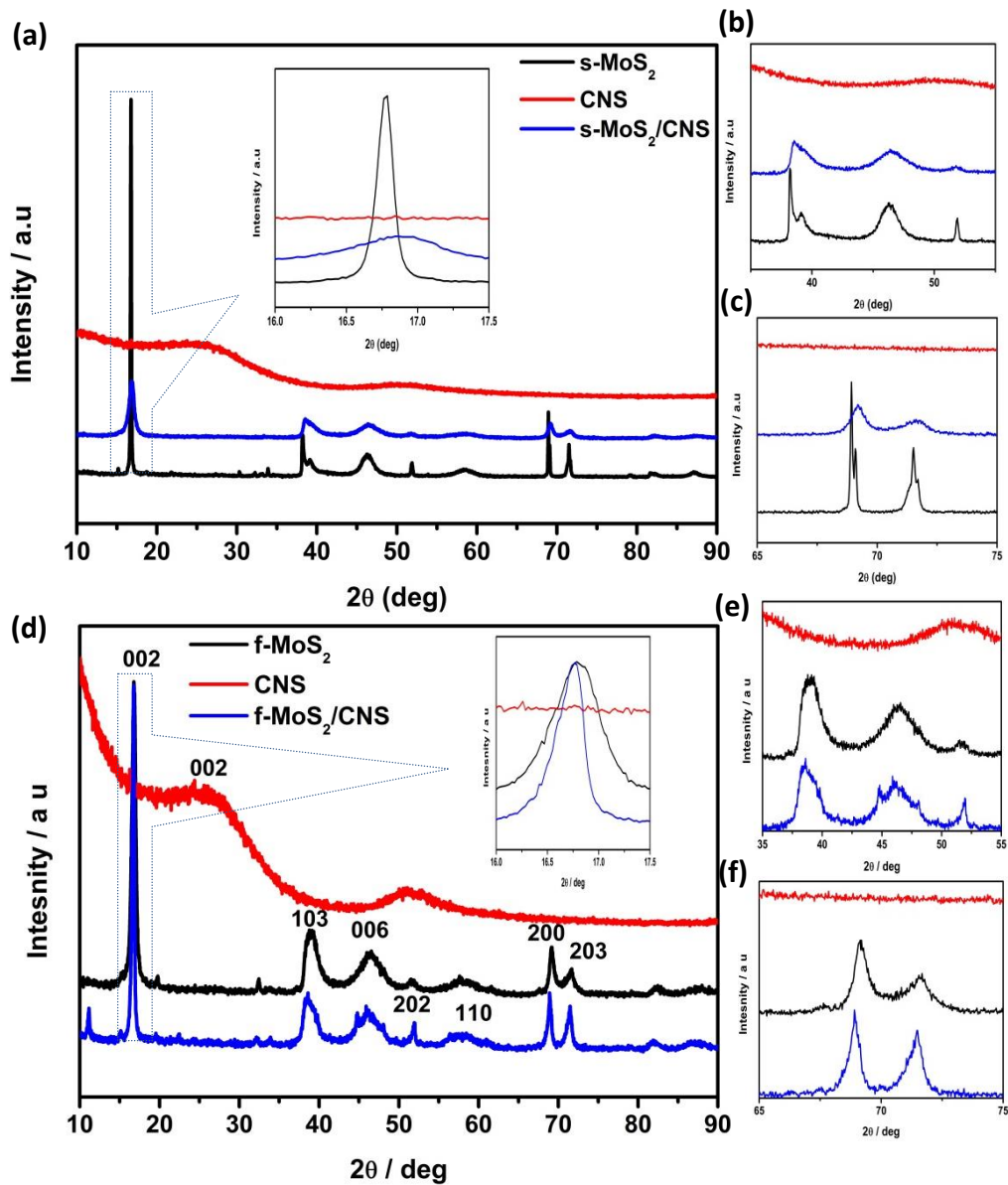
Figure 4.5. XRD patterns of MoS_2, CNS and MoS_2/CNS composites for spherical (a-c) and flower-like (d-f) products and their magnified views.

BET (five-point analysis) was used to measure the specific surface area and porosity of the as-synthesized materials. As shown in Table 4.1, the s-MoS$_2$ has a specific surface area of 17.8 m^2 g^{-1}; on the other hand, specific surface area of the s-MoS$_2$/CNS decreased to 9.17 m^2 g^{-1}. This dramatic reduction is explained by the hindrance to the growth of the MoS$_2$ due to the presence of the CNS (also confirmed by the XRD patterns). In fact, the CNS makes the surface area of MoS$_2$ inaccessible. Moreover, the pore size of MoS$_2$ and MoS$_2$/CNS were revealed to be 22.9 and 18.61 nm, respectively. The f-MoS$_2$/CNS composite gave a higher surface area with value of 61 m^2 g^{-1} compared with 25 m^2 g^{-1} recorded for the flower-like MoS$_2$. This means that incorporation of CNS prevented the agglomeration of MoS$_2$ sheets (also suggested from the XRD data). Surprisingly, the BET data follow the XRD data, especially the (002) peak height. Considering that capacitance is a function of the surface area, one should expect the materials with higher surface area (such as the f-MoS$_2$/CNS) to provide the best capacitance value. Moreover, despite that pores do not directly contribute to the surface area, they provide accessible pathways for easy diffusion of ions and reversible charge storage.

Table 4.1: Porous texture of the as-synthesized materials

Sample	SA$_{BET}$ (m^2 g^{-1})	Pore Volume (cm^3 g^{-1})	Pore Size (nm)
s-MoS$_2$	17.80	0.100	22.93
s-MoS$_2$/CNS	9.17	0.040	18.61
f-MoS$_2$	25.00	0.018	36.13
f-MoS$_2$/CNS	61.00	0.020	14.68

Raman spectroscopy was used to provide more insights into the structure and topology of the as-synthesized MoS_2-based nanocomposites. Fig. 4.6 shows the Raman spectra of as-synthesized MoS_2 nanosheets, CNS and MoS_2/CNS nanocomposites. The CNS exhibited the signature D and G peaks of carbon-based materials at 1347 and 1590 cm^{-1}, respectively. As we expected, the MoS_2/CNS composites also showed the D and G peaks close to the regions where they were observed for the CNS alone, confirming the successful integration of the CNS in the two MoS_2-based composites. There was no detectable difference in the intensity ratios of the D to G band (I_D:I_G) of the CNS (0.95), s-MoS_2/CNS (0.94) and f-MoS_2/CNS (0.94), which implies that the CNS essentially retained its pristine structure even after integration with the MoS_2. The characteristic Raman bands for bulk s-MoS_2 are observed at 375.69 and 402.49 cm^{-1} due to E^1_{2g} and A_{1g} modes with full-widths at half maximum (FWHM) of 8.47 and 8.23 cm^{-1}, respectively. The E^1_{2g} mode describes the in-layer displacement of the Mo and S atoms, whereas the A_{1g} mode relates to the out-of-layer symmetric displacements of S atoms along the c axis.[21, 22] Interestingly, the incorporation of the CNS into the MoS_2 resulted in the slight softening of these two Raman bands compared to those of the bulk MoS_2: the spherical MoS_2/CNS appeared at 375.07 cm^{-1} (E^1_{2g}) and 400.84 cm^{-1} (A_{1g}) while the flower-like morphology appeared at 374.91 cm^{-1} (E^1_{2g}) and 401.78 cm^{-1} (A_{1g}). Also, the increment in the FWHM values are more pronounced for the flower-like morphology than for the layered morphology.
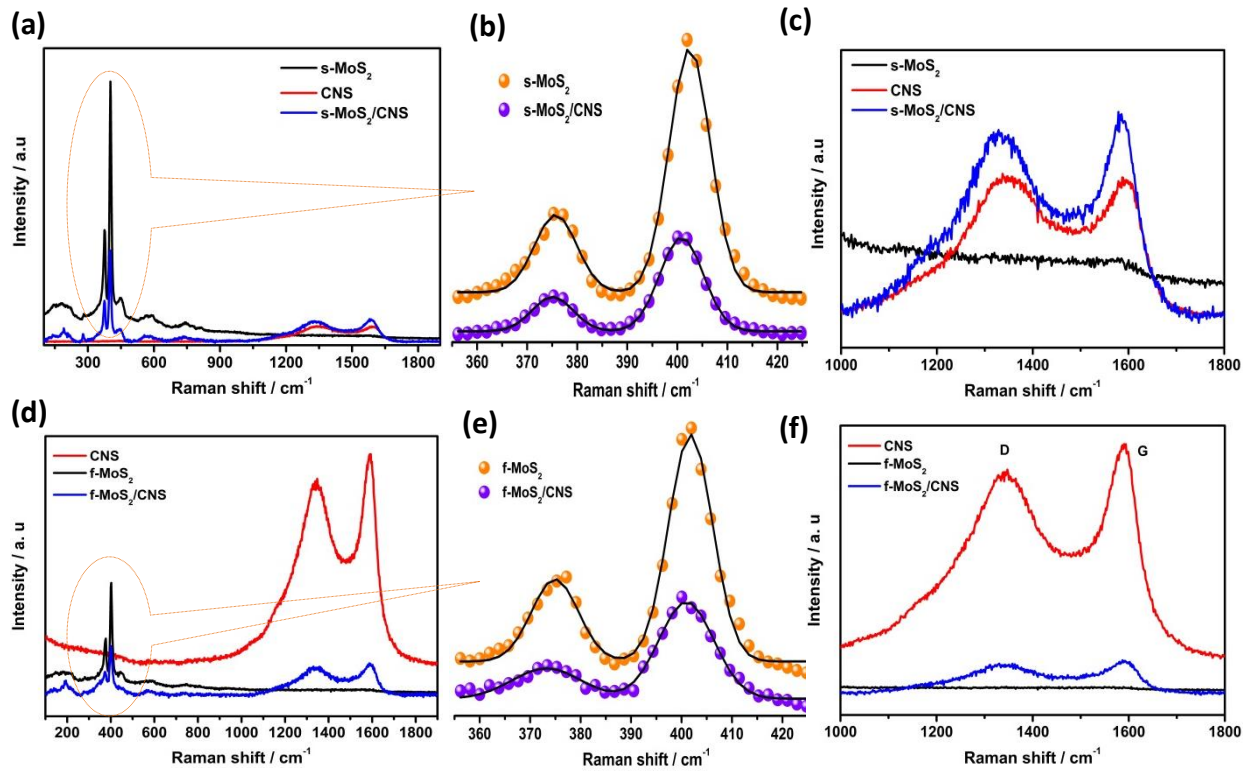
Figure 4.6. Raman Spectra of spherical (a-c) and flower-like (d-f) MoS_2, CNS and MoS_2/CNS nanocomposites and their magnified views.

Table 4.2 Comparison of Raman spectral data

Raman shift / cm^{-1}								
	s-MoS$_2$		s- MoS$_2$/CNS		f-MoS$_2$		f-MoS$_2$/CNS	
	E$^1_{2g}$	A$_{1g}$	E$^1_{2g}$	A$_{1g}$	E$^1_{2g}$	A$_{1g}$	E$^1_{2g}$	A$_{1g}$
Peak position	375.69	402.49	375.07	400.84	374.91	401.78	375.23	400.95
|E$^1_{2g}$ − A$_{1g}$|	26.8		25.77		26.87		25.72	
FWHM	8.47	8.23	8.19	8.71	9.29	8.72	13.55	10.88

77

In the flower-like morphology, FWHM values are larger in the f-MoS$_2$/CNS than in the bulk f-MoS$_2$ (*cf* E$^1_{2g}$ = 13.55 vs 9.29 cm^{-1} of the bulk f-MoS$_2$ or A$_{1g}$ = 10.88 vs 8.72 cm^{-1} of the bulk f-MoS$_2$). The broadening of the Raman bands is related to phonon confinement, and also indicates that the lateral dimensions of these MoS$_2$ layers are in the nano-dimension.[23] The larger FWHM for the f-MoS$_2$/CNS compared to its s-MoS$_2$/CNS counterpart is indicative of the smaller particle sizes and larger surface area, which corroborates the BET analysis. In a recent study by Lee *et al.*[23], the authors showed that the frequency difference between E$^1_{2g}$ and A$_{1g}$ modes could serve as a convenient and robust diagnostic of the layer thickness of MoS$_2$ samples. From our results in Table 4.2, the frequency difference (i.e., |E$^1_{2g}$ − A$_{1g}$|) decreases as follows: bulk MoS$_2$ (*ca.* 27 cm^{-1}) > f-MoS$_2$/CNS (*ca.* 26 cm^{-1}) ≈ s-MoS$_2$/CNS (*ca.* 26 cm^{-1}). Thus, our result indicates that there is no significant difference in the layer thicknesses of the two MoS$_2$/CNS composites and that the two synthesis methods we adopted in this study further confirmed the change in the physico-chemical properties of the MoS$_2$ complexes.

Fig. 4.7 shows FT-IR spectra of the MoS$_2$, CNS and MoS$_2$/CNS nanocomposites. In MoS$_2$, the peaks at 1583 and 1518 cm^{-1} were consistent with NH$_2$ in-group deformation (arising from the thiourea or L-cysteine used in the synthesis), and the peak at 1466 cm^{-1} is assigned to the N-C-N asymmetric stretching mode. The band at 1231 cm^{-1} is assigned to stretching vibrations of O-H bonds. The C-O-H stretching mode occurred at 1092 cm^{-1}. The C-S stretching vibrations are observed at 729 cm^{-1}. The weak peak around 600 cm^{-1} m is assigned to Mo-S vibration. Similar peaks are observed for MoS$_2$/CNS

nanocomposite with the additional peak at 2892 cm-1 and 2971 cm^{-1} due to C=C symmetric and asymmetric stretching vibrations as explained elsewhere.[24] Indeed, the presence of the functional groups on the CNS could have contributed to the efficient integration of the CNS with the MoS_2 (as observed in the TEM images).
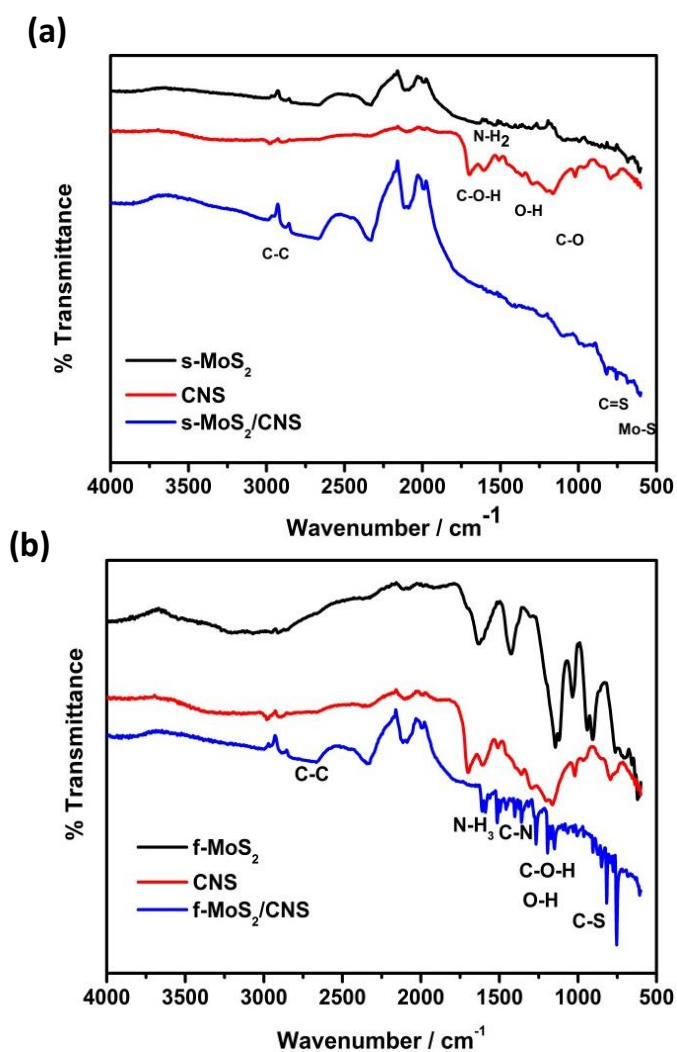
Figure 4.7. FT-IR spectra of spherical (a) and flower-like (b) MoS_2, CNS and MoS_2/CNS nanocomposites

Fig. 4.8 compares the XPS data of s-MoS$_2$/CNS (Fig. 6a and b) and f-MoS$_2$/CNS (Fig. 4.8c and d). XPS analysis reveals the predominant Mo 3d and S 2p characteristic peaks for both s-MoS$_2$/CNS and f-MoS$_2$/CNS. The two materials clearly show that the only elements present are Mo, S, adventitious C and O, and Na 'impurity' (Table 4.3).

Both materials show the typical spectral signature of MoS$_2$, with the co-existence of metallic (1T) and semiconducting (2H) phases.[25-27] There is a clear difference between the two complexes, notably the S 2p splits into two peaks in the s-MoS$_2$/CNS (162.42 and 163.67 eV for S 2p$_{3/2}$ and S 2p$_{1/2}$, respectively), whereas the f-MoS$_2$/CNS splits into four peaks (located at 162.31, 163.34, 164.63 and 169.23, which are assigned to S 2p$_{3/2}$, S 2p$_{1/2}$, S$_2^{2-}$ or S^{2-} and S^{4+}, respectively), suggesting that the S atoms exist in two different chemical states. This finding is indicative of f-MoS$_2$/CNS undergoing partial oxidation into MoS$_x$O$_y$ at the edges and defect sites, which effectively leads to enhanced redox processes. The molybdenum spectra (Fig. 4.8a and c) show the expected Mo 3d$_{5/2}$ and Mo 3d$_{3/2}$, including the Mo^{6+} species (*ca*. 236 eV) usually observed in partially oxidized MoS$_2$ complexes. In addition to the significant changes in the S 2p of the f-MoS$_2$/CNS, its surface atoms, with the exception of O and Na, are lower than observed for the s-MoS$_2$/CNS. Considering that surface Na species are involved in the storage mechanism, one may conclude that Na will be more accessible to the f-MoS$_2$/CNS in an aqueous solution for enhanced energy storage than the s-MoS$_2$/CNS.
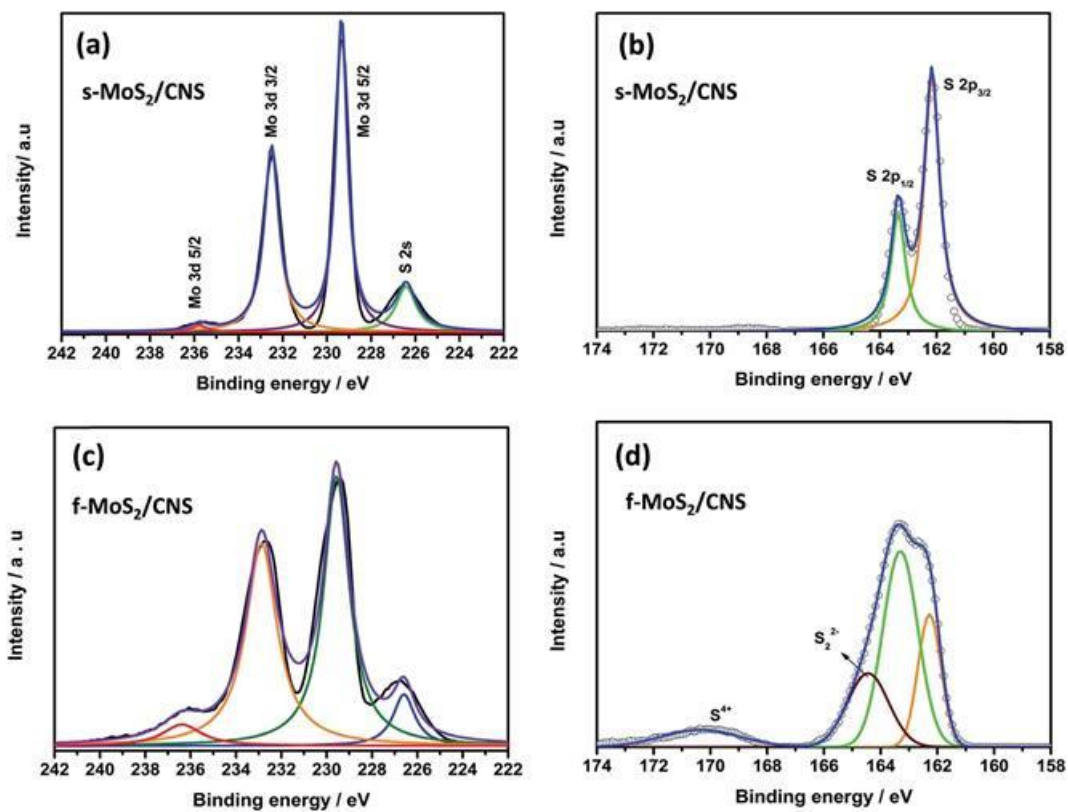
Figure 4.8. High resolution XPS analysis of s-MoS₂/CNS (a and b) and f-MoS₂/CNS (c and b). Mo 3d (a and c) and S 2p (b and d).

Table 4.3 XPS data for the s-MoS$_2$/CNS and f-MoS$_2$/CNS samples

Sample	Binding energy/eV			Atomic /%, det. limit of 0.1 at%				
	Mo 3d$_{5/2}$	Mo 3d$_{3/2}$	Mo 3d$_{5/2}$	Mo 3d	S 2p	C 1s	O 1s	Na
s-MoS$_2$/CNS	229.33	232.7	235.75	25.5	31.6	29.8	12.1	1.0
f-MoS$_2$/CNS	229.00	232.80	236.50	22.8	28.4	15.8	23.1	9.9

4.2.2 Electrochemical properties

Fig. 4.9a shows the cyclic voltammetric (CV) evolutions of the individual CNS, s-MoS$_2$ and f-MoS$_2$ obtained from a 3-electrode configuration in 1 M Na$_2$SO$_4$ at 5 mVs^{-1}. The results shows that s-MoS$_2$ is more capacitive that the f-MoS$_2$ but, as it will be shown later, the capacitance retention of the s-MoS$_2$ is worse than that of the f-MoS$_2$. From Fig. 4.9a, it is evident that CNS does not show any significant current response. Fig. 4.9b compares the CVs of the composite materials, showing that the f-MoS$_2$/CNS gave better performance (high current response and slightly wider voltage window) compared to the s-MoS$_2$/CNS. Fig. 4.8c and d exemplify typical GCPL curves of the various symmetric cells obtained in 1 M Na$_2$SO$_4$ at 0.5 A g^{-1}. The performance of the s-MoS$_2$ is better than its composite, while the f-MoS$_2$/CNS is better than its precursor f-MoS$_2$. As will be shown later, the nanocomposite materials (both spherical and flower-like) showed better capacitance retention and cycling stability than their MoS$_2$ materials. Also, the

CVs and GCPL curves of the composite materials (Fig. 4.9b), notably the flower-like materials, showed quasi-rectangular shapes, a strong deviation from the ideal rectangular shape that is expected from the EDLC. Furthermore, the GCPL of the flower-like composite (Fig. 4.8d) show broad peak around 0.2 V. These results clearly confirm the pseudocapacitive behavior of these MoS_2-based composite materials.
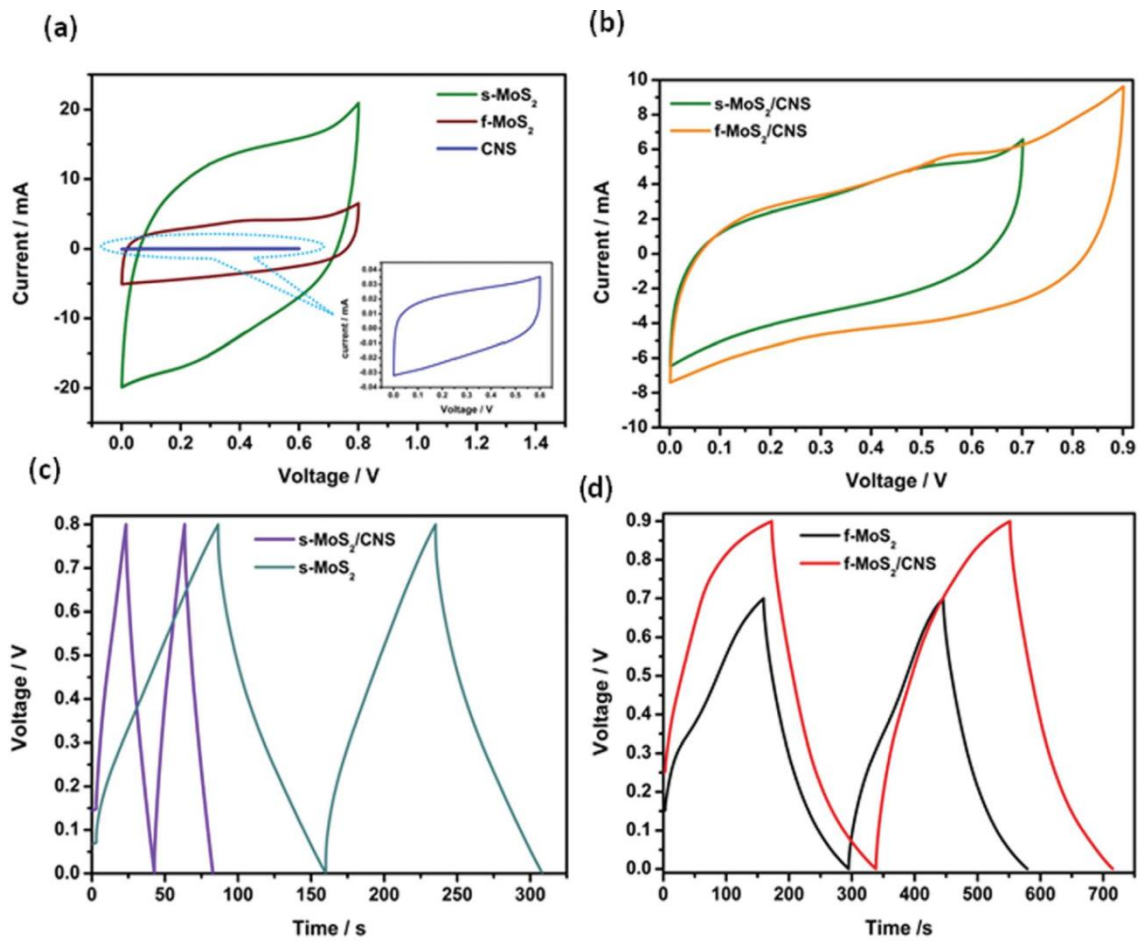
Figure 4.9. CV comparison of (a) s-MoS_2, f-MoS_2, CNS, and (b) s-MoS_2/CNS and f-MoS_2/CNS, and GCPL comparison of (c) s-MoS_2/CNS and s-MoS_2, and (d) f-MoS_2/CNS and f-MoS_2. Conditions: CVs obtained at 5 mVs^{-1} while the GCPL at 0.5 Ag^{-1}; all data in 1 M Na_2SO_4.

Figure 4.10 shows the plots of specific capacitance versus current densities. With the exception of the s-MoS$_2$/CNS-based cell, the capacitance values of all the cells decrease with increasing gravimetric currents. The capacitance of the s-MoS$_2$/CNS-based cell remained essentially the same (*cf.* 108 F g^{-1} at 0.1 A g^{-1} versus 94 Fg^{-1} at 1 A g^{-1}, which is about 13 % capacitance loss). This ability of the s-MoS$_2$/CNS to maintain high capacitance even at high current density is indicative of high-power performance.
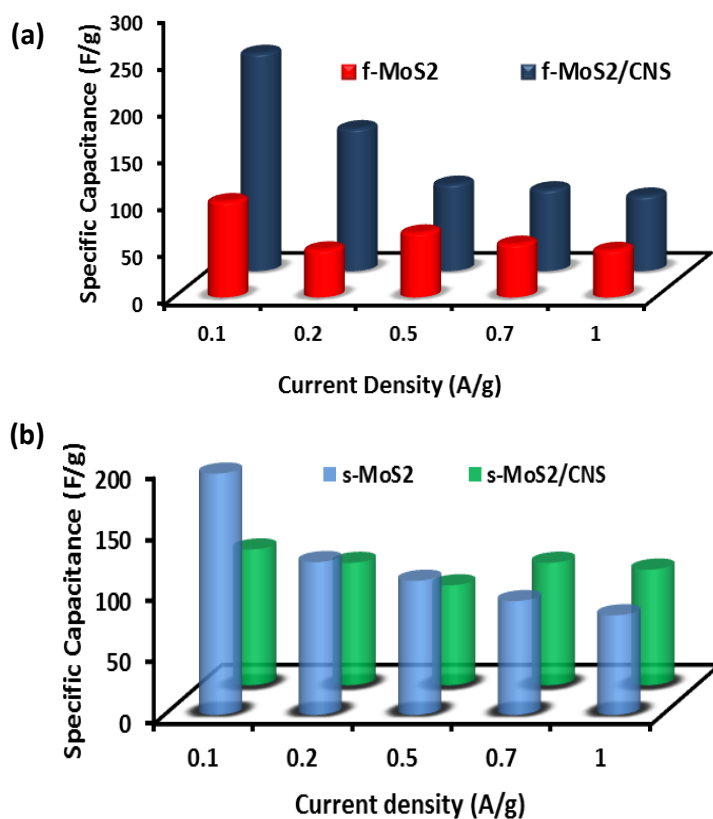
Figure 4.10. GCPL results for specific capacitance at various current densities of spherical and flower-like MoS$_2$ and MoS$_2$/CNS

Table 4.4 compares the values of capacitance, maximum energy and power densities of the symmetric cells, unfortunately there is no related literature with which to compare our results, except 3-electrode systems. The maximum specific capacitance for the flower-like composite f-MoS$_2$/CNS electrodes is 231 F g^{-1} with maximum energy density 26 Wh kg^{-1} and power density 6443 W kg^{-1}. For the sphere-like morphologies, the equivalent values obtained were 108 F g^{-1}, 7.4 Wh kg^{-1} and 3700 W kg^{-1}. The inferior performance of the s-MoS$_2$/CNS electrodes can be explained by the inaccessible surface area for charge storage in MoS$_2$/CNS composite due to the presence of CNS as shown by the Raman spectroscopic data. The maximum energy density achievable with f-MoS$_2$/CNS (26 Wh kg^{-1}) is more than twice that of MoS$_2$ (10 Wh kg^{-1}) alone. The high energy density is owed to the favorable porous nanostructure of the composite in which MoS$_2$ sheets serve as active sites for redox reactions coupled with CNS interaction with electrolyte and synergistic effects of MoS$_2$/CNS composites.

In theory, the specific capacitance of the MoS$_2$ may be estimated from the amount of power needed to carry out the electrolysis of 1 mol of active materials (*i.e.*, 1 F= 96 485 C) and the molar mass of the material (MoS$_2$ = 160.07 g mol^{-1}) using the equation (21):[28]

$$F = \frac{Q}{U} \tag{21}$$

Where U is the voltage window and Q is electrical energy per 1 gram. Because our U ranges between 0.8 and 1 V, the theoretical pseudocapacitance is between 603 and 754 F g^{-1}. If we consider that the supercapacitance of a 3-electrode cell is

about a quarter that of a 2-electrode system, our value for the f-MoS$_2$/CNS based symmetric pseudocapacitor (231 F g^{-1}) is in good agreement with theory.

Table 4.4 Comparison of capacitive performance of various MoS$_2$-based supercapacitors

Aqueous Electrolyte	Electrode material	Device configuration	Voltage (V)	C_{sp} / F g^{-1}	E_{sp}/ Wh kg^{-1}	P_{max}/ W kg^{-1}	Ref.
1 M Na$_2$SO$_4$	f-MoS$_2$/CNS	Symmetric	0.9	231	26	6443	This work
1 M Na$_2$SO$_4$	s-MoS$_2$/CNS	Symmetric	0.7	108	7.4	3700	This work
1 M Na$_2$SO$_4$	s-MoS$_2$	Symmetric	1	195	27	8750	This work
1 M Na$_2$SO$_4$	f-MoS$_2$	Symmetric	0.8	96	8.59	4000	This work
1 M Na$_2$SO$_4$	MoS$_2$	3-electrode	0.7	92.85	7.25	186.5	14
1 M H$_2$SO$_4$	PANI/MoS$_2$	3-electrode	1	575	265	18 000	2
1 M KCl	PPy/MoS$_2$	3-electrode	0.8	553.7	49	400	8
1 M Na$_2$SO$_4$	MoS$_2$-graphene composite	3-electrode	1	243	85	7600	6
1 M Na$_2$SO$_4$	MoS$_2$/RGO	3-electrode	0.6	253	12.65	300	10
1 M Na$_2$SO$_4$	MoS$_2$/MWCNT	3-electrode	1	452.7	-	-	12
3 M KOH	Porous tubular C/ MoS$_2$	3-electrode	0.5	210	-	-	14

Voltage-holding cycling experiments, complemented with EIS experiments, were performed to provide insights into the cycling stability of the four symmetric cells. The zeroth hour cycling capacitance (brown data point in Fig. 4.11 and 4.13) for each of the four symmetric cells was found to be lower than that at the 10th hour cycling, which suggests that MoS_2-based cells require significant amount of time to equilibrate prior to recording data from voltage-holding tests. Thus, the best voltage-holding test data were obtained from the 10th hour. Fig. 4.11 exemplified typical voltage-holding test performed at 0.7 Ag^{-1} for the spherical morphology. At the 10th hour, the s-MoS_2 started with about 140 F g^{-1} and gave 20 F g^{-1} at the end of the 50th hour (Fig. 4.11a), which is about 86 % loss of capacitance. The composite s-MoS_2/CNS started with about 90 F g^{-1} but maintained 55 F g^{-1} at the end of the 50th hour (Fig. 4.11c) which is about 39 % loss of capacity. The fitted EIS data for both the s-MoS_2 (Fig. 4.11b) and its composite form (s-MoS_2/CNS, Fig. 4.11d)) obtained before and after the 50-hour long-cycling experiments are summarized in Table 4.5. For the flower-like materials (Fig. 4.13), the capacitance of the f-MoS_2 at the 10th hour was about 24 F g^{-1} and gave 14 F g^{-1} at the end of the 50th hour (Fig. 4.13a), which is about 42 % loss of capacitance. The composite f-MoS_2/CNS started with about 90 F g^{-1} but maintained 84 F g^{-1} at the end of the 50th hour (Figure 4.13c) which is a mere 6 % loss of capacity. The fitted EIS data for both the f-MoS_2 (Fig. 4.13b) and its

composite form (f-MoS$_2$/CNS, Fig. 4.13d)) obtained before and after the 50-hour long-cycling experiments are summarized in Table 4.5.
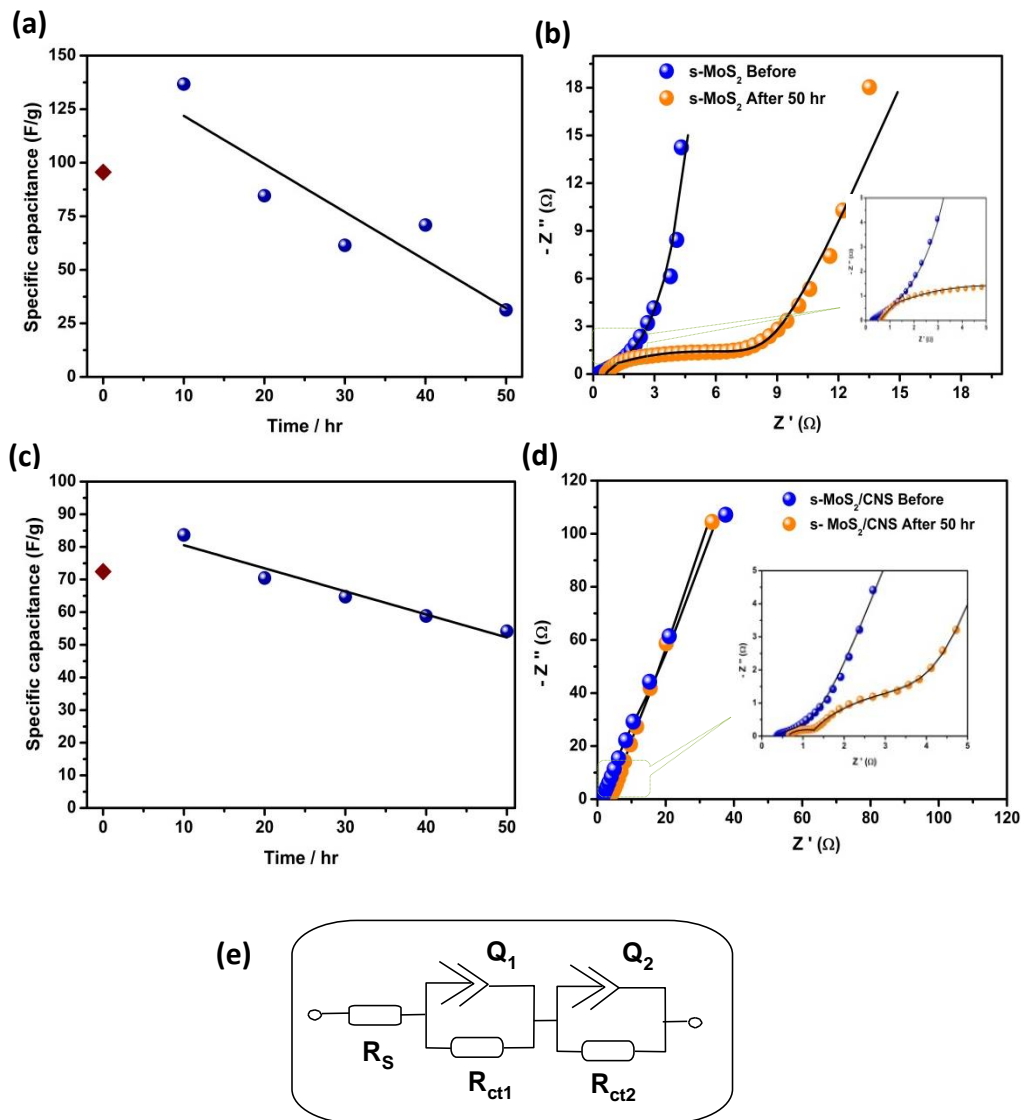
Figure 4.11. Typical GCPL plots at 0.7 A g-1 (a and c) and Nyquist plots (b and d) obtained before and after 50-hour voltage experiments for the spherical (a and b) MoS$_2$- and (c, d) MoS$_2$/CNS-based symmetric pseudocapacitors. The electrical equivalent circuit used in fitting the Nyquist plots is shown as (e).
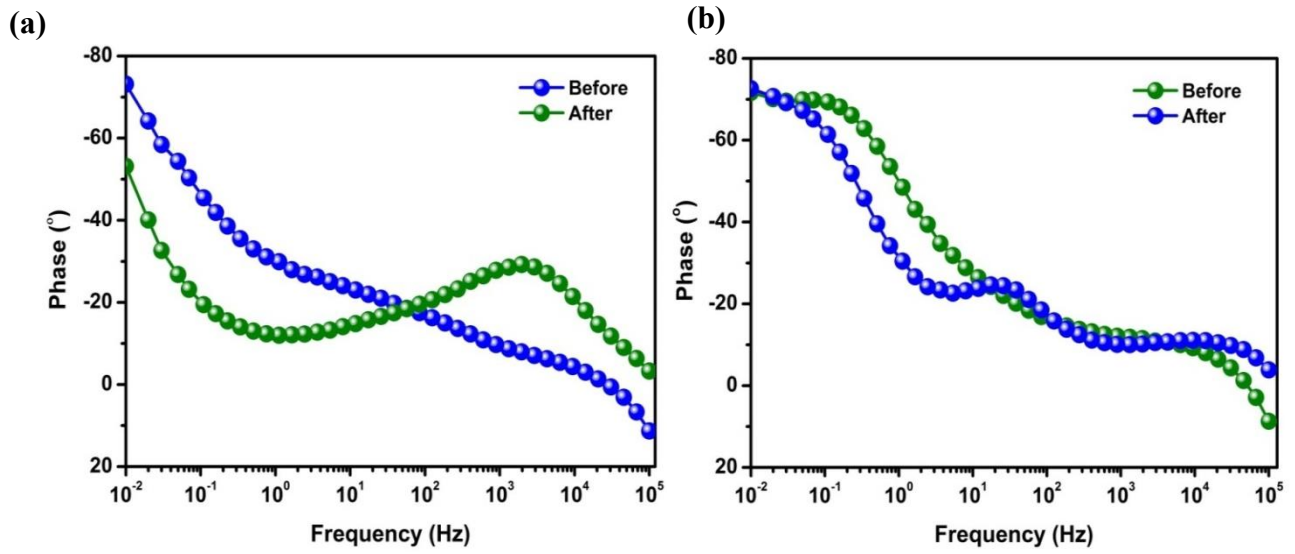
Figure 4.12. Bode diagrams for s-MoS$_2$ (a) and s-MoS$_2$/CNS (b)

Table 4.5 Cycling performance of the layered MoS$_2$ and MoS$_2$/CNS based symmetric pseudocapacitors in 1 M Na$_2$SO$_4$. EIS data before and after 50 h voltage-holding experiments were fitted with the Voigt equivalent circuit

Parameter	s-MoS$_2$ // s-MoS$_2$		s-MoS$_2$/CNS // s-MoS$_2$/CNS	
	0th hour cycle	50th hour cycle	0th hour cycle	50th hour cycle
R_s / Ω	0.23 ± 0.05	0.49 ± 0.06	0.33 ± 0.19	1.14 ± 0.87
Q$_1$ / mF.s(α-1)	0.33 ± 0.08	0.47 ± 0.03	0.2 ± 0.03	2.21 ± 0.11
n$_1$	0.40 ± 0.09	0.77 ± 0.15	0.82 ± 0.17	0.64 ± 0.18
R$_{ct1}$ / Ω	3.75 ± 0.42	10.08 ± 2.7	0.72 ± 0.21	1.39 ± 0.13
Q$_2$ / mF.s(α-1)	8.10 ± 0.34	8.70 ± 0.02	13.32 ± 1.32	9.38 ± 0.02
n$_2$	0.80 ± 0.25	0.80 ± 0.22	0.47 ± 0.29	0.83 ± 0.17
R$_{ct2}$ / Ω	12.51 ± 0.07	7.20 ± 1.95	1.73 ± 0.55	3.23 ± 0.29
Phase angle	-73°	-53°	-80°	-80°
Knee frequency	1 Hz	1 Hz	50 Hz	5 Hz
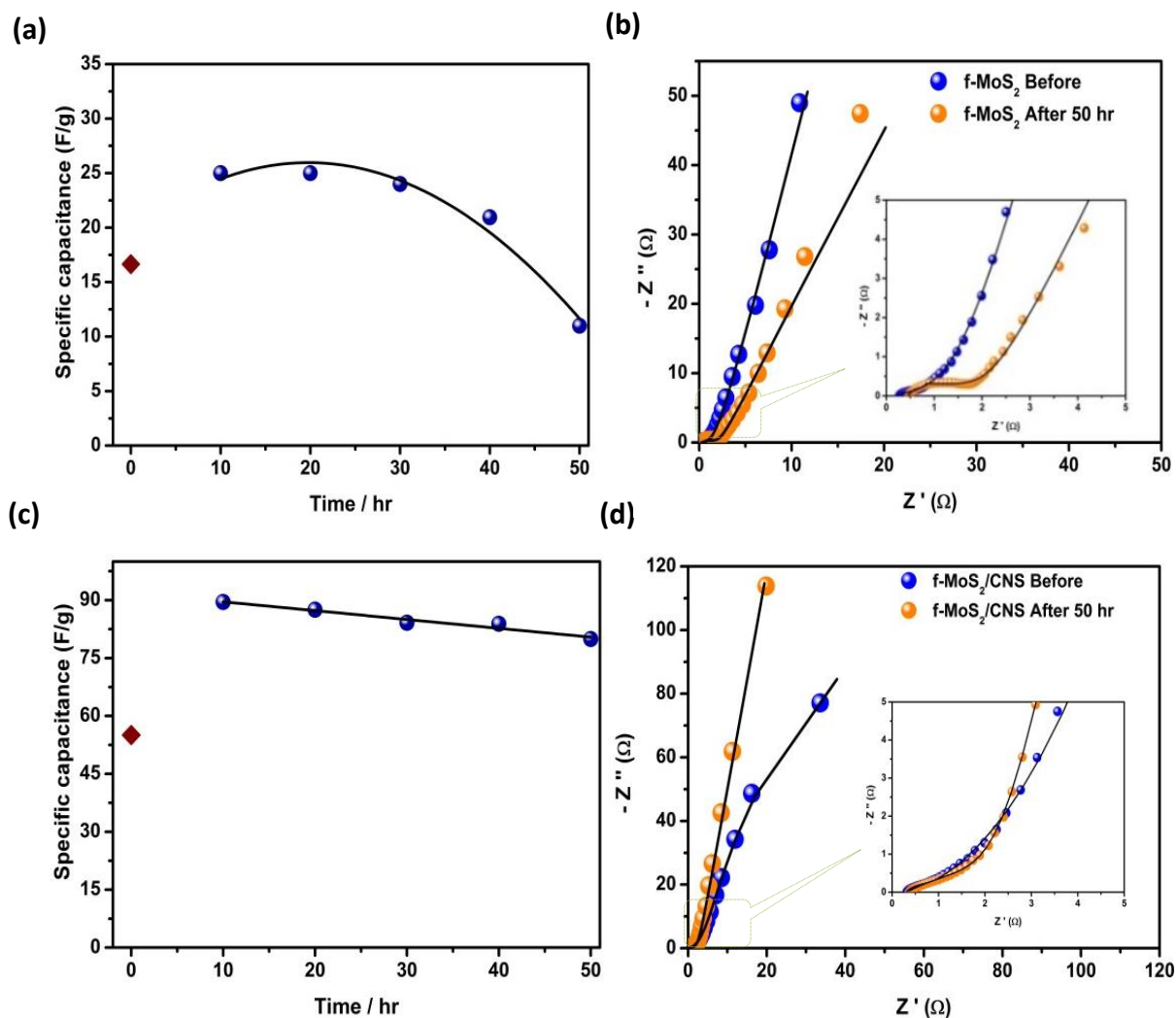
Figure 4.13. Typical GCPL plots at 1 A g-1 for f-MoS2 (a) and 1.5 A g-1 for f-MoS$_2$/CNS (c) and Nyquist plots for f-MoS$_2$ (b) and f-MoS$_2$/CNS (d) obtained before and after 50-hour voltage experiments. The electrical equivalent circuit used in fitting the Nyquist plots is shown in Fig.10e.

(c)

(d)
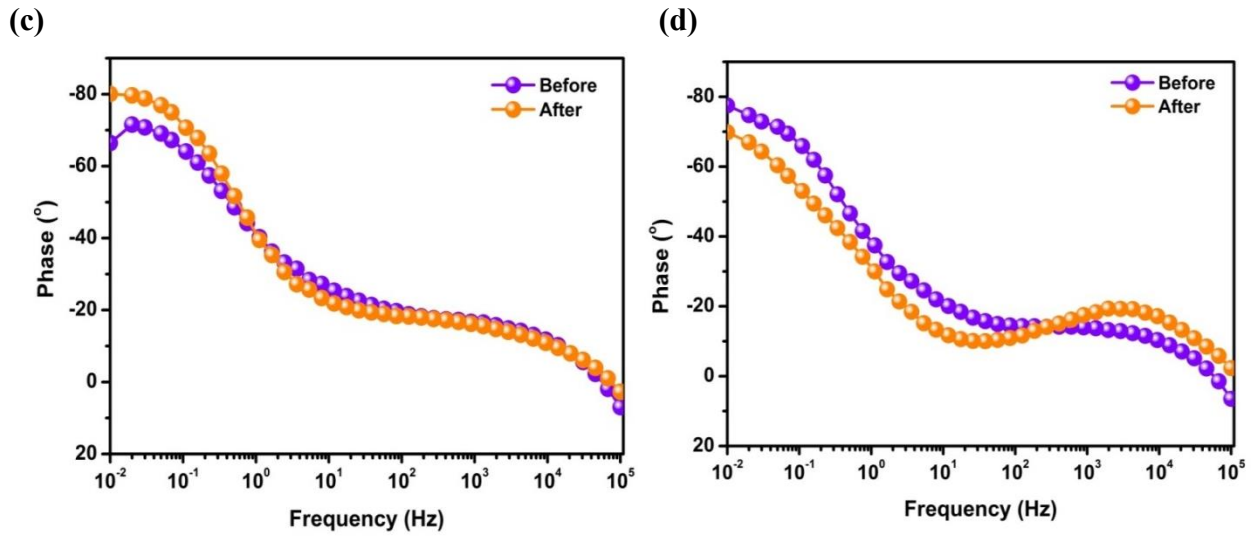
Figure 4.14. Bode diagrams for f-MoS$_2$ (a) and s-MoS$_2$/CNS (b)

Table 4.6 Cycling performance of the flower-like MoS$_2$ and MoS$_2$/CNS based symmetric pseudocapacitors in 1 M Na$_2$SO$_4$. EIS data before and after 50 h voltage-holding experiments were fitted with the Voigt equivalent circuit.

Parameter	f-MoS$_2$ // f-MoS$_2$		f-MoS$_2$/CNS // f-MoS$_2$/CNS	
	0th hour cycle	50th hour cycle	0th hour cycle	50th hour cycle
R_s / Ω	0.21 ± 0.102	0.4 ± 0.1	0.26 ± 0.08	0.31 ± 0.17
Q$_1$ / mF.s(α-1)	0.2 ± 0.14	0.16 ± 0.03	0.12 ± 0.07	0.17 ± 0.02
n$_1$	0.67 ± 0.19	0.73 ± 0.1	0.84 ± 0.14	0.90 ± 0.13
R$_{ct1}$ / Ω	1.70 ± 0.62	1.57 ± 0.16	0.32 ± 0.13	1.28 ± 0.74
Q$_2$ / mF.s(α-1)	21.12 ± 0.07	9.4 ± 0.08	12.24 ± 0.68	9.64 ± 0.36
n$_2$	0.85 ± 0.15	0.62 ± 0.13	0.68 ± 0.21	0.47 ± 0.29
R$_{ct2}$ / Ω	1.73 ± 0.18	2.57 ± 1.24	3.05 ± 0.18	3.81 ± 0.41
Phase angle	-78°	-70°	-75°	-80°
Knee	10 Hz	10 Hz	50 Hz	50 Hz

From the results of the cycling performances of the layered (Figure 4.11) and flower-like (Figure 4.13) materials, the following important findings should be emphasized. First, the zeroth hour cycling capacitance for each of the cells was found to be lower than that at the 10th hour cycling, which suggests that MoS_2-based cells or related layered materials require significant amount of time to equilibrate prior to recording data from voltage-holding tests. Second, the cycling stability for MoS_2 is very poor, but can be greatly improved by integrating it with conductive carbon materials such as the CNS. Third, the cycling stability of the cells from the MoS_2 or its carbon composite is strictly dependent on its morphology, the flower-like morphology showing enhanced electrochemistry compared to its spherical morphology.

Finally, to obtain some insights into the capacitive properties of the cells, we were able to satisfactorily fit the raw EIS data with the electrical equivalent circuit (EEC). The EEC consists of Voigt RC elements (Fig. 4.11e), involving series resistance (R_s), charge-transfer resistance (R_{ct}) and constant-phase elements (CPE or Q). For the cell with the spherical morphology (Table 4.5), the R_s values of the s-MoS_2 before and after 50th hour are 0.23 and 0.49 Ω, respectively. For the s-MoS_2/CNS, the R_s values before and after 50th hour were 0.33 and 1.14 Ω, respectively. The combined R_{ct} values before and after 50th hour were 16.26 and 17.28 Ω, respectively. For the s-MoS_2/CNS it was 2.45 before and 4.62 Ω after the 50th hour cycling. The result clearly proves that the presence of the CNS enhanced the conductivity of the s-MoS_2-based cells. However, in the data for the

cells fabricated from the flower-like morphology (Table 4.6), the R_s values of the f-MoS$_2$ before and after 50th hour are 0.21 and 0.40 Ω, respectively. For the f-MoS$_2$/CNS, the R_s values before and after 50th hour were 0.26 and 0.31Ω, respectively. The combined R_{ct} values for the f-MoS$_2$ before and after 50th hour were 3.43 and 4.14 Ω, respectively. For the f-MoS$_2$/CNS it was 3.37 before and 5.09 Ω after the 50th hour cycling. Like the s-MoS$_2$-based cells, the result for the f-MoS$_2$-based cells suggests that the CNS component serves to reduce the internal resistance of the f-MoS$_2$, thereby improving the conductivity and capacitance of the f-MoS$_2$/CNS-based symmetric pseudocapacitor. The impedance of the CPE (Z_{CPE}) is related to the frequency-independent constant (Q) and radial frequency (w) according to the equation (22):[29]

$$Z_{CPE} = \frac{1}{[Q(jw)^n\,]} \tag{22}$$

where n (with values in the $-1 \leq n \leq 1$ range) is obtained from the slope of log Z versus log f. When $n = 0, 1, -1$ or 0.5, the CPE describes a pure resistor, a pure capacitor, an inductor, or Warburg impedance (Z_w) due to the diffusion of the ions, respectively. For all the cells, the n values observed for these electrodes are generally greater than 0.5, which confirms the pseudocapacitive properties of the MoS$_2$-based symmetric cells, corroborating the CV data in Fig. 4.9a and b.

The data of Bode plots (see, Figure-4.12 and 4.14) summarised in Tables 4.5 and 4.6 sho that the phase angle for each of the systems before and after 50-hour cycling was greater than -75°, but lower than the -90° expected of an ideal EDLC system. The phase angle result is a further confirmation of the pseudocapacitive behaviour of these MoS$_2$-based systems. In addition, knee

frequency (f_o, $\phi = 45°$), is the maximum frequency at which the dominant behaviour of the supercapacitor (power density) can be observed. The knee frequency relates to the rate or power capability of the supercapacitor; the higher the f_o value is, the more rapidly such a supercapacitor can be charged and discharged. The f_o values for the s-MoS$_2$/CNS are 50 Hz (time constant = 0.02 s) before cycling and 5 Hz (time constant = 0.2 s) after the 50th hour voltage-holding testing. However, for the f-MoS$_2$/CNS system, the f_o value remained at 50 Hz before and after the voltage-holding test, which is a further confirmation of the high electrochemical cycling stability of the f-MoS$_2$/CNS system.

The energy-storage mechanism of MoS$_2$ in aqueous supercapaitors is well described in the literature; [26, 28] it is the combined phenomena involving the transition from EDLC to the pseudocapacitive process (faradaic/redox process) and increased active surface area due to possible exfoliation. First, there is the accumulation of ions at the double layer interface between the MoS$_2$ flakes and the electrolyte. This is subsequently accompanied by a redox process: upon charging (reduction) the alkali metal ions in the electrolyte (Na$^+$) adsorb onto the surface and intercalate between the MoS$_2$ layers, followed by deintercalation upon discharging (oxidation), as shown in Equation 22.

$$MoS_2 + Na^+ + e^- \leftrightarrow MoS\text{-}SNa \tag{22}$$

The repeating intercalation-deintercalation process of the sodium ions over several cycles leads to partial exfoliation of the MoS$_2$ layers, resulting in an increased surface area and enhanced specific capacitance. The evidence for the possible partial exfoliation of the MoS$_2$ during repeated intercalation-deintercalation

process of electrolyte ions can be observed from the zeroth hour cycling capacitance (brown data point in Fig. 4.11 and 4.13 described above) which was lower than the 10th hour cycling before stabilizing.

4.3 Conclusions

Two variants of carbon nanosphere-modified molybdenum disulphide (MoS$_2$/CNS) nanostructures were successfully synthesized by a simple one-pot hydrothermal method. The two different synthetic methods gave two different morphologies, flower-like (f-MoS$_2$/CNS) and spherical (s-MoS$_2$/CNS) morphologies. The physical and chemical characterisations reveal that the two materials were properly integrated onto the CNS surface. The addition of CNS impedes the growth of the s-MoS$_2$ crystals in the composite, but enhanced the growth of the f-MoS$_2$, particularly in the (002) plane of hexagonal MoS$_2$. The f-MoS$_2$/CNS showed lattice expansion and large surface area, while the s-MoS$_2$/CNS shows lattice contraction and smaller surface area. The presence of CNS on the MoS$_2$ structure leads to slight softening of the characteristic Raman bands (E$^1_{2g}$ and A$_{1g}$ modes) with larger FWHM. The electrochemical capacitive behaviour of the MoS$_2$-based materials was evaluated in symmetric cells. The electrochemical performance of the composites demonstrates that the MoS$_2$/CNS composite from flower-like MoS$_2$ exhibits better capacitance, energy and power density (231 F/g, 26 Wh/kg and 6443 W/kg) compared to the spherical morphology (108 F g^{-1}, 7.4 Wh kg^{-1} and 3700 W kg^{-1}). CNS plays a vital role in improving electrochemical properties of the MoS$_2$-based electrode materials,

especially with respect to improving the capacitance retention (*i.e.*, stable electrochemical cycling). The excellent electrochemical performances of MoS_2/CNS were accredited to the morphology of the composite and synergistic effects between MoS_2 sheets and CNS. These findings show great promise for future studies of MoS_2 modified with other conducting carbon nanostructures for the development of high-performance electrochemical energy storage systems.

4.4 References

1. Conway, B. E. (Ed.), (1999) Electrochemical Supercapacitors, Scientific Fundamentals and Technological Applications, Kluwer Acadamic/Plenum Publishers, New York,

2. Huang, K. J.; Wang, L.; Liu, Y. J.; Wang, H. B.; Liu Y. M. and Wang, L. L. (2013) Synthesis of polyaniline/2-dimensional graphene analog MoS_2 composites for high-performance supercapacitor. *Electrochimica Acta*, *109*, 587.

3. Wang, G.; Zhang, L. and Zhang, J. (2012) A review of electrode materials for electrochemical supercapacitors. *Chemical Society Reviews*, *41*, 797–828.

4. G.A. Snook, P. Kao and A.S. Best, (2011) Conducting-polymer-based supercapacitor devices and electrodes. *Journal of Power Sources*, *196*, 1-12.

5. Miller, J. R. Maxwell Technologies, Inc. "Energy Storage Technology, Markets and Applications, Ultracapacitors in combination with Lithium-ion" *URL:http://www.maxwell.com/products/ultracapacitors/downloads*.

6. Mazda 'i-ELOOP' Capacitor-Based Brake Energy Regeneration System, *URL:http://www.mazda.com/publicity/release/2011/201111/111125a.html*

7. Huang, K. J.; Wang, L.; Liu, Y. J.; Liu, Y. M.; Wang, H. B.; Gan, T.; Wang, L. L. (2013) Layered MoS_2-Graphene Composites for Supercapacitor Applications with Enhanced Capacitive Performance. *International Journal of Hydrogen Energy*, *38*, 14027–14034.

8. Wang, S.; An, C. and Yuan, J. (2010) Synthetic fabrication of nanoscale MoS_2-based transition metal sulphides. *Materials*, *3*, 401-433.

9. Ma, G.; Peng, H.; Mu, J. ; Huang, H.; Zhou, X.Z. and Lei, Z. (2013) In situ intercalative polymerization of pyrrole in graphene analogue of MoS_2 as advanced electrode material in supercapacitor. *Journal of Power Sources, 229*, 72-78.

10. Mandal, M.; Ghosh, D.; Kalra, S. S.; Das, C. K.; Centre, M. S.; Bengal, W. (2014) High performance supercapacitor electrode material based on flower like MoS2/reduced graphene oxide. *International Journal of Latest Research in Science and Technology*, *3*, 65–69.

11. Changa, K. and Chen W. (2011) In situ synthesis of MoS_2/graphene nanosheet composites with extraordinarily high electrochemical performance for lithium ion batteries, *Chemical Communication*, *47*, 4252–4254.

12. Huang, K. J.; Wang, L.; Zhang, J. Z.; Wang, L. L. and Mo, Y.P. (2014) One-step preparation of layered molybdenum disulfide/multi-walled carbon nanotube composites for enhanced performance supercapacitor *Energy, 67*, 234-240.

13. Soon, J.M. and Loh, K.P. (2007) Electrochemical Double-Layer Capacitance of MoS_2 Nanowall Films. *Electrochemical and Solid-State Letters, 10*, A250-A254.

14. Hu, B.; Qin, X.; Asiri, A.M.; Alamry, K.A.; Al-Youbi, A. O. and Sun, X. (2013) Synthesis of porous tubular C/MoS_2 nanocomposites and their

application as a novel electrode material for supercapacitors with excellent cycling stability. *Electrochimica Acta, 100*, 24.

15. Moorthy, K. K.; Subramani, G.K.V.; Krishnan, S.R. and Kim S. J. (2014) Supercapacitive properties of hydrothermally synthesized sphere like MoS_2 nanostructures. *Materials Research Bulletin, 50*, 499–502.

16. Márquez, A. N.; Romero, R.; Romero, A. and Valverde, J. L. (2011) Carbon nanospheres: synthesis, physicochemical properties and applications. *Journal of Materials Chemistry*, *21*, 1664–1672.

17. Jiang, T.; Pan, W.; Wang, J.; Bie, X.; Du, F.; Wei, Y.; Wang C. and Chen G. (2010) Carbon coated $Li_3V_2(PO_4)_3$ cathode material prepared by a PVA assisted sol – gel method. *Electrochimica Acta*, *55*, 3864–3869.

18. Béguin, F.; Presser, V.; Balducci, A. and Frackowiak, E. (2014) Carbons and electrolytes for advanced supercapacitors. *Advanced Materials*, *26*, 2219-2251.

19. Makgopa, K.; Ejikeme, P. M.; Jafta, C. J.; Raju, K.; Zeiger, M.; Presser, V. and K.I. Ozoemena, (2015) A high-rate aqueous symmetric pseudocapacitor birnessite-type manganese oxide nanohybrids. *Journal of Materials Chemistry. A, 3*, 3480–3490.

20. Wang, C.; Wan, W.; Huang, Y.; Chen, J.; Zhou, H. H. and Zhang, X. X. (2014) Hierarchical MoS_2 nanosheet/active carbon fiber cloth as a binder-free and free-standing anode for lithium-ion batteries. *Nanoscale*, *6*, 5351-5158.

21. Li, H.; Zhang, Q.; Ray Yap, C. C.; Tay, B. K.; Tong Edwin, T.H.; Olivier, A and Baillargeat, D. (2012) From Bulk to Monolayer MoS_2 : Evolution of Raman Scattering. *Advanced Functional Materials, 22*, 1385-1390.

22. Frey, G. L.; Tenne, R.; Matthews, M. J.; Dresselhaus, M. S. and Dresselhaus, G. (1999) Raman and resonance Raman investigation of MoS_2 nanoparticles. *Physical Review B, 60*, 2883-2892.

23. Lee, C.; Yan, H.; Brus, L. E.; Heinz, T. F.; Hone J. and Ryu, S. (2010) Generation of B-doped graphene nanoplatelets using a solution process and their supercapacitor applications *ACS Nano, 4*, 19-26.

24. Mohan A. N. and Manoj, B. (2012) Synthesis and Characterization of Carbon Nanospheres from Hydrocarbon Soot. *International Journal of Electrochemical Science, 7*, 9537 -9549.

25. Acerce, M.; Voiry, D. and Chhowalla, M. (2015) Metallic 1T phase MoS_2 nanosheets as supercapacitor electrode materials. *Nature Technology*, *10*, 313-318.

26. Bissett, M. A.; Kinloch, I. A.; Dryfe, R. A. W. (2015) Characterization of MoS_2-Graphene Composites for High-Performance Coin Cell Supercapacitors. *ACS Applied Materials & Interfaces*, *7(31)*, 17388-17398.

27. Voiry, D.; Goswami, A.; Kappera, R.; Silva, C.C.C.; Kaplan, D.; Fujita, T.; Chen, M.; Asefa, T. and Chhowalla M. (2015) Covalent functionalization of monolayered transition metal dichalcogenides by phase engineering. *Nature Chemistry*, *7*, 45-49.

28. Peng, C.; Hu, D. and Chen, G. Z. (2011) Theoretical specific capacitance based on charge storage mechanisms of conducting polymers: Comment on 'Vertically oriented arrays of polyaniline nanorods and their super electrochemical properties'. *Chemical Communications*, *47*, 4105–4107.

29. Jorcin, J. B.; Orazem, M. E.; Pébère, N. and Tribollet, B. (2006) CPE analysis by local electrochemical impedance spectroscopy *Electrochimica Acta, 51*, 1473 -1479.

CHAPTER FIVE

5 THE EFFECTS OF MORPHOLOGY RE-ARRANGEMENTS ON THE PSEUDOCAPACITIVE PROPERTIES OF MESOPOROUS MOLYBDENUM DISULFIDE (MOS₂) NANOFLAKES[*]

5.1 Introduction

One of the factors that determine the performance of any energy material, be it in catalysis, sensing, photochemistry or electric energy storage, is its morphology.[1] This explains why different materials with different dimensions (zero-, one-, two- or three-dimensional nanostructures) give different physico-chemical properties and applications.[2] Morphology has effects on the surface area, kinetics and thermodynamic properties of the materials.[3] For example, it is has been known that graphene and carbon nanotubes give different catalytic properties due to their morphologies.[4] Nanowires are known to enhance electron transport compared to nanoparticles of the same materials.[5]

Molybdenum disulfide (MoS_2), which belongs to the family of transition-metal dichalcogenides (TMDs), has been receiving some research attention as a viable energy storage material, both as supercapacitor and anode material for lithium-ion batteries.[6, 7] As an important inorganic layered material, MoS_2 has

---

been shown to be an analogue of graphene[8], and useful for hydrogen storage,[9] catalysis,[10] supercapacitors,[11] pseudocapacitors[12] and anode materials for lithium-ion batteries.[13]

One of the active research areas of MoS_2 is in the fabrication of supercapacitors.[14] In the last three years, it is interesting to observe that MoS_2 has begun to attract interest even as full cell (2-electrode) configuration. [12, 15-20] The supercapacitor performance of MoS_2 has been compared to that of the carbon nanotubes (CNT) array electrodes. [6, 21] Spherical morphology of the MoS_2 remains the most investigated morphology for supercapacitor applications. Recently, however, Li et al.[7] showed that hierarchical hollow (rod-like) morphology of MoS_2 (with acetylene black as conducting agent) can potentially serve as a viable anode material for lithium-ion batteries. Also, Qiu et al.[22] showed that MoS_2 with hollow microsphere morphology (using amorphous carbon as conducting agent) is a promising anode material for lithium-ion batteries. Due to the poor conductivity of the MoS_2, most studies regarding its use as energy storage electrode material involved the modification with conducting materials such as CNT,[11] polyaniline (PANI),[23] polypyrrole (PPy),[24] and reduced graphene (RGO),[25] acetylene black[7] and amorphous carbon.[22]

In our previous work, [12] we reported how the presence of CNS is intrinsically linked to the pseudocapacitance of MoS_2 with flower-like and spherical morphologies. The previous study suggested that different morphologies give different physico-chemical properties. The present work is aimed at answering the question of: "*to what extent can the physico-chemistry and pseudocapacitance be influenced by changes in the synthesis methods and*

morphologies of MoS₂"? Thus, in this work, we have introduced a facile synthesis method of preparing two different MoS$_2$: i) graphene-like MoS$_2$ nanoflakes, and ii) hierarchical hollow MoS$_2$ morphology, by simply using water and water/acetone mixture in a one-pot hydro/solvothermal process. We explored the impact of the different morphologies on the pseudoca-pacitive properties of the MoS$_2$ using a symmetric cell (2-electrode configuration) with carbon nanospheres (CNS) as a conducting agent. From our findings, we prove that the pseudocapacitive storage properties of the MoS$_2$/CNS (especially, in terms of cycling stability and electronic conductivity) are strongly dependent on the morphology of the MoS$_2$, the graphene-like nanoflakes showing better physico-chemical properties than the hierarchical morphology.

5.2 Results and discussion

5.2.1 Material Characterisation

MoS$_2$ was synthesized by direct reaction of molybdenum trioxide and potassium thiocyanate in a one-step hydrothermal process. Fig. 5.1 outlines the morphology of MoS$_2$ in the as-synthesized condition. SEM and TEM micrographs reveal 2-dimensional graphene-like nanoflakes. Fig. 5.2 shows the EDX mapping, clearly providing the images of the elemental distribution of the MoS$_2$. Microscopic investigations were conducted to study the morphological transformation of MoS$_2$ from graphene-like to hollow tubes. Fig. 5.3 shows the morphologies of hollow MoS$_2$ obtained from TEM and SEM. Evidently, the hollow structures have a diameter range between 100 and 250 nm and a length of up to 1 μm. These rods

are composed of nanosheets with estimated thickness of 4 nm. Few rods with open ends were seen in Fig. 5.3a. The different contrast (shown by the TEM images) between the centre of the rods and the edges suggests a porous internal. While the pores might enhance ion diffusion, the closed ends hinder the movement of charge carries and the thick long walls greatly increases the diffusion path. Since supercapacitors rely on ionic transportation to form double layer charge storage, as will be discussed later, the specific capacitance is dramatically reduced.

The elemental composition of the as-synthesized g-MoS_2, obtained from the EDX (Fig. 5.2 and summarised in Table 5.1) show S (35), K (6.61) and Mo (58.37) weight %. Also, for the h-MoS_2 (Fig. 5.4) the values were S (39.29), K (14.55) and Mo (46.16) weight %. Intuitively, the results suggest that the stoichiometry is $MoS_{1.75}$ for the g-MoS_2 and $MoS_{2.25}$ for the h-MoS_2 which, within the limits of errors, satisfactorily confirm the stiochiometry of the MoS_2. The impurity 'K' is attributed to the starting precursor KSCN.
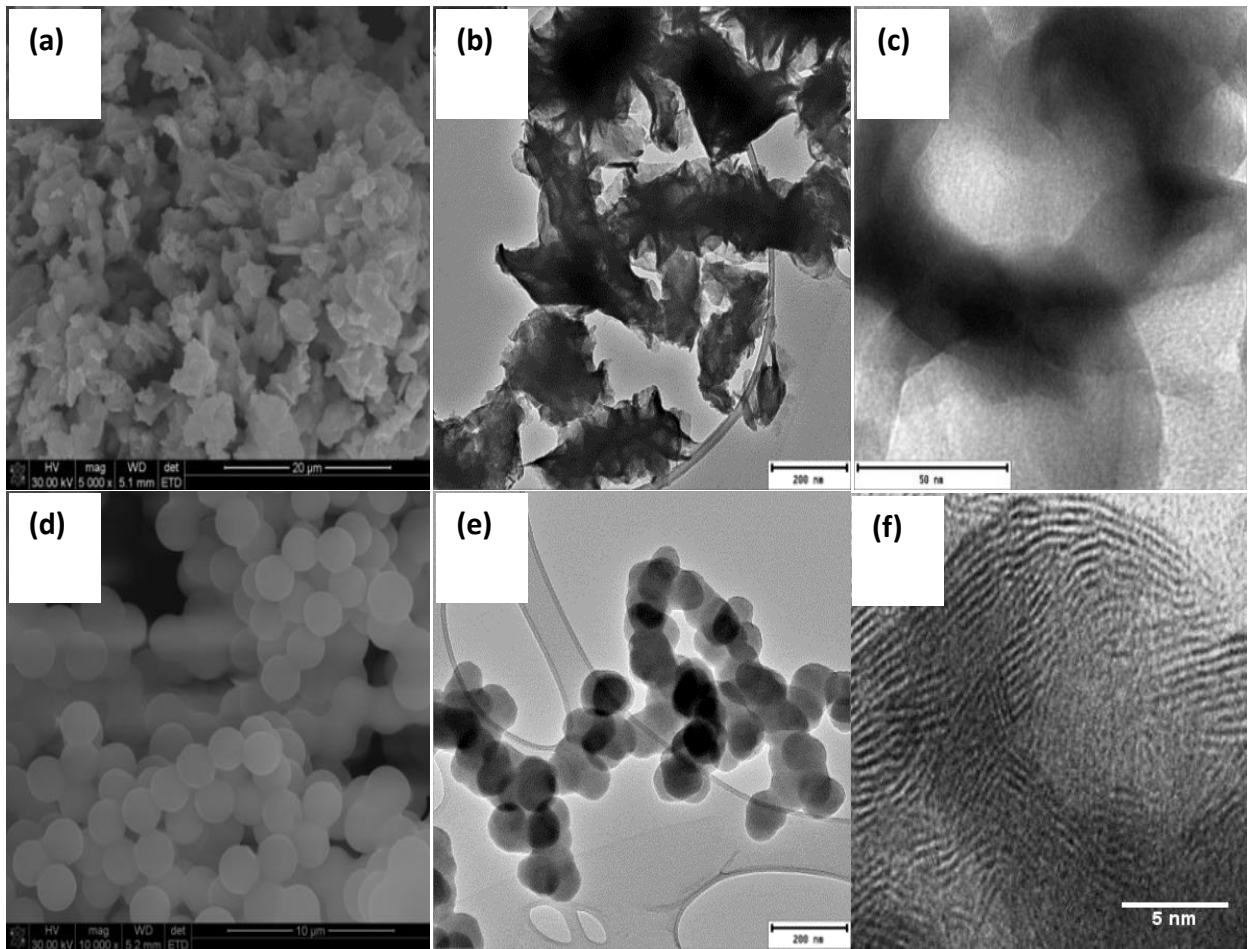
Figure 5.1. SEM (a and d) and TEM (b, c, e and f) images of g-MoS$_2$ (a, b and c), CNS (d and e), and d-spacing of g-MoS$_2$ (f)
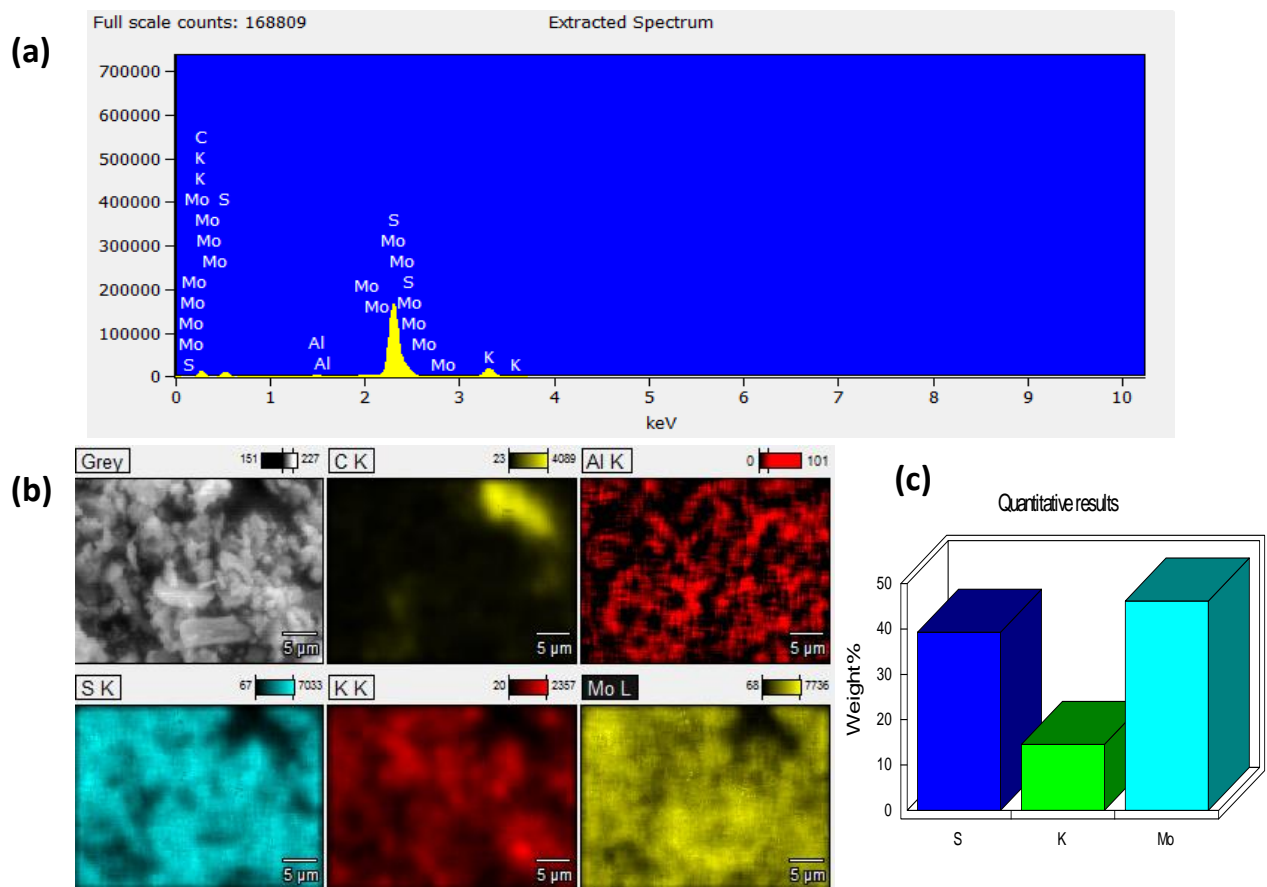
Figure 5.2. (a) EDX spectra and elemental composition of g-MoS$_2$, (b) EDX mapping of the Mo, S and K in g-MoS$_2$, and (c) bar chart representation of the elemental composition of the g-MoS$_2$
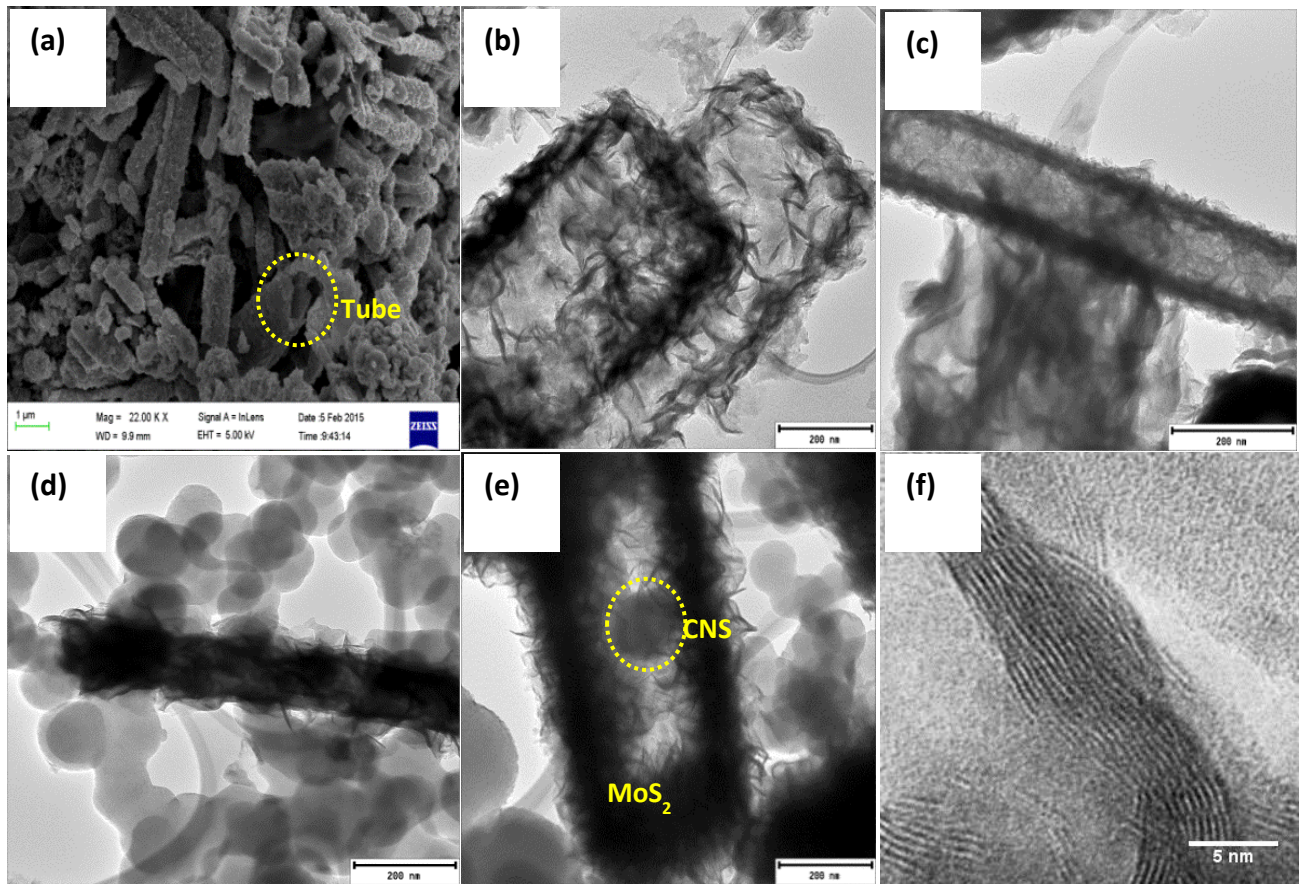
Figure 5.3. SEM (a and d) and TEM images (b, c, e and f) of h-MoS$_2$ (a, b and c), h-MoS$_2$/CNS (d and e) and d- spacing of h-MoS$_2$ (f)
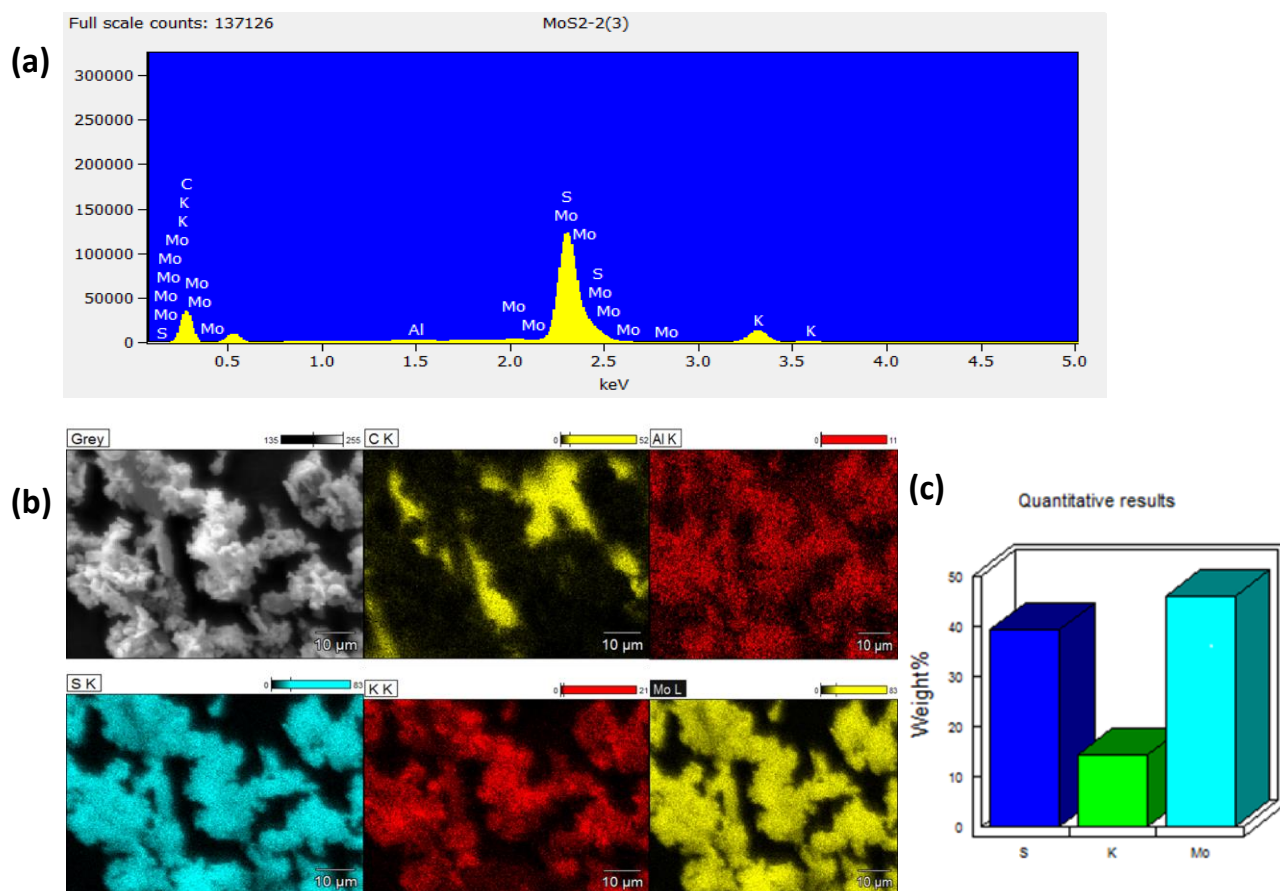
Figure 5.4. (a) EDS spectra and elemental composition of h-MoS$_2$, (b) EDX mapping of the Mo, S and K in h-MoS$_2$, and (c) bar chart representation of the elemental composition of the h-MoS$_2$.

Table 5.1 Concentration of Mo, S and K, calculated from EDX

Sample	S (K)		K (K)		Mo (L)	
	Weight %	Atomic %	Weight %	Atomic %	Weight %	Atomic %
g-MoS$_2$	35.02	58.42	6.61	9.04	58.37	32.54
h-MoS$_2$	39.29	58.95	14.55	17.9	46.16	23.15

Fig. 5.5 compares the spectroscopic data (XRD patterns, Raman and FTIR) of the two as-synthesized MoS_2 materials. The XRD peaks (Fig. 5.5 a-c) observed at about 16.7°, 39° and 69° for g-MoS_2, and 16.7°, 38° and 68° for the h-MoS_2 are attributed to (002) (103) and (201) planes. Both MoS_2 materials exhibit similar XRD patterns in terms of peak positions and in good agreement with the hexagonal structure. The spectral data provide critical information. For example, it is observed that the transformation of the g-MoS_2 to h-MoS_2 leads to decreased (002) peak intensity, an indication that the transition to h-MoS_2 leads to a dramatic suppression of the growth of the MoS_2 layers. Secondly, as depicted in Fig. 5.5b, there is a slight shift (~ 4°) to the higher 2θ value, which is an indication of a lattice contraction for the g-MoS_2. Thirdly, the peaks of the g-MoS_2 are generally broader than those of the h-MoS_2, the full-widths at half maximum (FWHM) for the g-MoS_2 being larger than those of the h-MoS_2, which is indicative of the average particle size of the g-MoS_2 being smaller than that of the h-MoS_2. The average particle was estimated by Scherrer formula and found to be 11.05 and 14.63 nm for g-MoS_2 and h-MoS_2, respectively. This finding means that the surface area of the g-MoS_2 will be larger than that of the h-MoS_2.

Raman spectra of the two MoS_2 materials (Fig. 5.5d) show the characteristic E_{2g} and A_{1g} bands, respectively located at 377 and 402 cm^{-1} for the g-MoS_2 and at 379 and 405 cm^{-1} for the h-MoS_2. The E^1_{2g} mode is related to the in-layer displacement of the Mo and S atoms, while the A_{1g} mode is associated with the out-of-layer symmetric displacements of the S atoms along the c axis.[26] According to Lee *et al.*,[27] the frequency difference between E^1_{2g} and A_{1g} modes

could serve as a convenient and robust diagnostic of the layer thickness of MoS_2 samples. From the Raman data, there is a slight difference for the $|E^1_{2g} - A_{1g}|$ value (cf. 25 cm^{-1} for the g-MoS_2 and 26 cm^{-1} for the h-MoS_2), which suggests that the h-MoS2 has a higher number of layered MoS_2 sheets than the g-MoS2. However, the FWHM is clearly larger for the g-MoS_2 than that of the h-MoS_2. The broadening of the Raman bands is associated with phonon confinement, and indicative of the fact that the lateral dimensions of the g-MoS_2 layers are more in the nano-dimension than that of the h-MoS_2. Simply stated, the average particle size of the g-MoS_2 is smaller (hence larger surface area) than that of its h-MoS_2 counterpart, in excellent agreement with the XRD data. Also, it may be concluded here that use of acetone/water mixture in the synthesis process promotes the formation of more MoS_2 layers compared to the use of water alone that promotes the formation of smaller nano-sized MoS_2 materials.

The FTIR data (Fig. 5.5e) are consistent with the expected functional groups, including the NH_2 in-group deformation at 1583 and 1518 cm^{-1}, N-C-N asymmetric stretching at 1466 cm^{-1}, stretching vibrations of O-H bonds at 1231 cm^{-1}, the C-O-H stretching mode at 1092 cm^{-1}, the C-S stretching vibrations of L-cysteine at 729 cm^{-1}, the weak Mo-S vibration peak around 600 cm^{-1}, and the C=C symmetric and asymmetric stretching vibrations at 2892 cm^{-1} and 2971 cm^{-1}.
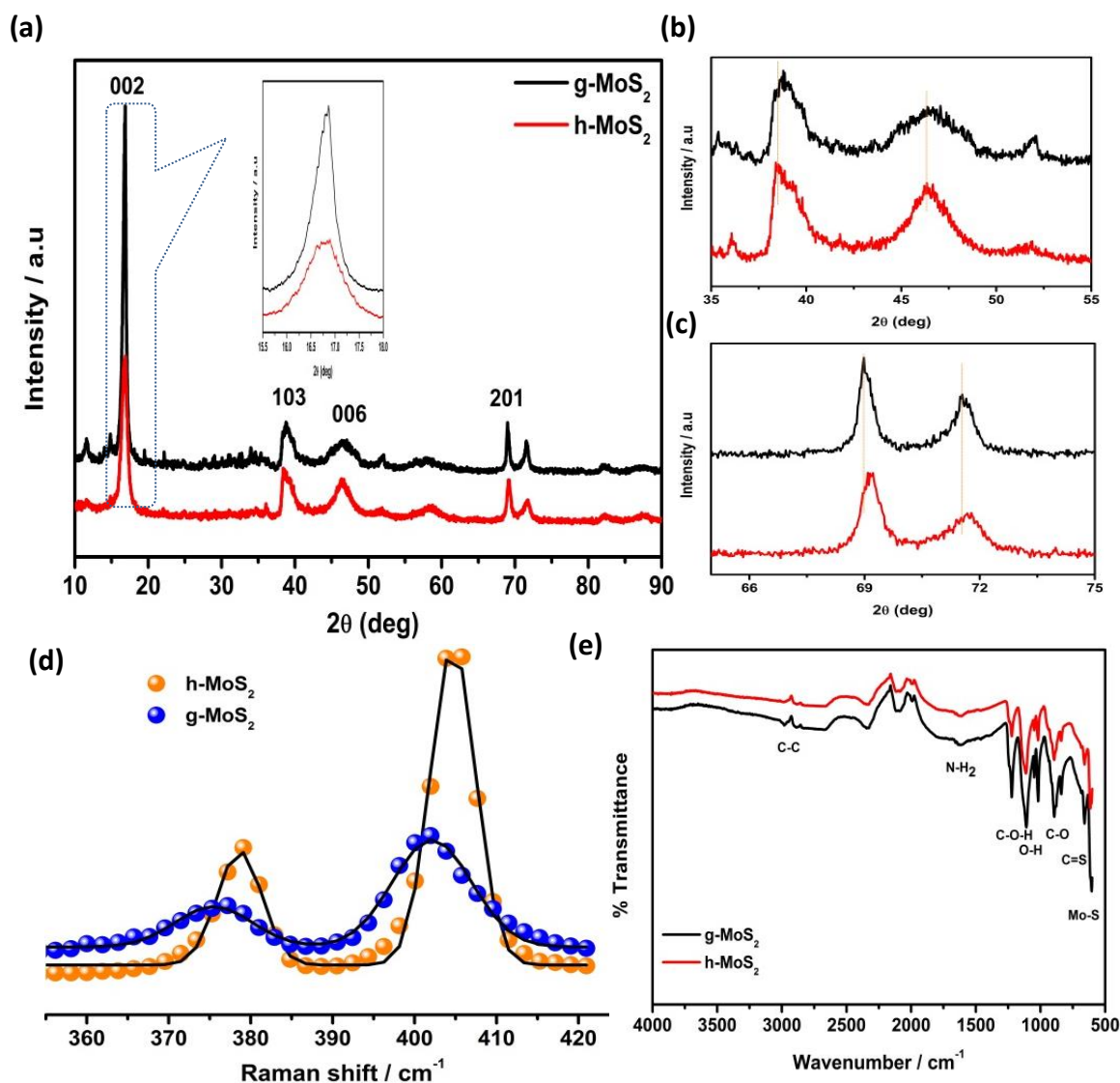
Figure 5.5. XRD pattern of g- and h- MoS$_2$ (a) and their magnified view (b and c) Raman spectra of g-and h-MoS$_2$ (d) FTIR spectra of g-and h-MoS$_2$ (e)

Surface area values from the BET measurements (five-point analysis) summarized in Table 5.2 shows that the g-MoS$_2$ has a higher specific surface area (15.3 m^2 g^{-1}) than its h-MoS$_2$ counterpart (9.94 m^2 g^{-1}). This result is in excellent agreement with the findings from the XRD and Raman analyses. The dramatic reduction of the surface area of the h-MoS$_2$ due to the employment of water/acetone mixture in the synthesis protocol can be explained by the

transformation of the morphology. The BET shows that g-MoS$_2$ and h-MoS$_2$ are mesoporous materials, with the pore size of the former being larger ($\sim$ 43 nm) than the latter ($\sim$ 27 nm).

Table 5.2 BET results showing porous texture of the as-synthesized materials

Sample	SA$_{BET}$	Pore Volume	Pore Size
	m^2/g	cm^3/g	nm
g-MoS$_2$	15.3	0.09	42.91
h-MoS$_2$	9.94	0.07	27.18

5.2.2   Electrochemical Properties

Fig. 5.6 compares typical cyclic voltammograms (CV) and charge-discharge (GCPL) evolutions of the individual CNS, g-MoS$_2$ and h-MoS$_2$ obtained from 3-electrode configuration in 1 M Na$_2$SO$_4$ at 5 mVs^{-1}. The specific capacitance of 32, 16.4 and 3.4 Fg^{-1} obtained for g-MoS$_2$, h-MoS$_2$ and CNS at a current density of 0.1 Ag^{-1}. Evidently, g-MoS$_2$ exhibits higher capacitance compared to the h-MoS$_2$ and CNS. The h-MoS$_2$, however, showed high potential window. The observed capacitance at higher current density is much better when compared to literatures. [15-25] For example, Bissett et al.[15] reported a value of 3.40 Fg-1 for MoS$_2$ in 1 M Na$_2$SO$_4$, while Winchester et al.[18] reported $\sim$3.1 mF cm^{-2} in 6 M KOH. Fig. 5.7 shows that the electrochemical data of the symmetric cells (full cells) obtained

from the CNS-based composite materials, the g-MoS$_2$/CNS and h-MoS$_2$/CNS. There are three key findings here that should be emphasized. First, the g-MoS$_2$/CNS can be cycled at high current densities (0.1 – 2 Ag^{-1}) while the h-MoS$_2$/CNS can only be cycled at lower current densities (0.07 – 0.5 Ag^{-1}). Second, at the same scan rate, the g-MoS$_2$/CNS gave higher current response compared to the h-MoS$_2$/CNS. Third, the g-MoS$_2$/CNS exhibits much higher capacitance (e.g., ~ 200 Fg^{-1} at 0.1 Ag^{-1}) compared to the h-MoS$_2$/CNS (~ 30 Fg^{-1} at 0.1 Ag^{-1}). Table 5.3 summarizes the values of capacitance (F g^{-1}), maximum energy (Wh kg^{-1}) and power densities (W kg^{-1}) of the symmetric cells. It is unfortunate there is no related literature with which to compare our results, except 3-electrode systems. The maximum values for the g-MoS$_2$/CNS system are 183 F g^{-1}, 9.2 Wh kg^{-1} and 2907 W kg^{-1}. For the h-MoS$_2$/CNS system, the values are 70 F g^{-1}, 7.81 Wh kg^{-1} and 1364 W kg^{-1}. The high performance of the g-MoS$_2$/CNS symmetric cell may be related to the high surface area of the g-MoS$_2$ material.
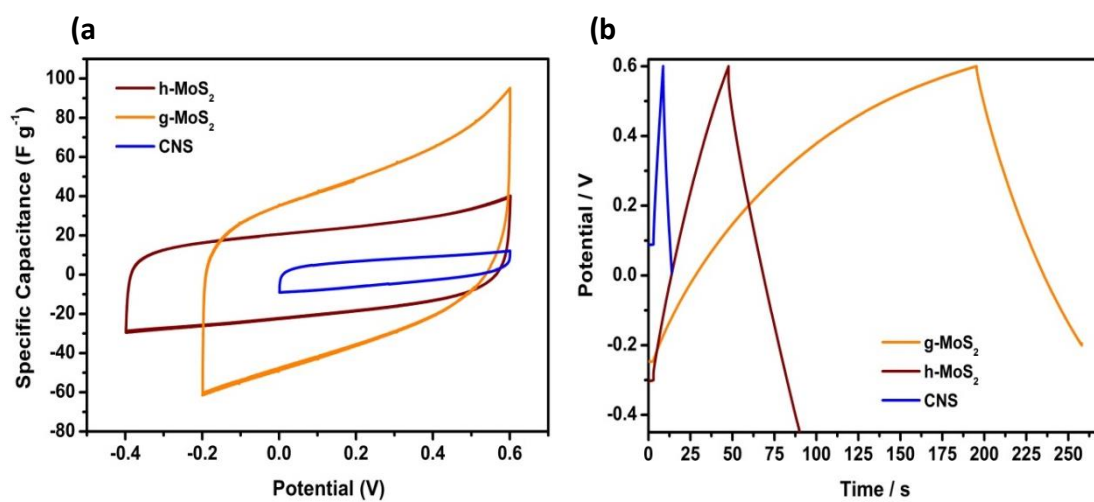
Figure 5.6. Typical CV (5 mV s-1) (a) and charge- discharge (0.1 A g-1) (b) profiles of three-electrode configurations of g-MoS$_2$, h-MoS$_2$ and CNS
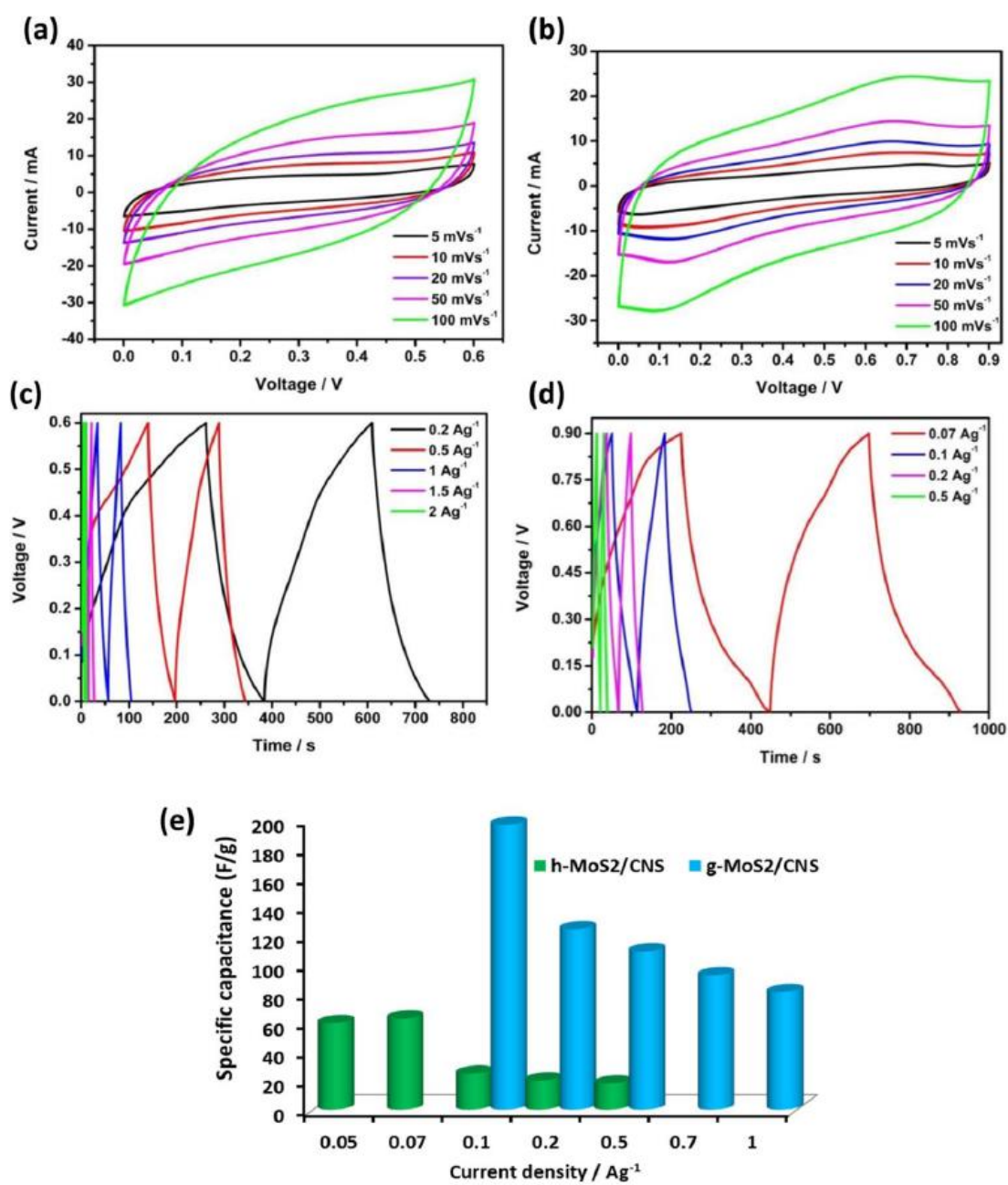
Figure 5.7. Typical CV (a and b) and charge- discharge (c and d) profiles of symmetric cells obtained from g-MoS$_2$/CNS (a and c) and h-MoS$_2$/CNS (b and d) composites, capacitance against different current density (e)

Table 5.3 Comparison of electrochemical capacitive parameters of various MoS_2-based supercapacitors

Aqueous Electrolyte	Electrode material	Device configuration	Voltage window (V)	C_{sp} / F g^{-1}	E_{sp} / Wh kg^{-1}	P_{max} / W kg^{-1}	Ref.
1 M Na$_2$SO$_4$	g-MoS$_2$/CNS	Symmetric	0.6	183	9.17	2907	This work
1 M Na$_2$SO$_4$	h-MoS$_2$/CNS	Symmetric	0.9	70	7.84	1360	This work
1 M Na$_2$SO$_4$	MoS$_2$	3-electrode	0.7	92.85	7.25	186.5	15
1 M Na$_2$SO$_4$	MoS$_2$/r-GO	3-electrode	0.6	253	12.65	300	19
1 M Na$_2$SO$_4$	MoS$_2$/MWCNT	3-electrode	1.0	452.7	-	-	11

The electrochemical cycling stability of the MoS$_2$-based symmetric pseudocapacitor was first tested using the traditional long-term repetitive cycling at 1 Ag^{-1} (Fig. 5.8). From Fig. 5.8, the g-MoS$_2$/CNS-based symmetric pseudocapacitor showed initial capacitance of ~ 35 Fg^{-1} and 28 Fg^{-1} at the end of the 2000th cycle (*i.e.*, about 20% loss of capacitance). On the other hand, the h-MoS$_2$/CNS system started with about 17 Fg^{-1} at the zeroth cycle and 15 Fg^{-1} at the 2000th cycle (*i.e.*, ~ 12% loss in capacitance). The coulombic efficiency of the systems (η / %) was obtained from equation (18).

From Fig. 5.8, the coulombic efficiency for each of the system was about 80% between the zeroth and 50th cycle, but then stabilized at 100% from the 50th to the 2000th cycle. The result indicates that the MoS$_2$-based symmetric

pseudocapacitor require sufficient amount of cycling time to equilibrate prior to a stable power generation.
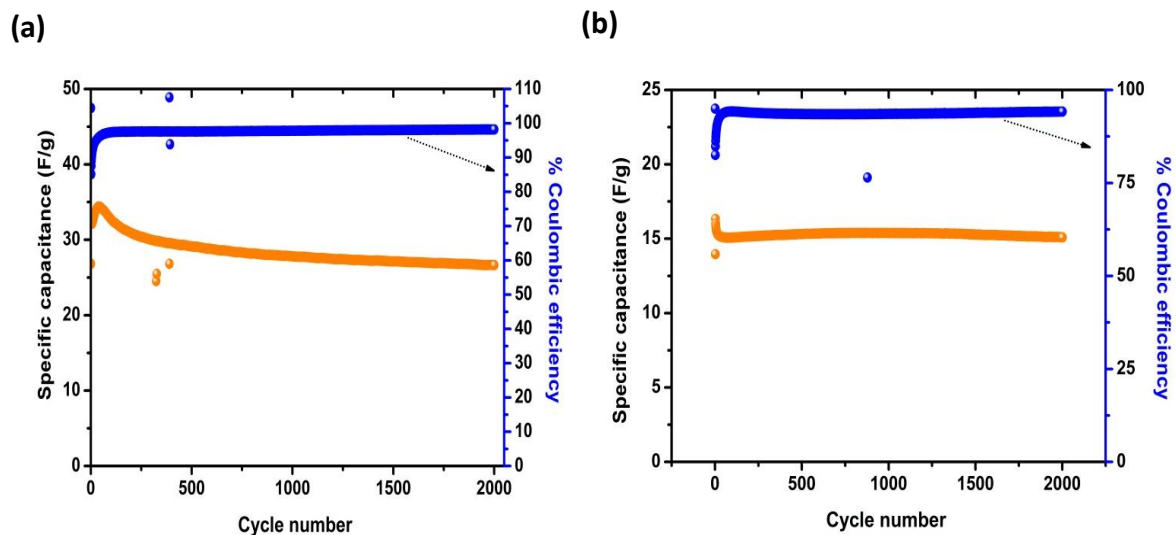
Figure 5.8. Electrochemical cycling test of symmetric pseudocapacitors based on (a) g-MoS$_2$/CNS and (b) h-MoS$_2$/CNS materials. All data were obtained in 1 M Na$_2$SO$_4$ solution at 1 A g^{-1}.

Fig. 5.9 compares the Nyquist and Bode plots of the two systems, satisfactorily fitted with the Voigt RC electrical equivalent circuits (Fig. 5.7e). The circuit comprises the series resistance (R_s), charge-transfer resistance (R_{ct}) and constant-phase elements (CPE or Q). As shown in Table 5.4, the R_s values for the h-MoS$_2$/CNS system before and after 2000th cycle are 0.78 Ω and 0.81 Ω, respectively. For the g-MoS$_2$/CNS, the R_s values before and after 2000th cycle were 0.37 Ω and 0.66 Ω, respectively. The combined R_{ct} values for the h-MoS$_2$/CNS before and after cycling were 2.28 Ω and 5.01 Ω, respectively. For the

g-MoS$_2$/CNS, the equivalent values were 5.65 Ω before and 19.2 Ω after the 2000th cycle. The result shows that the h-MoS$_2$/CNS-based cell is more stable than the g-MoS$_2$/CNS, which corroborates the cycling performance described in Fig. 5.8. Also, the *n* values are generally greater than 0.5, which proves the pseudocapacitive properties of the MoS$_2$-based symmetric cells.

Figure 5.9. Nyquist plots (a and b) and Bode plots (c and d) for g-MoS$_2$/CNS (a and c) and h-MoS$_2$/CNS (b and d) the MoS$_2$/CNS before and after 2000 cycling tests. (e) is the Voigt electrical equivalent circuit used in fitting the Nyquist plots.

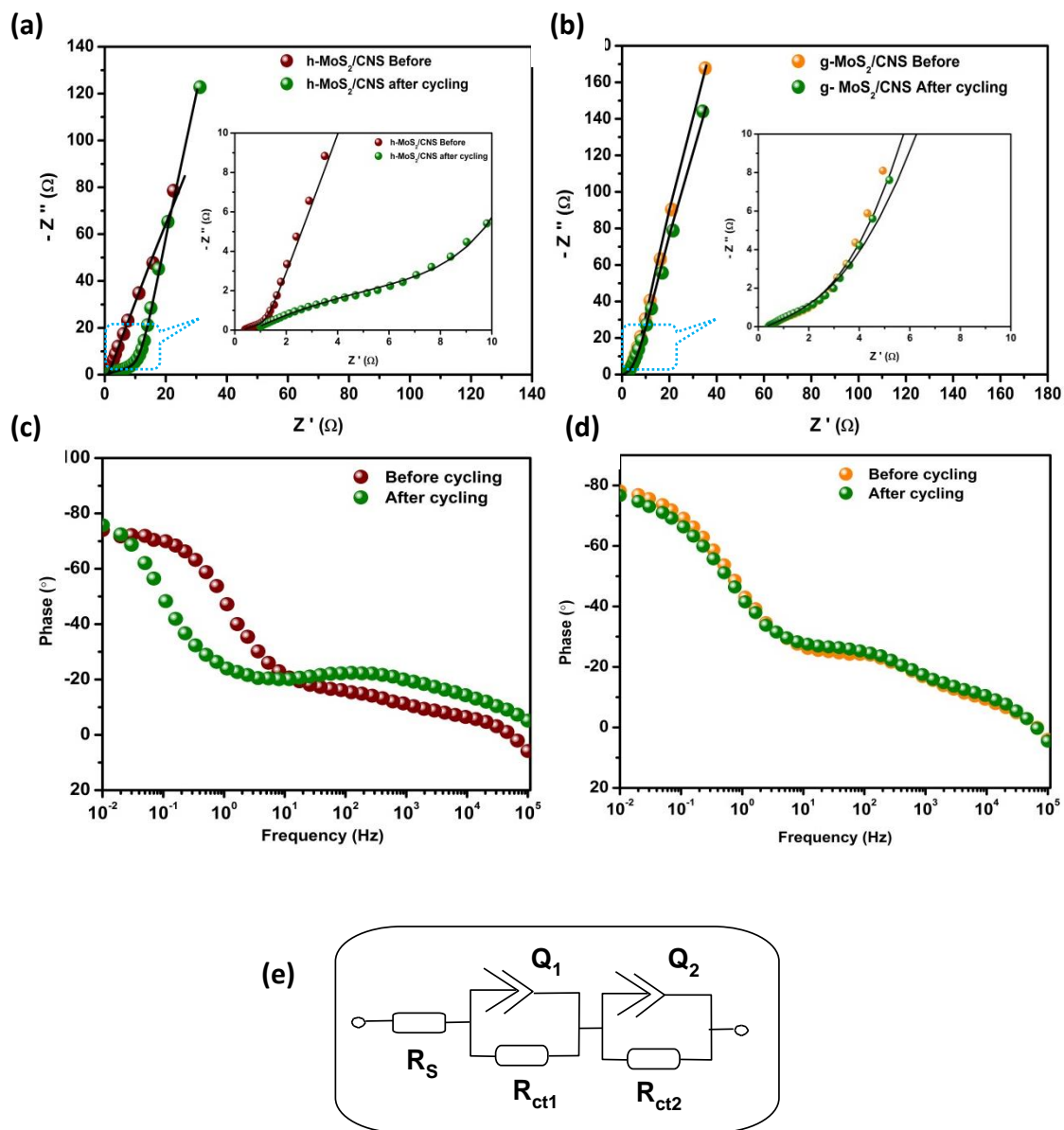From the Bode plots (Fig. 5.9c and d), the phase angles are approximately -80°, which is lower than -90° for an ideal capacitance, confirming the pseudocapacitive behaviour of the systems. The maximum frequency at which the supercapacitor exhibits its dominant properties is known as its knee frequency (f_o, $\phi = 45°$). The knee frequency describes the power capability of the supercapacitor; the higher it is, the faster the supercapacitor can be charged and discharged. From the Bode plots, it is observed that the f_o values for the g-MoS$_2$/CNS are 10 Hz (time constant = 0.1 s) before cycling and 1 Hz (time constant = 1 s) after the 2000th cycle. For the the h-MoS$_2$/CNS, the f_o value remained at 10 Hz even after the 2000th cycle, which confirms the high cycling stability of the the g-MoS$_2$/CNS system.

Table 5.4 Cycling performance of MoS$_2$/CNS based symmetric pseudocapacitors in 1 M Na$_2$SO$_4$. EIS data before and after 2000 cycling experiments were fitted with the Voigt equivalent circuit shown in Fig 5.9e

Parameter	h-MoS$_2$/CNS		g-MoS$_2$/CNS	
	Before cycling	**After cycling**	**Before cycling**	**After cycling**
R_s / Ω	0.78 ± 0.13	0.81 ± 0.32	0.37 ± 0.09	0.66 ± 0.23
Q$_1$ / mF.s(α-1)	0.33 ± 0.17	0.54 ± 0.62	0.08 ± 1.22	0.17 ± 0.06
n$_1$	0.72 ± 0.21	0.63 ± 0.21	0.83 ± 0.27	0.92 ± 0.33
R$_{ct1}$ / Ω	0.64 ± 0.11	2.44 ± 0.38	0.94 ± 0.01	4.63 ± 1.24
Q$_2$ / mF.s(α-1)	0.25 ± 0.07	1.47 ± 0.14	0.12 ± 0.73	0.31 ± 0.07
n$_2$	0.87 ± 0.24	0.82 ± 0.17	0.82 ± 0.29	0.36 ± 0.27
R$_{ct2}$ / Ω	1.64 ± 0.16	2.57 ± 1.24	4.71 ± 0.21	14.57 ± 2.28

| Phase angle | -80° | -80° | -78° | -78° |
| Knee frequency | 10 Hz | 10 Hz | 10 Hz | 1 Hz |

5.3 Conclusions

This work describes the synthesis and electrocapacitive properties of two variants of mesoporous molybdenum disulphide (MoS_2). The main difference in the hydrothermal synthesis of these materials is the use of either water or a water/acetone mixture. The first variant is the graphene-like nanoflakes (g-MoS_2) obtained with water, while the second is the hollow-like morphology (h-MoS_2) obtained with water/acetone. Both materials have been modified with conductive carbon nanospheres and studied as symmetric pseudocapacitors in aqueous electrolyte (1 M Na_2SO_4 solution). The physico-chemical properties of these materials (morphology, surface areas and structural parameters) strongly correlate with their electrochemical capacitive properties. The g-MoS_2 with higher surface area and larger pore size gave higher specific capacitance (183 F g^{-1}), maximum energy density (9.2 Wh kg^{-1}) and power density (2.9 kW kg^{-1}). Sulfur is known for its poor cycling performance, which is the key problem in the realisation of lithium-sulfur battery. Thus, one may speculate that the poor cycling performance of the h-MoS_2 to be due to its slightly higher sulfur content than in the g-MoS_2 (as intuitively provided by the EDX data). But this speculation must be properly investigated in the future to arrive at any foolproof conclusion. However, these findings have opened doors for future research on tuning the morphology of MoS_2 materials for enhanced energy storage.

5.4 References

1. Kumar, N. A.; Dar, M. A.; Gul, R.; Baek, J. (2015) Graphene and Molybdenum Disulfide Hybrids : Synthesis and Applications. *Biochemical Pharmacology*, *18*, 286–298.

2. Yadav, V.K.; Bhardwarj, N. (2013) Introduction to Supercapacitors and Supercapacitor Assisted Engine Starting System. *International Journal of Scientific & Engineering Research*, *4*, 583-588.

3. Huang, Z.; Li, X.; Liu, Z.; He, L.; Tan, X. (2015) Morphology Effect on the Kinetic Parameters and Surface Thermodynamic Properties of Ag_3PO_4 Micro- /Nanocrystals, *Journal of Nanomaterials*, *2015*, 1-9.

4. Fan, Z.; Yan, J.; Zhi, L.; Zhang, Q.; Wei, T.; Feng, J.; Zhang, M.; Qian, W.; Wei, F. A (2010) Three-Dimensional Carbon Nanotube/Graphene Sandwich and Its Application as Electrode in Supercapacitors. *Advanced Materials*, *22*, 3723–3728.

5. Thomas, J. (2015) Supercapacitor electrode materials: nanostructures from 0 to 3 dimensions. *Energy & Environmental Science*, *8*, 702–730.

6. Huang, K. J.; Wang, L.; Liu, Y. J.; Liu, Y. M.; Wang, H. B.; Gan, T.; Wang, L. L. (2013) Layered MoS_2-Graphene Composites for Supercapacitor Applications with Enhanced Capacitive Performance. *International Journal of Hydrogen Energy*, *38*, 14027–14034.

7. Li, G.; Zeng, X.; Zhang, T.; Ma, W.; Li, W.; Wang, M. (2014) Facile Synthesis of Hierarchical Hollow MoS_2 Nanotubes as Anode Materials for High-Performance Lithium-Ion Batteries. *CrystEngComm*, *16*, 10754–

10759.

8.   Ramakrishna Matte, H. S. S.; Gomathi, A.; Manna, A. K.; Late, D. J.; Datta, R.; Pati, S. K.; Rao, C. N. R. (2010) MoS_2 and WS_2 Analogues of Graphene. *Angewandte Chemie - International Edition*, *49*, 4059–4062.

9.   Chen, J.; Kuriyama, N.; Yuan, H. (2001) Electrochemical Hydrogen Storage in MoS_2 Nanotubes, *Journal of the American Chemical Society, 123*, 11813–11814.

10.   Sun, M.; Adjaye, J.; Nelson, A. E. (2004) Theoretical Investigations of the Structures and Properties of Molybdenum-Based Sulfide Catalysts. *Applied Catalysis A, 263*, 131–143.

11.   Huang, K. J.; Wang, L.; Zhang, J. Z.; Wang, L. L.; Mo, Y. P. (2014) One-Step Preparation of Layered Molybdenum Disulfide/multi-Walled Carbon Nanotube Composites for Enhanced Performance Supercapacitor. *Energy*, *67*, 234–240.

12.   Khawula, T. N. Y.; Raju, K.; Franklyn, P. J.; Sigalas, I. and Ozoemena, K. I. (2016) Symmetric pseudocapacitors based on molybdenum disulfide (MoS2)-modified carbon nanospheres: correlating physicochemistry and synergistic interaction on energy storage. *Journal of Materials Chemistry A*, *4*, 6411-6425.

13.   Wang, S.; Li, G.; Du, G.; Jiang, X.; Feng, C.; Guo, Z.; Kim, S. J. (2010) Hydrothermal Synthesis of Molybdenum Disulfide for Lithium Ion Battery Applications. *Chinese Journal of Chemical Engineering*, *18*, 910–913.

14.   Ding, S.; Chen, J. S. (2011) Glucose-Assisted Growth of MoS_2 Nanosheets

on CNT Backbone for Improved Lithium Storage Properties. *Chemistry - A European Journal*, *17*, 13142–13145.

15. Acerce, M.; Voiry, D. and Chhowalla, M. (2015) Metallic 1T phase MoS_2 nanosheets as supercapacitor electrode materials, *Nature Nanotechnology*, *10*, 313-318.

16. Bissett, M. A.; S. D.Worrall, Ian A. Kinloch, and R. A. W. Dryfe (2016). Comparison of Two-Dimensional Transition Metal Dichalcogenides for Electrochemical Supercapacitors. Electrochimica Acta, 201, 30

17. Bissett, M. A.; Kinloch, I. A. and Dryfe, R. A. W.; (2015) Characterization of MoS_2–Graphene Composites for High-Performance Coin Cell Supercapacitors. *ACS Applied Materials & Interfaces*, *7 (31)*, 17388–17398.

18. Clerici, F.; Fontana, M.; Bianco, S.; Serrapede, M.; Perrucci, F.; Ferrero, S.; Tresso, E. and Lamberti, A. (2016) In situ MoS_2 Decoration of Laser-Induced Graphene as Flexible Supercapacitor Electrodes. *ACS Applied Materials & Interfaces, 8*, 10459−10465

19. Winchester, A.; Ghosh, S.; Feng, S.; Elias, A. L.; Mallouk, T.; Terrones, M. and Talapatra, S. (2014) Electrochemical characterization of liquid phase exfoliated two-dimensional layers of Molybdenum disulfide. *ACS Applied Materials & Interfaces*, *6 (3)*, 2125-2130.

20. Cao, L.; Yang, S.; Gao, W.; Liu, Z.; Gong, Y.; Gong, Y.; Ma, L.; Shi, G.; Lei, S.; Zhang, Y. Vajtai, R. and Ajayah, P. M. (2013) Direct laser-patterend micro-supercapacitors from paintable MoS_2 films. *Small*, *9*,

2905-2910.

21.   Soon, J. M. and Loh, K. P. (2007) Electrochemical double-layer capacitance of MoS_2 nanowalls films. *Electrochemical and Solid-State Letters*, *10*, A250-A254.

22.   Qiu, W.; Xia, J.; He, S.; Xu, H.; Zhong, H. and Chen, L. (2013) Facile Synthesis of Hollow MoS_2 Microspheres/Amorphous Carbon Composites and Their Lithium Storage Properties. *Electrochemica Acta*, *117*, 145-152.

23.   Huang, K. J.; Wang, L.; Liu, Y. J.; Wang, H. B.; Liu Y. M. and Wang, L. L. (2013) Synthesis of polyaniline/2-dimensional graphene analog MoS_2 composites for high-performance supercapacitor. *Electrochimica Acta*, *109*, 587.

24.   Ma, G.; Peng, H.; Mu, J. ; Huang, H.; Zhou, X.Z. and Lei, Z. (2013) In situ intercalative polymerization of pyrrole in graphene analogue of MoS_2 as advanced electrode material in supercapacitor. *Journal of Power Sources, 229*, 72-78.

25.   Mandal, M.; Ghosh, D.; Kalra, S. S.; Das, C. K.; Centre, M. S.; Bengal, W. (2014) High performance supercapacitor electrode material based on flower like MoS_2/reduced graphene oxide. *International Journal of Latest Research in Science and Technology*, *3*, 65–69.

26.   Frey, G.L.; Tenne, R.; Matthews, M.J.; Dresselhaus, M.S. and Dresselhaus, G. (1999) Raman and resonance Raman investigation of MoS_2 nanoparticles. *Physical Review B*, *60*, 2883-2892.

27.   Lee, C.; Yan, H.; Brus, L.E.; Heinz, T. F.; Hone J. and Ryu, S. (2010)

Anomalous lattice vibrations of single- and few-layer MoS$_2$. *ACS Nano, 4,* 2695-2700.

CHAPTER SIX

6 CONCLUSIONS AND FUTURE WORK

6.1 Conclusions

A series of MoS_2-based nanopowders (s-MoS_2, s-MoS_2/CNS, f-MoS_2 and f-MoS_2/CNS) were synthesized, characterized and evaluated as supercapacitor electrodes. A comparative study was conducted to analyze the effect of different morphologies from MoS_2-based nanostructures with CNSs on the capacitance and energy density.

- Interestingly, the capacitance of f-MoS_2 is 4 % higher than s-MoS_2 while the energy density differs only by 1.34 Wh Kg^{-1}. The power density of the former is ~ 20 times greater than the latter.

- Incorporation of CNS in-situ into the MoS_2 nanostructures resulted in a dramatic increased capacitance and energy density especially for f-MoS_2/CNS due to its higher surface area (61 m^2 g^{-1}) compared to s-MoS_2/CNS (9.17 m^2 g^{-1}) which improved slightly.

- Both MoS_2/CNS nanocomposites show excellent cycling stability compared to MoS_2 alone. This means that, the conductivity of the electrodes have greatly improved. CNS plays a vital role in improving the electrochemical properties of the electrode. The excellent electrochemical performances of f-MoS_2/CNS were accredited to the morphology of the composite and synergistic effects between MoS_2 sheets and CNS.

In addition, two variants of mesoporous MoS_2 were mixed with CNS through mechanical exfoliation to obtain h-MoS_2/CNS and g-MoS_2/CNS nanocomposites. Both materials were studied as symmetric pseudocapacitors in aqueous electrolyte (1 M Na_2SO_4 aqueous solution).

- The physico-chemical properties of these materials (morphology, surface areas and structural parameters) strongly correlate with their electrochemical capacitive properties. The g-MoS_2/CNS with higher surface area and larger pore size gave higher specific capacitance (183 F g^{-1}), maximum energy density (9.2 Wh kg^{-1}) and power density (2.9 kW kg^{-1}).

- Although g-MoS_2/CNS exhibit good capacitance, inefficient cycling stability is detrimental to the energy density of the composite.

Another main objective was to calculate a proposed circuit model and the pseudocapacitance, by fitting the experimental data to a proposed equivalent circuit.

- For the cell with the spherical morphology, the combined R_{ct} values of the s-MoS_2 before and after 50th hour are in the range 16 to 18 and 2 to 5 for the s-MoS_2/CNS composite. The ccombined R_{ct} values for the f-MoS_2 before and after 50th hour were between 3 and 5 Ω, respectively. On the other hand, for f-MoS_2/CNS it was ~ 3 before and 5 Ω after the 50th hour cycling. Like the s-MoS_2-based cells, the result for the f-MoS_2-based cells suggests that the CNS component serves to reduce

the internal resistance of the f-MoS$_2$, thereby improving the conductivity and capacitance of the f-MoS$_2$/CNS-based symmetric pseudocapacitor.

- The combined R_{ct} values for the h-MoS$_2$/CNS before and after cycling were in the range 2 Ω and 5 Ω, respectively. For the g-MoS$_2$/CNS, the equivalent values were between 5 Ω before and 19 Ω after the 2000th cycle.

- Also, the n values are generally greater than 0.5, which proves the pseudocapacitive properties of the MoS$_2$-based symmetric cells. From the Bode plots, the phase angles are approximately -80°, which is lower than -90° for an ideal capacitance

6.2 Future work

Although a lot of studies have shown hydrothermally prepared MoS$_2$ to be a good electrode material for supercapacitors and batteries, the quality of MoS$_2$ still needs to be improved due to stacking of sheets. More focus should be given to MoS$_2$ prepared by exfoliation methods with resulting pristine, clean, and high-quality structures, which are suitable for energy storage applications.

It is also important to fully understand the electrochemical behavior of the electrodes. In addition to three electrode and symmetric configuration, an asymmetric configuration is recommended in order to increase the working potential and capacitance.

APPENDIX

The presentations and papers during the course of these investigations are:

1. **Tobile N.Y. Khawula**, Kumar Raju, Paul J. Franklyn, Iakovos Sigalas, and Kenneth I. Ozoemena. Studies on molybdenum disulphide for the development of supercapacitors. 5th Annual Gauteng's Nanosciences Young Researcher's Symposium (NYRS), Johannesburg, 9th October, 2015.

2. **Tobile N.Y. Khawula**, Kumar Raju, Paul J. Franklyn, Iakovos Sigalas, and Kenneth I. Ozoemena. Studies on molybdenum disulphide for the development of supercapacitors. 53rd annual conference of the Microscopy Society of Southern Africa (MSSA), (Poster presentation) Pretoria, 29Nov- 4 Dec, 2015.

3. **Tobile N.Y. Khawula**, Kumar Raju, Paul J. Franklyn, Iakovos Sigalas, and Kenneth I. Ozoemena (2016) "Symmetric pseudocapacitors based on molybdenum disulfide (MoS_2)-modified carbon nanospheres: Correlating physico-chemistry and synergistic interaction on energy storage" *Journal of Materials Chemistry A*, 4, 6411–6425.

4. **Tobile N.Y. Khawula**, Kumar Raju, Paul J. Franklyn, Iakovos Sigalas, and Kenneth I. Ozoemena (2016) "The effects of morphology re-arrangements on the pseudocapacitive properties of mesoporous molybdenum disulfide (MoS_2) nanoflakes" *Journal of The Electrochemical Society*, 163 (9), A1-A9.